THESIS FOR THE DEGREE OF DOCTOR OF PHILOSOPHY

Astrochemical Investigations of the Methanol Hotspot in Barnard 5

Tadeus Carl

CHALMERS
UNIVERSITY OF TECHNOLOGY

Department of Physics and Astronomy
Chalmers University of Technology
Gothenburg, Sweden, 2026

Astrochemical Investigations of the Methanol Hotspot in Barnard 5

Tadeus Carl

ISBN 978-91-8103-474-5
DOI: https://doi.org/10.63959/chalmers.dt/5931

Doktorsavhandlingar vid Chalmers tekniska högskola
Ny serie nr 5931
ISSN 0346-718X

Front cover: Perseus molecular cloud by JOLO (September 2021)
URL: https://astrojolo.com
Retrieval date: May 22, 2026

Acknowledgments, dedications, and similar personal statements in this thesis reflect the author's own views.

This thesis has been prepared using LaTeX.

Department of Physics and Astronomy
Chalmers University of Technology
SE-412 96 Gothenburg, Sweden
Phone: +46 (0)31 772 1000
www.chalmers.se

Printed by Chalmers Reproservice
Gothenburg, Sweden, August 2026

"Everything existing in the universe is the fruit of chance and necessity."

- Democritus (460 – 370 BC)

Abstract

The molecules present in the molecular clouds of the Milky Way and other galaxies are formed by a combination of gas phase reactions and grain surface reactions on interstellar dust grains. Especially at low temperatures, grain surface reactions become increasingly important for the formation of many molecules, giving rise to the formation of molecular ices around the grains. The molecules in the ice can be released into the gas phase by different desorption mechanisms, and once in the gas, they become observable via their rotational spectra. The focus of this thesis is on two particular groups of molecules: (1) complex organic molecules (COMs), i.e., carbon-bearing molecules composed of at least six atoms, and (2) sulfur-bearing molecules. Further focus is on observations of such molecules in the gas phase of cold ($\sim 10\,\mathrm{K}$) and dense ($\sim 10^5\,\mathrm{cm}^{-3}$) molecular cloud regions using single-dish radio telescopes. The overall aim of the observations is to put constraints on the formation pathways and the desorption mechanisms of those groups of molecules at low temperatures, as many details of these processes are still not well established.

In particular, the papers appended to this thesis utilized the OSO 20 m, IRAM 30 m, and Yebes 40 m telescopes to investigate the molecular content and chemistry in cold and dense gas at the so-called methanol hotspot in the Barnard 5 (B5) dark cloud (Perseus). The methanol hotspot is the position of maximum methanol emission in B5, and is generally characterized by very efficient ice desorption, releasing water, methanol (CH_3OH), and larger COMs into the gas phase. Paper A presents a deep search for glycine (NH_2CH_2COOH), i.e., the simplest biotic amino acid. Glycine could not be detected, but sensitive upper limits were derived. Paper B studies the distribution of several COMs around the methanol hotspot, showing that COMs are widely distributed in the area and likely released from ices by the same efficient desorption mechanism. Lastly, paper C investigates the sulfur budget and sulfur chemistry at the hotspot. The sulfur budget is significantly higher than towards other dark cloud sources while the chemistry is likely affected by the high gas phase water abundance.

Keywords: ISM – molecules, ISM – molecular clouds, dark clouds, astrochemistry, astrobiology

List of Papers

This thesis is based on the following papers:

[A] **Tadeus Carl**, Eva S. Wirström, Per Bergman, Steven B. Charnley, Yo-Ling Chuang, Yi-Jehng Kuan, "Deep Search for Glycine Conformers in Barnard 5". MNRAS 524, 2023.

[B] **Tadeus Carl**, Eva S. Wirström, Per Bergman, Anna Punanova, Steven B. Charnley, A.O. Henrik Olofsson, "The Distribution of Complex Organic Molecules in Barnard 5". A&A 710, 2026.

[C] **Tadeus Carl**, Eva S. Wirström, Per Bergman, Anna Punanova, Steven B. Charnley, A.O. Henrik Olofsson, Maria J. Jiménez-Donaire, "Sulfur Chemistry in Cold Water-Rich Gas in Barnard 5". To be submitted to A&A.

Acknowledgments

The path to this PhD thesis was quite a journey and I am deeply grateful that I got the chance to take it. I am grateful to Chalmers University, which became a home over the past five years. Working at OSO with its beautiful landscape and historic telescopes, as well as traveling to and working at the IRAM and APEX telescopes, was truly inspiring. But most importantly, I am grateful to all the people who supported me along the way. First and foremost, I am grateful to my supervisors Eva and Per for their amazing support on every step of my PhD work. It was fun, and I would do it again any time! I am also grateful to my friends and colleagues at Chalmers for nice chats and encouraging words, be it at the office, in the car, or over a conference dinner. I would further like to thank Cathy, John, and Henrik for enlightening discussions about various aspects related to the theory and practice of radio astronomical observations. In this regard, special thanks goes to Anna for in-depth discussions and hands-on observing sessions. I am also grateful to Steven for discussions about the theory of molecule formation in the ISM and for hosting me at NASA Goddard (it was an inspiring stay!). I also wish to thank Karine for having me in her teaching team throughout the whole five years as well as Robert for having me in his outreach team (it was fun and I learned a lot!). Thanks also goes to Wouter, Vincent, Matthias, Pia, and Paulina for always ensuring that my PhD education is on track. Additional thanks goes to the people from different institutions of my previous academic education, who provided great support and inspiration: Harry, Ralf, Vera, Lena, Tim, Paola, Jaime, and Anika. Lastly, I would like to thank my loving family and close friends who always supported me. I could not have done it without you.

Acronyms

ALI	Accelerated Lambda Iteration
ALMA	Atacama Large Millimeter/submillimeter Array
AtLAST	Atacama Large Aperture Submillimeter Telescope
CMB	Cosmic Microwave Background
COM	Complex Organic Molecule
HGBS	Herschel Gould Belt Survey
HPBW	Half Power Beam Width
ISM	Interstellar Medium
IRAM	Institut de Radioastronomie Millimétrique
IR	Infrared
JWST	James Webb Space Telescope
LOS	Line Of Sight
LTE	Local Thermodynamic Equilibrium
LVG	Large Velocity Gradient
MoI	Moment of Inertia
OSO	Onsala Space Observatory
PAH	Polycyclic Aromatic Hydrocarbon
RFI	Radio Frequency Interference
RMS	Root Mean Square
RNA	Ribonucleic Acid
RT	Radiative Transfer
SE	Statistical Equilibrium
UV	Ultraviolet
WCCC	Warm Carbon-Chain Chemistry

Thesis Outline

This thesis is structured as follows:

Chapter 1 provides an overview about the field of astrochemistry, discussing some historical aspects (1.1) and theoretical frameworks (1.2), as well as the relation to other fields of study (1.3).

Chapter 2 covers the physical background of the methods utilized in the appended papers to derive molecular abundances from radio-astronomical observations of spectral emission lines. Starting with some basic concepts (2.1), it covers the fundamentals of rotational spectroscopy (2.2), energy level populations (2.3), and radiative transfer (2.4). It furthermore discusses important concepts related to shape of spectral emission lines (2.5) and their detection with single-dish radio telescopes (2.6).

Chapter 3 discusses the modeling of spectral line radiation for both LTE conditions (3.1) and non-LTE conditions (3.2). It furthermore demonstrates how spectral line intensities from molecular cloud sources are calculated based on the principles of radiative transfer (3.3) and how observations with a telescope beam are simulated (3.4).

Chapter 4 covers the basic equations and concepts for the calculation of molecular column densities. Starting with the most basic definitions and a discussion of the case of LTE conditions (4.1), it covers the cases of having optically thin and optically thick conditions (4.2), introduces the population diagram method (4.3), and discusses the case of having non-LTE conditions (4.4).

Eventually, chapter 5 provides a summary of the three appended papers and chapter 6 provides a final summary and an outlook to future work in the field of (observational) astrochemistry, related to the research presented in this thesis.

Contents

CHAPTER 1

Astrochemistry – An Overview

Evolved in the late 1960s, astrochemistry is a highly interdisciplinary field with overlaps to astrophysics, astrobiology, cosmochemistry, planetology, and geology. It considers the evolution of the molecular inventory of the Milky Way and other galaxies by using a combination of astronomical observations, laboratory experiments, and theoretical modeling. This chapter highlights some of the most basic concepts and milestones in the field of astrochemistry. Section 1.1 provides an overview about the history of astrochemistry, reaching back to the first detection of interstellar matter in the Milky Way. Section 1.2 then summarizes key aspects leading to the molecular complexity observed in the interstellar medium of our galaxy and other galaxies. This section is intentionally biased towards the chemistry of the cold and dense gas of galactic molecular clouds, not covering important concepts related to extragalactic chemistry or the chemistry of stellar envelopes, protoplanetary disks, and exoplanetary atmospheres. Lastly, section 1.3 discusses the relation of astrochemistry to other fields of study.

1.1 Evolution from Molecular Astrophysics

Compared to the centuries-old, highly traditional field of observational astronomy, its subfield astrochemistry is a fairly young discipline. It started to evolve in the late 1960s from what was called molecular astrophysics at that time (Hartquist, 1990). Indeed, astrochemistry shares the same roots with astrophysics, going back to the first detection of solar absorption lines (Fraunhofer, 1817) and the development of spectral analysis (Kirchhoff, 1860; Kirchhoff and Bunsen, 1860, 1861). The importance of spectral analysis for astrochemical research can hardly be better summarized than in Kirchhoff and Bunsen (1860):

> "*Bietet einerseits die Spectralanalyse [...] ein Mittel von bewunderungswürdiger Einfachheit dar, die kleinsten Spuren gewisser Elemente in irdischen Körpern zu entdecken, so eröffnet sie andererseits der chemischen Forschung ein bisher völlig verschlossenes Gebiet, das weit über die Grenzen der Erde, ja selbst unseres Sonnensystems, hinausreicht.*"

> "*On the one hand, spectral analysis provides a method of admirable simplicity to detect the smallest traces of certain elements in earthly bodies; on the other hand, it opens up to chemical research a previously entirely inaccessible field that extends far beyond the boundaries of the Earth, indeed even beyond our solar system.*"

Soon after the development of the empirical laws of spectral analysis, astronomers started to classify stars based on the appearance of their spectra. This work culminated in the incorporation of quantum mechanics in the description of stellar spectra and the realization that the "Harvard classification" of stars, which is still in use today, is following a temperature scale (Payne-Gaposchkin, 1925). In addition, it became clear around the same time that most of the nebulous objects observed all over the sky for decades are independent galaxies (Hubble, 1925, 1926), which paved the way for the field of extragalactic astronomy. In the following years and decades, the development of more advanced telescopes sensitive to a broader range of frequencies combined with the refinement of the language of quantum mechanics and new solutions to the equations of general relativity, astronomers found a whole lot

of new exotic stellar objects. The characterization of the physical properties as well as the processes happening within and around these objects started to be in the hand of astrophysicists.

The identification of elements in the photosphere of the Sun and other stars has clearly shown that stars are made of the same elements that are also found on Earth, even though in very different proportions. The same can be said about the space between the stars of our galaxy and other galaxies. It started to become apparent at the beginning of the last century that the interstellar space is not empty but filled with a mixture of gas, dust, and radiation, together referred to as the interstellar medium. The first direct evidence of interstellar matter is reported in Hartmann (1904), who noted an absorption line of ionized calcium in the spectrum of δ Orionis at a velocity that does not fit the velocity of the remaining lines in the spectrum, indicating that this line is not produced in the photosphere of the star but by some calcium-bearing gaseous medium in the line of sight towards the star. The same phenomenon is reported in Heger (1919) for two lines of ionized sodium and an additional line of ionized calcium towards β Scorpii and δ Orionis. Pickering (1912) discusses the properties of the *"interstellar absorbing medium"*, considering that it might be the (at this time still hypothesized) ether producing the absorption of light, even though the observed selective absorption at specific wavelengths is recognized as characteristic for a gas, as also noted by Kapteyn (1909). Systematic studies on the *"detached calcium lines"* and the related hypothesized *"calcium clouds"* are reported in Struve (1925, 1926, 1927, 1928). Thorndike (1930) is stating that the existence of a diffuse cloud filling the galactic interstellar medium is almost certain, highlighting that *"[...] it could scarcely have been believed that the enormous gaps between the stars are completely void"*. He is also referring to the terrestrial aurora produced by charged particles ejected by the Sun, arguing that the same process should be at work for all stars, continuously filling the interstellar space with particles. The first concrete description of the effect of interstellar dust grains on the received light from stars, i.e., the extinction and reddening of the light by the dust, is given by Trumpler (1930). Even though the term "interstellar dust" is not used as such in this work, it quickly became the major candidate to explain the reddening of starlight. Struve (1933) provides a compact summary of the fundamental advances in astronomy made over the previous approximately

30 years, i.e., the discoveries that (i) nebulae are extragalactic objects, and (ii) that the galactic interstellar space is filled with a mixture of gas and dust. He emphasizes that *"[...] some of the recent results [...] concerning the physical properties of matter in interstellar space [...] have opened a new field of research in astrophysics."*

The possibility that the galactic interstellar gas is not only populated by ions or atoms but also by molecules is first seriously discussed in several papers from 1937 (Swings, 1937; Eddington, 1937; Saha, 1937; Swings and Rosenfeld, 1937). For example, Eddington (1937) argues that neutral atoms of H, O, N, etc. can and should exist in interstellar space, and that they should be able to react with one another to form molecules, occurring as mixtures of ices that are dominated by water. Considerations like those are based on observations by Merrill (1934, 1936) and Dunham (1937) of several interstellar absorption lines which could not be assigned to atoms or ions. Examples are lines at λ 6613.9 and λ 4300.3, which are theoretically discussed in Swings (1937) and Swings and Rosenfeld (1937) as being produced by CO_2 and CH, respectively. Eventually, the presence of interstellar CH, CN, and CH^+ is confirmed in McKellar (1940) and Douglas and Herzberg (1941) by comparison of observations and theoretical calculations to laboratory data. van de Hulst (1946) and Oort and van de Hulst (1946) discuss interactions between gas and dust, including accretion, desorption, surface mobility, and surface reactions. van de Hulst (1946) was the first to consider the actual *"chemical composition"* of dust particles, reporting chemical reactions that could lead to the formation of H_2, O_2, and water, noting that *"some of these molecules might be transiently formed without being part of the final [dust] particle."* He suggests that the dust grains should contain, i.a., H_2O, H_2, CH_4, and NH_3 (in decreasing order of abundance), and finds that *"this conclusion is remarkably close to the suggestion of Eddington (1937) that the dark clouds in space would consist mainly of ice-particles."*

Strömgren (1948) introduces the first large-scale separation of the interstellar medium into regions dominated by neutral hydrogen and ionized hydrogen, i.e., H-I and H-II regions, respectively. The process of molecule formation is thereby assumed to take place in low-temperature H-I regions, as can be read in e.g., Spitzer and Tukey (1951). It has been further realized that molec-

ular hydrogen should also exist in those regions where other molecules are formed (Kahn, 1955; Takayanagi and Nishimura, 1960; McCrea and McNally, 1960; McDowell, 1961), even though it has no observable rotational spectrum because of its lacking dipole moment. The first detection of the 21 cm line of atomic hydrogen was only achieved shortly before by Ewen and Purcell (1951). Noting that the formation of H_2 by two-body reactions in the gas phase is highly inefficient, McCrea and McNally (1960) present the first basic framework for the formation of H_2 at the surface of dust grains. Eventually, Gould and Salpeter (1963) and Gould et al. (1963) extend this framework and present first detailed model calculations of the galactic abundance distribution of H_2.

At around the same time, Weinreb et al. (1963) report the first detection of an interstellar polyatomic species, OH, at radio wavelengths, basically marking the beginning of molecular radio spectroscopy. The advent of the first high resolution radio receivers soon led to the detections of further interstellar molecules, composed of two (CO, CS, SO; Wilson et al., 1970; Penzias et al., 1971; Gottlieb and Ball, 1973), three (H_2O, HCN; Cheung et al., 1969; Buhl and Snyder, 1970), four (NH_3, H_2CO; Cheung et al., 1968; Snyder et al., 1969), and even six (CH_3OH, CH_3CN; Ball et al., 1970; Solomon et al., 1971), seven (CH_3C_2H, CH_3CHO; Snyder and Buhl, 1973; Fourikis et al., 1974), and up to nine (CH_3OCH_3, CH_3CH_2OH; Snyder et al., 1974; Zuckerman et al., 1975) atoms. The quickly increasing number of detected interstellar molecules naturally raised the question how all these molecules, including complex species like CH_3CH_2OH, could actually form in the cold vacuum of interstellar space. Inspired by this question and based on ideas and principles discussed in earlier work by, e.g., van de Hulst (1946) and Gould and Salpeter (1963), the first astrochemical models (Herbst and Klemperer, 1973; Allen and Robinson, 1975) and laboratory experiments (Anders et al., 1974; Bar-Nun, 1975) were developed. The basic assumption was (and still is) that interstellar molecules are formed by chemical reactions in the gas phase as well as at the surface of dust grains. Some more general aspects of the process of molecule formation in interstellar space are discussed in the next section. For more details about the early advances in astrochemistry see the reviews by Dalgarno and Black (1976) and Watson (1976).

1.2 Interstellar Molecular Complexity

As discussed in the previous section, astrochemistry evolved from astrophysical research on the properties of the galactic interstellar medium (ISM) by shifting the focus away from treating the chemical components of the ISM as parts of its physical characteristics towards asking what *chemical* processes, i.e., what reactions, are responsible for the molecular complexity we observe in the ISM. The term "molecular complexity" is understood here as both the number of known molecules as well as the complexity of individual species, largely measured by the number and sorts of constructing atoms as well as by the atomic configuration.

The molecular inventory

Dalgarno and Black (1976) report a total number of 41 detected interstellar molecules, excluding isotopologues. Most of the early detections from the late 1960s and early 1970s were made towards high-mass molecular clouds close to the galactic center such as Sgr B2 and Orion. The high amount of material in such clouds makes it easier to detect molecular emission, as the intensity/optical depth of spectral lines is directly proportional to the number of emitting/absorbing molecules along the line of sight. However, progress in the field of radio receiver technology soon made it possible to detect more of the fainter emission from closer low-mass molecular clouds such as TMC-1, as well as from extragalactic sources and protoplanetary disks. Some of the first molecular detections in extragalactic sources (Rickard et al., 1975, 1977) and protoplanetary disks (Beckwith et al., 1986; Ohashi et al., 1991) were made for simple species like CO, CS, and HCN, which have been observed before in molecular clouds of the galactic ISM.

McGuire (2022) provides a review of all detected interstellar molecules up to the year 2021, i.e., 241 in total, excluding isotopologues. Fig. 1.1 shows the cumulative number of detected molecules as a function of time, highlighting the commissioning dates of the most important contributing facilities. The majority of interstellar molecules ($> 80\,\%$) were first detected via their respective emission lines in the radio range (centimeter, millimeter, submillimeter) produced by transitions between rotational energy levels. A smaller number of detections comes from observations in the infrared (IR), optical, and ultra-

violet (UV) ranges. More than 90 % of all ISM molecules were first detected in either a star-forming region (e.g., Sgr B2), a dark cloud (e.g., TMC-1), a carbon star (e.g., IRC+10216), or a diffuse/translucent/dense cloud along the line of sight towards a background source (source types ordered by decreasing number of detections). Of the 241 interstellar molecules known by 2021, approximately 30 % have also been detected in other galaxies. Furthermore, 25 of the known molecules have also been detected in protoplanetary disks, 10 in interstellar ices, and 9 in exoplanetary atmospheres. Since 2021, and until August 2026, the number of detected interstellar molecules has further increased to about 350, which is a strong increase in only about four years. Part of the reason for that might be the use of new machine learning algorithms to propose new targets for interstellar survey studies [McGuire, B.; priv. comm.] (Lee et al., 2021; Scolati et al., 2023).

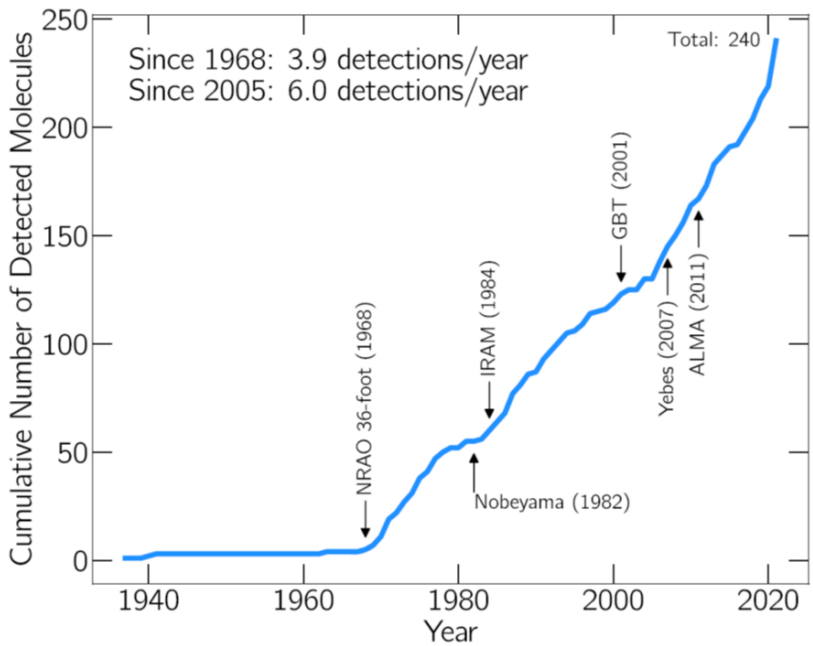

Figure 1.1: Cumulative number of detected ISM molecules as a function of time (as of 2021). Credit: McGuire (2022).

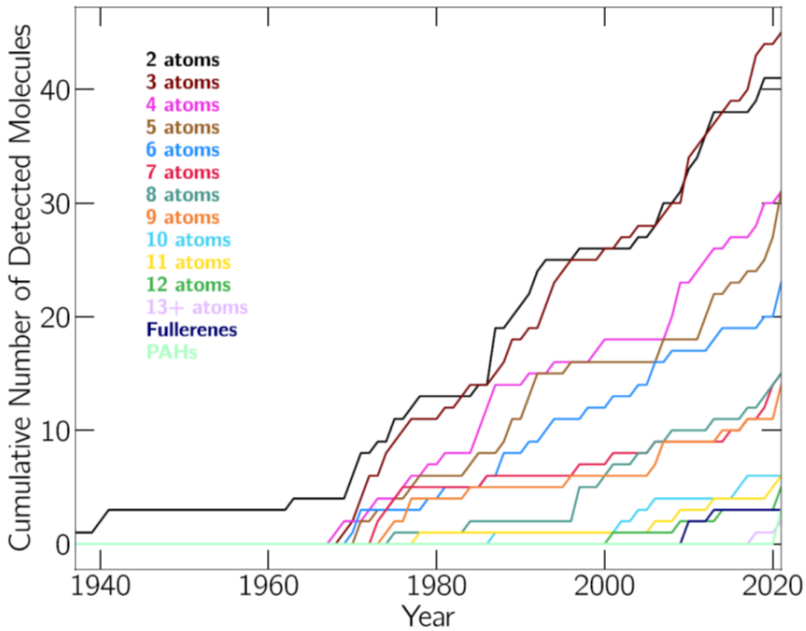

Figure 1.2: Cumulative number of detected ISM molecules as a function of time (as of 2021), separated into molecules composed of 2 to 13 atoms, as well as fullerenes and PAHs. Credit: McGuire (2022).

Molecular complexity

All known ISM molecules are composed of only 19 different chemical elements, most importantly H, C, N, O, and S. Most of these molecules are made of two or three atoms while the number of detected molecules decreases with increasing number of constructing atoms (see Fig. 1.2). This is largely due to the fact that larger, more complex molecules tend to be less abundant while also showing weaker emission features distributed over a larger bandwidth. It can be also seen from Fig. 1.2 that, even though some quite complex molecules such as CH_3CH_2OH and CH_3OCH_3 were detected very early on (Snyder et al., 1974; Zuckerman et al., 1975), molecules composed of 10 or more atoms started to become detected regularly only around 2000. The largest ISM molecules known to date are the fullerenes C_{60} and C_{70}, detected by Cami et al. (2010) in the infrared towards the planetary nebula Tc 1. Even though the fullerenes

are very large molecules, they are not very complex but rather simple, highly symmetric carbon structures that take the shape of hollow spheres. The PAH (polycyclic aromatic hydrocarbon) molecules referred to in Fig. 1.2 are two isomers of $C_{10}H_7CN$ (McGuire et al., 2021) as well as C_9H_8 (Cernicharo et al., 2021; Burkhardt et al., 2021). In contrast to the fullerenes, PAHs are very complex structures that are thought to be responsible for a lot of the absorption in various IR bands, yet it is difficult to assign spectral features to particular PAHs; however, note that the above PAHs were detected by their emission features in the radio range. In fact, it is assumed that 10 - 25 % of the interstellar carbon is bound in PAHs, which are likely formed in the envelopes of evolved stars (McGuire et al., 2021). It is furthermore theorized that interstellar carbon-rich dust might be formed in those environments by coagulation of PAHs (Frenklach and Feigelson, 1989; Cherchneff et al., 1992; Burkhardt et al., 2021).

Interstellar dust and gas

All interstellar molecules are either formed by gas phase reactions or reactions at the surface of dust grains, or both. In general, at the low densities of interstellar space, three-body gas phase reactions can virtually not occur, and only two-body reactions involving atoms, ions, small molecules, and electrons are possible. Because many (if not most) interstellar molecules have efficient surface reaction routes, a basic understanding of the formation and structure of interstellar dust is crucial for astrochemical research. As mentioned in the previous section, first considerations of the interactions between gas phase particles and dust grains go back to van de Hulst (1946) and Oort and van de Hulst (1946). Interstellar dust grains are generally assumed to be non-spherical, porous structures, that are composed of a mixture of mostly amorphous silicates and carbon, with sizes that range from nanometers to some tens of micrometers; the average grain size is commonly assumed to be 0.1 µm (Mathis et al., 1977; Mathis, 1996; Li and Draine, 2001; Min et al., 2007; Jones et al., 2013; Siebenmorgen et al., 2014; Zinner, 2014; Potapov et al., 2025). It is furthermore assumed that interstellar dust grains condense from the cooling gas in the envelopes around evolved stars and supernova remnants, depleting the gas from most of the refractory elements like Fe, Ni, Mg, etc. (Dorschner, 2003; Molster and Waters, 2003). Astronomical observations of interstellar dust are carried out mostly in the IR and optical ranges where

the dust is absorbing and scattering light from surrounding stars. Stellar radiation is also heating the dust, which re-emits parts of it as thermal radiation, peaking in the IR.

Table 1.1: ISM regions with their typical temperatures T, densities n(H), and states of matter. Values from: Draine (2011); van Dishoeck et al. (2013).

	T [K]	n(H) [cm^{-3}]	state of matter
hot ionized medium	$> 10^5$	~ 0.004	at.; ion.
H-II regions	$\sim 10^4$	~ 0.3	at.; ion.
H-I regions	100 – 5000	0.6 – 30	at.; ion., neut.
diffuse clouds	30 – 100	$\sim 10^2$	at., mol.; ion., neut.
molecular clouds	10 – 50	$\sim 10^4$	at., mol.; ion., neut.
starless cores	7 – 15	$> 10^5$	
protostellar cores	7 – 200	$10^5 - 10^9$	
circumstellar disks	7 – 3000	$10^6 - 10^{15}$	

at.: atomic; mol.: molecular; ion.: ionized; neut.: neutral

The gas-to-dust ratio in the ISM of the Milky Way is assumed to be around 100:1. The gas is largely dominated by H and He (together around 99 %), while the remaining ~ 1 % is mainly comprised of O, C, N, and S (as well as Ne). The temperature and density in the ISM vary by about five and ten orders of magnitude, respectively, while the pressure is roughly balanced (Friberg and Hjalmarson, 1990). It follows that, depending on the considered region, the elements in the gas phase are either in atomic or molecular form, while the atoms and molecules are either ionized or neutral. As mentioned in the previous section, the separation into regions where H is mostly in its neutral and ionized forms, i.e., H-I and H-II regions, respectively, was already introduced by Strömgren (1948). This separation is still in use today, while further separations are made for the hot ionized medium, diffuse clouds, and molecular clouds (Draine, 2011; van Dishoeck et al., 2013). Tab. 1.1 summarizes the major ISM regions and their characteristic temperatures and densities, as well as the predominant states of matter, i.e., atomic (at.), molecular (mol.), ionized (ion.), and neutral (neut.). Additional separations are made for major substructures of molecular clouds, namely (i) starless cores, i.e., dense cores

that might form a protostar in the future, (ii) protostellar cores, i.e., dense cores in which a protostar has formed at the center, and (iii) circumstellar disks around young stars. Note that the gas in protostellar cores and circumstellar disks is at the transition between being part of the ISM and part of a new stellar system. In the following, focus will be on processes in galactic molecular clouds.

Molecular clouds

In general, molecular clouds can be defined as gravitationally bound structures in which hydrogen is predominantly in its molecular form. In contrast to molecular clouds, diffuse clouds are transient structures bound by external pressure (Friberg and Hjalmarson, 1990). As discussed in the previous section, it was recognized around the midst of the last century that hydrogen should make a transition from H to H_2 in cold H-I regions. The efficient formation and accumulation of H_2 requires sufficient (dust) densities such that newly formed H_2 molecules are shielded by dust grains from destructive UV radiation. The distribution of interstellar gas and dust is commonly assumed to be well mixed, meaning that a high gas density corresponds to a high dust density. If the amount of H_2 becomes sufficiently high, self-shielding, i.e., the process in which new H_2 molecules are shielded by surrounding H_2 molecules, becomes efficient as well. The total gas mass in the galactic ISM is $> 10^9\,M_\odot$, while the ratio of molecular to atomic gas is ~ 0.3 (Dobbs et al., 2014; Molinari et al., 2014). Most of the molecular gas is located in molecular clouds, which can be further separated into giant molecular clouds ($\sim 10^7\,M_\odot$) close to the galactic center and smaller molecular clouds (or dark clouds; $\sim 10^2\,M_\odot$) in outer regions of the galactic disk and at high galactic latitudes (Dobbs et al., 2014).

Observations have shown that all nearby molecular clouds, including, e.g., Taurus, Perseus, and Ophiuchus, are pervaded by a network of dense filaments (André et al., 2010; Arzoumanian et al., 2011, 2019; Panopoulou et al., 2022; André et al., 2022, see Fig. 1.3). Those filaments are assumed to be the result of supersonic, turbulent motions in the ISM, induced by e.g., stellar feedback of massive stars, supernovae, and different sorts of gravitational and magnetic instabilities. The basic idea is that an elongated, line-shaped filament is created when two shock-fronts intersect. The density inside the filaments will be

higher relative to their surroundings, and if the density (or rather the mass per unit length) along the filaments exceeds a critical value, they will gravitationally collapse into denser, spheroidal aggregates, generally called starless cores.

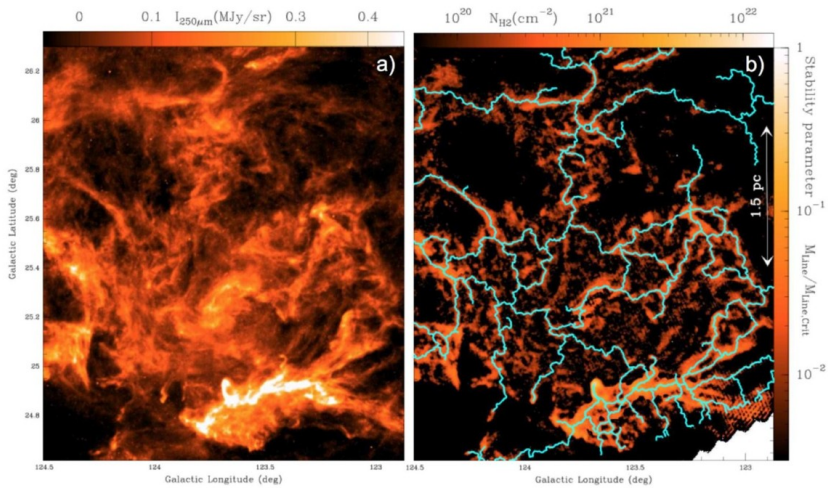

Figure 1.3: (a) Herschel 250 µm dust continuum map of a part of the Polaris Flare. (b) Corresponding H_2 column density map. The filamentary network in light blue has been derived with the *DisPerSe* algorithm. Given a typical filament width of ~ 0.1 pc, this map is equivalent to a map of mass per unit length along the filaments (expressed in terms of the stability parameter $M_{\rm L}/M_{\rm L,crit}$). Credit: André et al. (2014).

The critical line mass of a filament is generally defined as

$$M_{\rm L,crit} = \frac{2c_{\rm s}^2}{G}\,, \tag{1.1}$$

where c_s is the speed of sound and G is the gravitational constant (André et al., 2014). If a starless core is expected to form a protostar in the future, it is referred to as a prestellar core. Furthermore, and as already mentioned above, when a dense core has already formed a protostar at its center, it is called a protostellar core. It is emphasized in André et al. (2014) that the

first description of the internal filamentary structure of molecular clouds goes back to Barnard (1907), while the close relation between filamentary structure and the process of star formation has not been in the focus of research until recently.

Gas phase reactions in diffuse and molecular clouds

Even though the majority of interstellar molecules is formed within molecular clouds, the process of molecule formation already starts in diffuse clouds. According to Yamamoto (2017), 36 interstellar molecules are identified in diffuse clouds. Most of those species are comparatively simple ones like H_2, CO, and CN, while the most complex ones are NH_3, H_2CO, c-C_3H, and c-C_3H_2. As indicated in the previous paragraph, at the low densities of diffuse clouds, most molecules are easily dissociated by UV photons, so molecules do generally not reach high column densities. In addition, photoionization is efficient at low densities, so diffuse clouds are generally weakly ionized. H_2 is by far the most abundant interstellar molecule, formed exclusively on the surface of dust grains by the simple reaction

$$\mathrm{H(s) + H(s) \longrightarrow H_2(s)\,}, \tag{1.2}$$

where "(s)" marks a grain surface species. Thereby, the grain surface is needed to absorb the energy released by the formation of H_2, which, in free space, would immediately destroy the H_2 molecule as soon as it forms. Throughout diffuse clouds and molecular clouds, CO is the most abundant molecule after H_2, and because CO is easily detected by its strong radio emission, it is often used as a tracer of H_2 distribution; H_2 has no permanent electric dipole moment and therefore no simply $(J \to J-1)$ detectable rotational spectrum. In both diffuse clouds and molecular clouds, some of the most important reactions that form CO in the gas phase are

$$\mathrm{CH^*(g) + O(g) \longrightarrow CO(g) + H(g)\,}, \tag{1.3}$$
$$\mathrm{OH^*(g) + C(g) \longrightarrow CO(g) + H(g)\,}, \tag{1.4}$$
$$\mathrm{HCO^+(g) + e^- \longrightarrow CO(g) + H(g)\,}, \tag{1.5}$$

where "(g)" marks a gas phase species and the asterisk marks a radical. H_2O is another important molecule that already starts to form in the gas of diffuse

clouds via the electron recombination reaction

$$\mathrm{OH_3}^+(\mathrm{g}) + \mathrm{e}^- \longrightarrow \mathrm{H_2O}(\mathrm{g}) + \mathrm{H}(\mathrm{g})\,. \tag{1.6}$$

At the higher densities of molecular clouds, UV photons cannot penetrate deep into a cloud, and photodissociation is negligible. Therefore, molecules can accumulate in the gas phase, and once formed, molecules get mostly destroyed by reactions with He^+ and H^+. If one of these ions collides with a neutral molecule, it ionizes the target molecule by extracting an electron. Thereby, the difference in the ionization potentials between He (24.6 eV) or H (13.6 eV) and the target molecule can lead to the dissociation of the ionized molecule. Examples for this are

$$\mathrm{He}^+(\mathrm{g}) + \mathrm{CO}(\mathrm{g}) \longrightarrow \mathrm{C}^+(\mathrm{g}) + \mathrm{O}(\mathrm{g}) + \mathrm{He}(\mathrm{g}) \tag{1.7}$$

and

$$\mathrm{He}^+(\mathrm{g}) + \mathrm{H_2O}(\mathrm{g}) \longrightarrow \mathrm{OH}^+(\mathrm{g}) + \mathrm{H}(\mathrm{g}) + \mathrm{He}(\mathrm{g})\,. \tag{1.8}$$

Because of the lower ionization potential of H, reactions with H^+ may only ionize a target molecule without dissociation, as in

$$\mathrm{H}^+(\mathrm{g}) + \mathrm{OH}(\mathrm{g}) \longrightarrow \mathrm{OH}^+(\mathrm{g}) + \mathrm{H}(\mathrm{g}) \tag{1.9}$$

or

$$\mathrm{H}^+(\mathrm{g}) + \mathrm{H_2CO}(\mathrm{g}) \longrightarrow \mathrm{H_2CO}^+(\mathrm{g}) + \mathrm{H}(\mathrm{g})\,. \tag{1.10}$$

In molecular clouds, the only source of ionization are cosmic rays, which are negligible for ionization in diffuse clouds. The degree of ionization in molecular clouds it therefore lower than in diffuse clouds.

In the gas phase of molecular clouds, an efficient way of increasing the molecular complexity are hydrogenation reactions involving ions reacting with $\mathrm{H_2}$, such as

$$\mathrm{C_3}^+(\mathrm{g}) + \mathrm{H_2}(\mathrm{g}) \longrightarrow \mathrm{C_3H}^+(\mathrm{g}) + \mathrm{H}(\mathrm{g})\,, \tag{1.11}$$

$$\mathrm{C_3H}^+(\mathrm{g}) + \mathrm{H_2}(\mathrm{g}) \longrightarrow \mathrm{C_3H_2}^+(\mathrm{g}) + \mathrm{H}(\mathrm{g})\,, \tag{1.12}$$

$$\mathrm{C_3H}^+(\mathrm{g}) + \mathrm{H_2}(\mathrm{g}) \longrightarrow \mathrm{C_3H_3}^+(\mathrm{g}) + h\nu\,, \tag{1.13}$$

or

$$\mathrm{N^+(g) + H_2(g) \longrightarrow NH^+(g) + H(g)\,,} \tag{1.14}$$
$$\mathrm{NH^+(g) + H_2(g) \longrightarrow NH_2{}^+(g) + H(g)\,,} \tag{1.15}$$
$$\mathrm{NH_2{}^+(g) + H_2(g) \longrightarrow NH_3{}^+(g) + H(g)\,,} \tag{1.16}$$
$$\mathrm{NH_3{}^+(g) + H_2(g) \longrightarrow NH_4{}^+(g) + H(g)\,.} \tag{1.17}$$

Here, e.g., $\mathrm{C_3H_2{}^+}$ and $\mathrm{C_3H_3{}^+}$ can form the neutral carbon-chain molecules $\mathrm{C_3H}$ and $\mathrm{C_3H_2}$ via electron recombination, i.e.,

$$\mathrm{C_3H_2{}^+(g) + e^- \longrightarrow C_3H(g) + H(g)\,,} \tag{1.18}$$
$$\mathrm{C_3H_3{}^+(g) + e^- \longrightarrow C_3H_2(g) + H(g)\,.} \tag{1.19}$$

In the same way, $\mathrm{NH_3}$ can be formed from

$$\mathrm{NH_4{}^+(g) + e^- \longrightarrow NH_3(g) + H(g)\,.} \tag{1.20}$$

Another group of complex molecules are cyanopolyynes with the general formula $\mathrm{HC_nN}$, which can be formed in the gas phase by reactions of HCN with hydrocarbon ions. For instance, $\mathrm{HC_3N}$ can be formed via

$$\mathrm{C_2H_2{}^+(g) + HCN(g) \longrightarrow HC_3NH^+(g) + H(g)\,,} \tag{1.21}$$
$$\mathrm{HC_3NH^+(g) + e^- \longrightarrow HC_3N(g) + H(g)\,.} \tag{1.22}$$

However, the molecular complexity that can be reached by a "pure" gas phase chemistry is limited because the simplest type of hydrogenation reactions in which an H atom is added to another neutral species is prohibited for the same reason given above for the formation of $\mathrm{H_2}$, i.e., the reaction product is often unstable and would be dissociated by its own energy of formation. In contrast to this, the reaction products in the above hydrogenation reactions involving $\mathrm{H_2}$ are stabilized by the free hydrogen atom carrying away part of the reaction energy (Yamamoto, 2017). An exception is the radiative association reaction (1.13), in which the product it stabilized by spontaneous emission of a photon with energy $h\nu$.

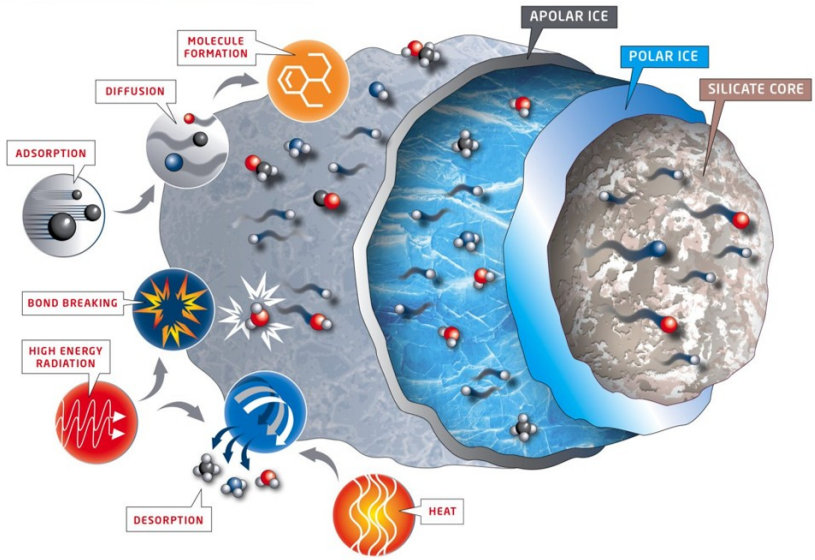

Figure 1.4: Interstellar grain surface chemistry: gas phase atoms and molecules can attach to refractory (silicate or carbonaceous) dust grains, move along the surface, and react with each other to form new molecules (see text for more information). Credit: https://blog.intercat.dk/2021/12/15/a-quick-look-into-my-research/ (Santos, J.; retrieval date: 2025-10-31).

The importance of grain surface reactions

This is why interstellar dust grains are an essential component to further increase the molecular complexity in molecular clouds: they provide the surface on which chemical reactions can take place, while also stabilizing the products of reactions such as $H + H \longrightarrow H_2$, prohibited in the gas phase. In general, gas phase atoms and molecules can stick to a dust grain and remain there for a considerable amount of time. Thereby, the strength with which a species is bound to the surface is controlled by its binding energy. Once stuck to a dust grain, a species can also move along the grain surface mainly by means of diffusion. However, the surface mobility of a species largely depends on grain temperature, and at a typical temperature of around 10 K, mostly H atoms are mobile. Furthermore, when two potential reaction partners meet at the same spot they can react to form a new species. Also, at any time, a surface species can desorb back into the gas phase via different types of desorption

mechanisms. Those grain surface processes are summarized in Fig. 1.4 and described in detail in, e.g., Tielens (2005), Cuppen et al. (2017), and Cuppen et al. (2024). It is worth noting that these processes are usually occurring at the surface or inside the bulk of interstellar ices around the dust grains rather than at the surface of the bare grains. However, for the sake of simplicity, we often collectively refer to them as "grain-surface" reactions.

Observations of interstellar ices

Observations of interstellar ices with infrared telescopes suggest that the first molecules that form at the surface of dust grains are mainly H_2O, CO_2, NH_3, and CH_4. The formation of these molecules starts at temperatures around 90 K and densities around $10^3\,\mathrm{cm}^{-3}$ (Boogert et al., 2008, 2015; Chuang et al., 2018, 2022), i.e., at the transition between diffuse clouds and molecular clouds. The surface formation of H_2O, NH_3, and CH_4 proceeds mainly via the subsequent hydrogenation of O, N, and C, respectively, i.e.,

$$\mathrm{O(s)} \xrightarrow{+\mathrm{H}} \mathrm{OH^*(s)} \xrightarrow{+\mathrm{H}} \mathrm{H_2O(s)}\,, \tag{1.23}$$

$$\mathrm{N(s)} \xrightarrow{+\mathrm{H}} \mathrm{NH^*(s)} \xrightarrow{+\mathrm{H}} \mathrm{NH_2{}^*(s)} \xrightarrow{+\mathrm{H}} \mathrm{NH_3(s)}\,, \tag{1.24}$$

$$\mathrm{C(s)} \xrightarrow{+\mathrm{H}} \mathrm{CH^*(s)} \xrightarrow{+\mathrm{H}} \mathrm{CH_2{}^*(s)} \xrightarrow{+\mathrm{H}} \mathrm{CH_3{}^*(s)} \xrightarrow{+\mathrm{H}} \mathrm{CH_4(s)}\,, \tag{1.25}$$

while most CO_2 is formed by the surface reaction

$$\mathrm{CO(s) + OH^*(s) \longrightarrow CO_2(s) + H(s)}\,. \tag{1.26}$$

It is interesting to note how close these observations are to the suggestion by van de Hulst (1946) that the composition of interstellar grains should be *transiently* dominated by H_2O, H_2, NH_3, and CH_4. Emphasizing the temporary component in this statement is important and very much true since, e.g., H_2 is only very transiently part of a dust grain because its high energy of formation and low binding energy leads to almost immediate release into the gas phase upon reaction. The other species mentioned above have much higher binding energies and can therefore accumulate at a dust grain surface, forming a mantle of molecular ice around the bare grain. The evolution of interstellar ices can span several millions of years, while passing through multiple phases of star-formation. However, the ice composition is always dominated by H_2O, as has been already speculated by Eddington (1937).

Another abundant component of interstellar ices is CO, which is however not formed at the surface of ices, but by the gas phase reactions (1.3), (1.4), and (1.5). CO becomes part of the ice mantles through freeze-out, i.e., accretion from the gas phase to an ice mantle, which starts to become effective at molecular cloud densities around $10^4\,\mathrm{cm}^{-3}$. At even higher densities around $10^5\,\mathrm{cm}^{-3}$, prevalent in dense molecular cloud cores, the freeze-out of CO onto grains becomes very efficient, and we speak of a so-called "catastrophic" CO freeze-out. The last major and securely identified component of interstellar ices is CH_3OH, which, according to many theoretical and experimental studies, is exclusively formed at the surface of dust grains via the subsequent hydrogenation of CO, i.e.,

$$\mathrm{CO\,(s)} \xrightarrow{+\mathrm{H}} \mathrm{HCO^*(s)} \xrightarrow{+\mathrm{H}} \mathrm{H_2CO\,(s)} \xrightarrow{+\mathrm{H}} \mathrm{CH_3O^*(s)} \xrightarrow{+\mathrm{H}} \mathrm{CH_3OH\,(s)} \quad (1.27)$$

(Watanabe and Kouchi, 2002; Garrod et al., 2006; Cuppen et al., 2009; Fuchs et al., 2009; Chang and Herbst, 2012; Chuang et al., 2018). The most commonly adopted picture that emerges from observations of interstellar ices separates between at least two major groups of layers. The lower layers are dominated by H_2O, CO_2, NH_3, and CH_4, while the upper layers are dominated by CO and CH_3OH (Boogert et al., 2015). However, the degree of separation/mixing between the different layers is subject of discussion. Recent observations by McClure et al. (2023) with the James Webb Space Telescope (JWST) towards two background stars tracing the ices in cold molecular clouds regions indicate that CH_3OH ice in the top layers is mixed with H_2O and CO ice. On the other hand, experiments by Müller et al. (2021) and comparison to observational data by Goto et al. (2021) and Penteado et al. (2015) indicate that CH_3OH and H_2O ices form separate layers on interstellar grains (see also Cuppen et al., 2011).

Besides the major ice species mentioned above, McGuire (2022) lists OCS, OCN^-, H_2CO, and HCOOH as additional identified species in interstellar ices, also listed in Boogert et al. (2015) as likely/possibly identified. This results in a total of 10 identified species (as of 2022), but we know that interstellar ices are made of many more molecules. However, securely assigning an infrared absorption feature to one unique molecule is much more difficult than e.g., assigning a radio emission line to its producing molecule. Part of the reason

for that is that many molecules share the same bonds (e.g, C – C, O – H, or C – O) or structural components (e.g., an OH or CH_3 group), which get vibrationally excited, i.e., absorb light, at the same or very similar wavelengths. In addition, ice species are never isolated but mixed with and loosely bound to surrounding species of different kind. Thereby, the relative abundances of species in a certain ice mixture can have drastic effects on e.g., the peak optical depth or width of absorption features. Also, when working with absorption spectra of interstellar ice analogues in the laboratory, only a limited number of components must be used to make sure that certain absorption features are securely assigned to specific molecules in the mixture, and to observe how these features change in shape when mixtures are changed. Eventually, limitations in the spectral characterization of interstellar ice analogues in the laboratory directly affect the interpretation of interstellar ice spectra, which is largely based on a comparison to laboratory data [Rocha, W.; priv. comm.]. Despite those difficulties related to the exact determination of interstellar ice compositions from observations, state-of-the-art infrared instruments like the JWST are promising tools to gain a better understanding of interstellar ices. For instance, recent studies of interstellar ices around protostars with JWST by Chen et al. (2024) and Rocha et al. (2024) claim detections of species such as CH_3CHO, CH_3OCHO, and CH_3CH_2OH.

Complex organic molecules

Even though we are only getting close to identifying more complex molecular species in interstellar ices, gas phase observations, experiments, and theoretical models suggest that they are there. In the remainder of this section, the focus will be on a particular group of interstellar molecules, called complex organic molecules (COMs), which are commonly defined as carbon-bearing molecules composed of at least six atoms. Following the early detections of gas phase COMs in warm protostellar environments, it was soon realized that gas phase reactions alone are not capable of explaining the abundances of observed COMs, but that grain-surface reactions must be contributing to the observed molecular complexity. Charnley (1997) first proposed a network of grain-surface chemical reactions that starts from CO and is capable of explaining the formation of many observed gas phase COMs by simple atom addition reactions involving H, O, C, and N (see Fig. 1.5). As mentioned above, CO is highly depleted onto dust grains in dense molecular cloud cores, and it is

assumed that at this stage, the surface formation of CH_3OH and other COMs becomes efficient.

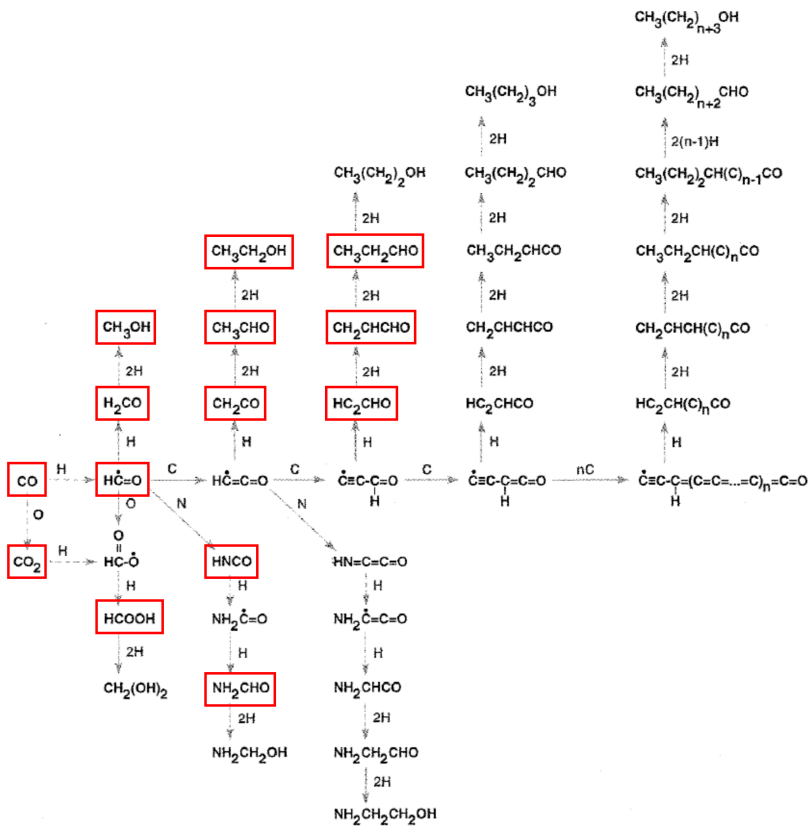

Figure 1.5: Grain surface chemistry seeded by CO. Broken arrows indicate reactions with activation energy barrier; arrows with "2H" indicate a barrier penetration reaction followed by an exothermic addition. Species observed in the ISM are marked in red. Credit: Charnley (2001).

Interestingly, a survey of starless and prestellar cores in the Taurus molecular cloud by Scibelli and Shirley (2020) has shown that gas phase CH_3OH, which is generally the simplest and best studied COM, is widely distributed

outside of dense cores and down to visual extinctions around 3 mag. Hence, the formation of CH_3OH and likely other COMs starts in dense regions of molecular clouds before the actual formation of dense cores. Priestley et al. (2025) arrive at very similar conclusions by combining hydrodynamical simulations of molecular clouds with a simple chemical network focusing on the formation of CH_3OH and CH_3CN. Further support for the early formation of COMs comes from observations of CH_3OH and larger COMs towards the so-called methanol hotspot in the Barnard 5 dark cloud (Taquet et al., 2017, see also paper B). Observations of gas phase COMs in cold environments further show that efficient non-thermal/-energetic desorption processes must be at work. A widely discussed candidate for this is so-called reactive desorption, i.e., the release of an ice species by its own energy of formation (Minissale et al., 2016; Chuang et al., 2018).

When ice-covered grains are incorporated into dense cores, the density and freeze-out of CO increases, which leads to a more efficient formation of CH_3OH and other COMs. Another survey of starless and prestellar cores in the Perseus molecular cloud by Scibelli et al. (2024) demonstrates that cores in which CH_3CHO is detected have higher CH_3OH abundances on average. In several of these cores with CH_3CHO detections, additional larger COMs, i.e., CH_3OCHO and/or CH_3OCH_3, are detected as well. In general, a higher abundance of CH_3OH in dense cores tends to correlate with the occurrence of more complex molecules. Eventually, if a protostar ignites at the center of a prestellar core, the released heat and radiation enables access to a whole new set of grain-surface chemical reactions, increasing the molecular complexity even further. Also, with increasing temperature, ice phase species are released when their respective sublimation temperature is exceeded, giving access to a much richer gas phase chemistry compared to cold and dense cores. We generally speak of a warm "hot core" or "hot corino" chemistry for high-mass and low-mass protostellar objects, respectively.

Warm carbon-chain chemistry

In the described scenario of a hot core/corino chemistry, mostly saturated COMs are formed at the surface of dust grains before being released into the gas phase to form the chemically rich envelopes around protostars. However, observations have shown that the chemistry of some protostellar cores is rather

dominated by unsaturated COMs, mostly carbon-chain molecules, while saturated COMs are depleted. Sakai and Yamamoto (2013) suggest that the differences in hot core/corino chemistry and the so-called warm carbon-chain chemistry (WCCC) are caused by different evolutionary timescales and with that, ice layering around the dust grains of the collapsing cores. In the more commonly considered hot core/corino scenario, core collapse is slowed down due to supporting mechanisms such as magnetic fields or turbulence. This causes the almost complete conversion of C atoms to CO molecules, which then freeze out onto dust grains with increasing density, burying earlier formed ice layers dominated by H_2O, CO_2, NH_3, and CH_4. As just described above, the CO molecules in the upper ice layers are then successively transformed into CH_3OH and other saturated COMs by simple atom addition reactions. In the WCCC scenario, core collapse proceeds much faster and the conversion from C to CO is incomplete, meaning that more C atoms can freeze out onto dust grains. This causes a more efficient production of CH_4 by hydrogenation of C (reaction 1.25) even in the outermost ice layers while the formation of CH_3OH and other larger saturated COMs is rather inefficient. When CH_4 comes off the grains during the warm-up phase, it triggers the formation of carbon-chain molecules by reactions with C^+. However, in the hot core/corino scenario, CH_4 is released together with large amounts of H_2O, which reacts with C^+ faster than CH_4, so no WCCC can be triggered. Therefore, both scenarios are largely exclusive.

Molecular transfer through phases of star-formation (?)

In general, the warm envelopes around young protostars are the environments with the highest molecular complexity in the ISM. However, as was discussed above, a relatively high molecular complexity can be reached in molecular clouds even before the formation of dense cores. One major question of interest in astrochemistry is to what degree the observed molecular complexity is transferred through different phases of star-formation. This question is tightly related to astrobiological research, because theories, experiments, and observations imply that important biologically relevant molecules could already form in interstellar space before becoming part of a protoplanetary disk and the growing planetary bodies inside (Kvenvolden et al., 1970; Hoyle and Wickramasinghe, 1977; Ehrenfreund and Charnley, 2000; Cooper et al., 2001; Ehrenfreund et al., 2001; Callahan et al., 2011; Garrod, 2013; Koga

and Naraoka, 2017; Nuevo et al., 2018; Furukawa et al., 2019; Oba et al., 2019; Hadraoui et al., 2019; Ioppolo et al., 2021, see also the following section 1.3 and paper A). However, models cannot describe the complete physical and chemical evolution of a growing stellar system from a collapsing molecular cloud filament, and neither can we observe this process for one single system in space, or simulate it in the laboratory. This means that, in order to approach this question, we need to piece together information from many astrochemical/-physical specializations because, in addition to laboratory data and theoretical models (for sub-parts of the star-formation process), observational data is needed from gas and ice phase observations towards starless cores, prestellar cores, protostellar cores, circumstellar disks, and exoplanetary atmospheres. However, differences in the physical and chemical conditions as well as evolutionary stages and dynamic timescales can be huge even for the members of the same group of objects, which can make it difficult to make comparisons and draw conclusions. After all, we are left with slowly but surely putting together the bits and pieces of the puzzle to create a successively more complete picture.

1.3 Relation to Other Fields

Astrophysics

As described in section 1.1, astrochemistry evolved from astrophysical research on the properties of the interstellar medium. Many of those properties are studied via atomic and molecular tracers, so there is still a very large overlap between the fields of (mainly interstellar) astrophysics and astrochemistry. Some examples are listed below without providing the methodological or physical background.

- Spectral line emission is generally an important gas cooling mechanism in the ISM, and the measurement of certain spectral lines can reveal insights into the major cooling pathways.

- At LTE (local thermodynamic equilibrium), the gas kinetic temperature of a source can be determined from rotation diagrams. Optically thick CO emission as well as emission from NH_3 and other symmetric top molecules such as methyl acetylene (CH_3CCH) are also commonly used tracers of the kinetic temperature.

- CO emission can reveal information about the density of an environment as it gets depleted from the gas phase with increasing density in molecular clouds. Measurements of CO gas mass/distribution are commonly used to infer the H_2 gas mass/distribution.

- Different molecules (or molecular transitions) have different so-called critical densities, i.e., the threshold density that must be exceeded in order to maintain the population of an upper energy level by collisions with H_2. Therefore, the occurrence and intensity distribution of certain spectral lines can be used as density tracers.

- The shape and position of spectral lines are important diagnostic tools to study gas kinematics, including infall and outflow motions, rotational motions, and turbulence. Also, the occurrence of certain molecules such as SiO can indicate past shock events.

- Isotope ratios like D/H can be used to derive information about source physical conditions as the fractionation of isotopes in different molecules is directly dependent on physical conditions such as temperature. Isotope ratios and molecule ratios (e.g., D/H, N_2H^+/CO) can also be used to derive estimates of source age or evolutionary stage.

- Measurements of ion/neutral ratios can reveal information about the ionization fraction of a source. Furthermore, the abundances of certain ions such as $H_3{}^+$, H_2O^+, or OH^+ can provide insights into the cosmic ray ionization rate.

Astrobiology

Just as astrochemistry, astrobiology is a fairly young discipline and deals with the study of life in the universe. This includes characterizing the prerequisites for the development of life on other planetary bodies, based on what we know about the development of life on Earth. Therefore, astrobiology requires a lot of input from other fields such as biochemistry, microbiology, geology, paleontology, planetology, and exoplanetary research.

Astrochemistry and astrobiology are tightly linked by the hypothesis that biologically relevant molecules are already formed in interstellar space before being transferred to protoplanetary disks around young stars and the growing

planetary bodies inside. For example, it has long been speculated that the simplest biotic amino acid glycine (NH_2CH_2COOH) could form in interstellar space, but despite many efforts spanning several decades of observations (e.g., Brown et al., 1979; Snyder et al., 1983; Combes et al., 1996; Jones et al., 2007; Drozdovskaya et al., 2019), no clear detection could be made yet. Paper A of this thesis deals with the search for glycine towards the so-called methanol hotspot in the Barnard 5 dark cloud. Hadraoui et al. (2019) find indications that cometary glycine might be inherited from interstellar space, while experiments and theoretical models by Ioppolo et al. (2021) show that glycine can form at low temperatures without the need of energetic ice-processing. Other experimental studies by Nuevo et al. (2018) and Oba et al. (2019) further indicate that nucleobases and sugars can be produced on interstellar ices. In addition, some potential precursors of biomolecules have been identified in interstellar space. Examples are formamide (NH_2CHO; Rubin et al., 1971), methylamine (CH_3NH_2; Kaifu et al., 1974), and glycolaldehyde (CH_2OHCHO; Hollis et al., 2000). Formamide and methylamine are respectively considered precursors of nucleobases and amino acids, while glycolaldehyde is considered an important precursor of the RNA sugar ribose. More recent detections include hydroxylamine (NH_2OH) and urea (NH_2CONH_2), which are both considered precursors of RNA ribonucleotides (Jiménez-Serra et al., 2020; Rivilla et al., 2020). Further interesting detections are ethanolamine ($NH_2CH_2CH_2OH$; Rivilla et al., 2021; Zeng et al., 2021), i.e., an important cell membrane molecule, and the four-carbon sugar erythrulose ($HOCH_2CH(OH)COCH_2OH$; Jiménez-Serra et al., 2026).

Another overlap between astrochemistry and astrobiology is the search for biomarkers in the atmospheres or oceans of other planetary bodies of the solar system, as well as in the atmospheres of exoplanets. Recently, the tentative detection of dimethyl sulfide (CH_3SCH_3) in the atmosphere of exoplanet K2-18b (Madhusudhan et al., 2025) was interpreted as a potential sign of the presence of life, because on Earth, dimethyl sulfide is mainly produced by marine life such as algae and plankton. However, another study reports the detection of dimethyl sulfide in the interstellar medium (Sanz-Novo et al., 2025), which shows that it can form abiotically.

Cosmochemistry, Planetology, and Geology

The study of the chemical composition and evolution of the planetary bodies of the solar system is linked to astrochemistry largely by the study of protoplanetary disks around young stars. That is, as a first-order principle, we generally assume a correlation between the chemical composition of a planet-forming disk at a certain radial distance from the central star and the composition of a growing planetary body at that distance. This basic principle is reflected by the very different compositions of the terrestrial planets of the inner solar system and the gaseous and icy planets and planetary bodies of the outer solar system. Essentially, the abundances of volatile species such as CO, H_2O, NH_3, and CH_4 vary drastically among physical phases as a function of temperature, i.e., as a function of radial distance. At low radial distances, temperatures are high, and volatile species are in the gas phase. Hence, the composition of planets forming close to the central star is dominated by refractory elements, largely bound in metal and silicate particles. At larger radial distances, temperatures are low such that volatiles are available in their solid state as ices, which can easily get incorporated into growing planetary bodies. The study of so-called "snow-lines" or condensation fronts, i.e., the distance at which a molecules makes the transition from its gaseous to its solid state, is very prominent in the research of protoplanetary disks (Dutrey et al., 2014; Pontoppidan et al., 2014).

The long-standing question for the origin of Earth's surface water is also bridging the gap between solar system sciences and astrochemistry. Given that water was only available as a gas or bound in certain water-rich minerals in the terrestrial planet-forming zone, it is often assumed that water-rich planetesimals, asteroids, and comets have delivered water to the surface of the young Earth. Alternatively, pebble accretion and direct gas accretion are discussed as well (Johansen et al., 2021; Perotti et al., 2023). The D/H ratio of Earth's ocean water is generally comparable to the D/H ratio of cometary and asteroidal water (Cordiner et al., 2025), which is regarded as an evidence that at least part of Earth's water was delivered by comets. Furthermore, abundant deuterated and especially doubly deuterated water in protostars, protoplanetary disks, and comets is considered as an evidence for the inheritance of water from the molecular cloud phase (van Dishoeck et al., 2014; Ceccarelli et al., 2014; Leemker et al., 2025). Since interstellar water ice is

mixed with other species such as COMs, this might be furthermore seen as an indication for the transfer of more complex molecules from the molecular cloud stage to the planet-forming stage. However, water has a significantly higher sublimation temperature than most other interstellar ices, such that it resides on dust grain surfaces for longer periods of time during the warm-up phase of star-formation. Nevertheless, it is feasible that water- and COM-rich interstellar ices might be incorporated into comets and other pristine bodies in the outskirts of a protoplanetary disk where temperatures are low and shielding from destructive stellar radiation is high. In turn, this would also have important astrobiological implications.

CHAPTER 2

Physics Background

This chapter summarizes important concepts and equations related to the occurrence, detection, and modeling of spectral line radiation emitted by molecules in cold interstellar gas. Section 2.1 covers two fundamental concepts, i.e., the Boltzmann distribution and Planck's law of thermal radiation, which are widely used throughout this work. Sections 2.2 and 2.3 then cover the basics of rotational spectroscopy and the population of molecular (rotational) energy levels, i.e., the theoretical frameworks explaining the occurrence and intensity of spectral line emission. Next, section 2.4 introduces the equations of radiative transfer, which form the basis for the modeling of spectral line intensities. Lastly, sections 2.5 and 2.6 discuss important concepts related to the shape of molecular emission lines and their detection with radio telescopes.

2.1 Basic Concepts

This section introduces the basic equations of two fundamental physical concepts used throughout this work, i.e., the Boltzmann distribution and Planck's law of thermal radiation.

The Boltzmann Distribution

One of the most fundamental concepts in physical chemistry is the Boltzmann distribution. It is a measure of how the energy of a collection of particles (e.g., atoms, ions, or molecules) is distributed in thermal equilibrium at a certain temperature. The term "thermal equilibrium" describes a steady state in the energy distribution, meaning that there is no net change of energy between the particles.

Assuming a total number of particles n_{tot} of the same kind, the Boltzmann distribution calculates the number of particles n_i with energy E_i as a fraction of n_{tot} and as a function of temperature T, i.e.,

$$\frac{n_i}{n_{\text{tot}}} = \frac{1}{q} \exp\left(-\frac{E_i}{k_{\text{B}}T}\right), \tag{2.1}$$

where q is a partition function (acting as a normalization constant), defined as

$$q = \sum_i \exp\left(-\frac{E_i}{k_{\text{B}}T}\right), \tag{2.2}$$

and k_{B} is the Boltzmann constant (Atkins et al., 2018). It can be seen that, as the temperature increases, higher energy states are populated at the expense of states with lower energy (see Fig. 2.1).

The Boltzmann distribution can also be used to calculate the number of particles in one state with energy E_i relative to the number of particles in another state with energy $E_j > E_i$ (Atkins et al., 2018), i.e.,

$$\frac{n_i}{n_j} = \exp\left(-\frac{(E_j - E_i)}{k_{\text{B}}T}\right) = \exp\left(-\frac{\Delta E}{k_{\text{B}}T}\right). \tag{2.3}$$

Here, it becomes apparent that the relative population of any two states decreases as the energy separation between the considered states increases.

It is furthermore important to note the distinction between energy states and energy levels (Atkins et al., 2018). Eq. (2.3) calculates populations of energy states, but several states might have the same energy, and any one of these states has the same population. This effect can be considered when instead calculating the relative population of energy levels, by taking into account the degeneracies (statistical weights) g_i and g_j of the levels with energies E_i and E_j. Eq. (2.1) then becomes

$$\frac{n_i}{n_{\text{tot}}} = \frac{g_i}{Q} \exp\left(-\frac{E_i}{k_{\text{B}}T}\right) \tag{2.4}$$

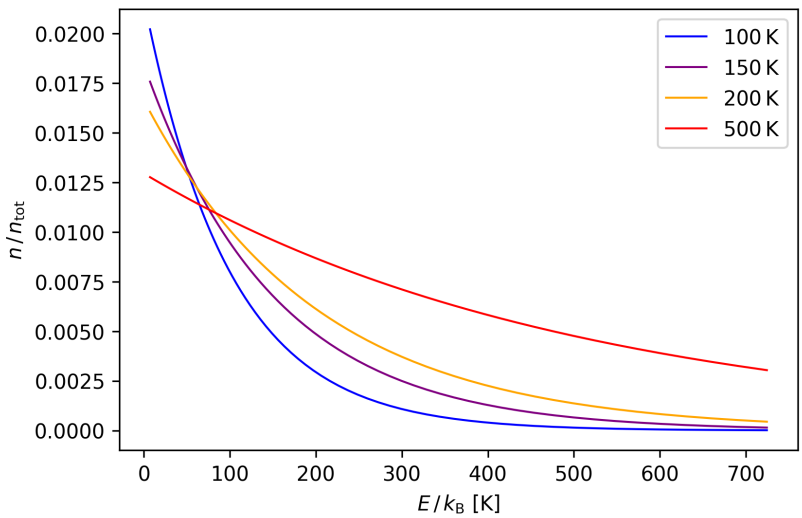

Figure 2.1: Arbitrary Boltzmann distribution for a collection of particles at different temperatures, according to Eq. (2.1) and assuming a continuous range of energies. With increasing temperature, the number of particles in higher energy states increases at cost of the number of particles in lower energy states.

with partition function

$$Q = \sum_i g_i \exp\left(-\frac{E_i}{k_\mathrm{B}T}\right), \tag{2.5}$$

while Eq. (2.3) becomes

$$\frac{n_i}{n_j} = \frac{g_i}{g_j} \exp\left(-\frac{\Delta E}{k_\mathrm{B}T}\right). \tag{2.6}$$

Planck's Law of Thermal Radiation

Another important concept that is frequently used for the interpretation and modeling of astronomical data is Planck's law of thermal radiation, describing the properties of blackbody radiation. Conceptually, a blackbody is an object in thermal equilibrium with its surroundings, absorbing all electromagnetic radiation it receives. In order to stay in equilibrium, a blackbody has to emit radiation at the same rate as it absorbs it (Atkins et al., 2018). Although perfect blackbodies do not exist in nature, the radiation emitted by many natural objects like stars, planets, light bulbs, and also humans can be approximated to a high degree as blackbody radiation in a certain frequency range (Bennett et al., 2010).

Assuming a spherical blackbody at a certain distance from an observer, Planck's law of thermal radiation can be used to calculate the spectral intensity $B_\nu(T)$ of the body. The spectral intensity gives the emitted energy E per unit time t, per unit frequency ν[1], per unit solid angle Ω, received per unit area A, i.e.,

$$B_\nu(T) = \frac{\mathrm{d}E}{\mathrm{d}t\,\mathrm{d}\nu\,\mathrm{d}\Omega\,\mathrm{d}A}, \tag{2.7}$$

such that it has dimensions of $\mathrm{J\,s^{-1}\,Hz^{-1}\,sr^{-1}\,m^{-2}}$. The emitted energy, which is proportional to the number of photons emitted per unit solid angle, is the same in each direction of space. However, the received energy, proportional to the number of photons collected per unit area, depends on the distance to the observer. The emitted energy furthermore depends on the considered frequency range. According to Planck's law, the spectral intensity is calculated

[1] Equivalent expressions can be given in terms of wavelength or wavenumber.

as

$$B_\nu(T) = \frac{2h\nu^3}{c^2}\left[\exp\left(\frac{h\nu}{k_\mathrm{B}T}\right) - 1\right]^{-1}, \tag{2.8}$$

where h is the Planck constant, ν is the frequency, c is the speed of light, k_B is the Boltzmann constant, and T is the temperature.

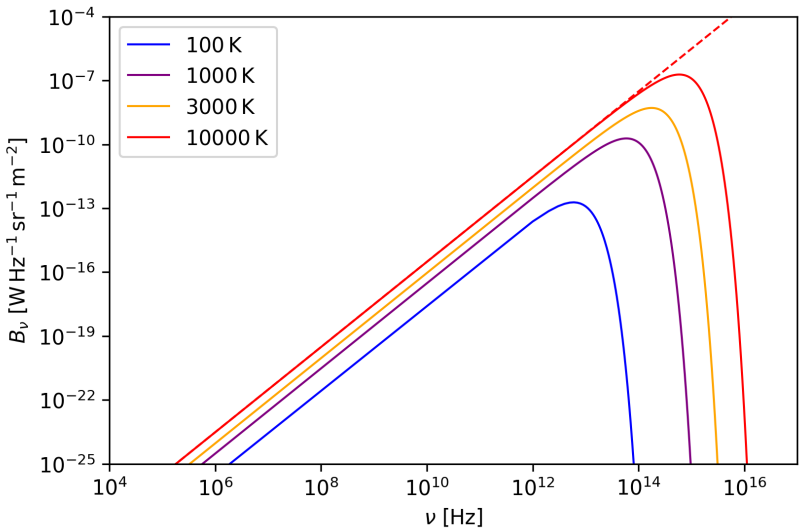

Figure 2.2: Spectral intensity $B_\nu(T)$ of blackbody radiation for a range of frequencies and different temperatures, calculated from Eq. (2.8). With increasing temperature, the peak spectral intensity shifts towards higher frequencies while the total intensity ($\int B_\nu(T)\,\mathrm{d}\nu$) increases. The red dashed line indicates the Rayleigh-Jeans approximation (Eq. 2.10) for 10 000 K.

The explicit units of $B_\nu(T)$ are $\mathrm{J\,m^{-2}}$, which means that the remaining units, i.e., $\mathrm{s^{-1}\,Hz^{-1}\,sr^{-1}}$, are implicit[2]. Integrating the spectral intensity over frequency gives the total intensity $B(T)$ of the body, i.e.,

$$B(T) = \int_0^\infty B_\nu(T)\,\mathrm{d}\nu\,. \tag{2.9}$$

[2]Even though the units of time and frequency cancel each other, they should be kept to keep track of the complete physical setting.

Fig. 2.2 shows the spectral intensity of blackbody radiation for a range of frequencies and different temperatures. It can be seen that, as the temperature increases, the peak spectral intensity is shifting towards higher frequencies (Wien's displacement law) while the total intensity, described by Eq. (2.9), increases.

An important approximation to Planck's law often used in radio astronomy is the so-called Rayleigh-Jeans approximation. It is a good approximation to the spectral intensity of a blackbody in the limit $h\nu \ll k_\mathrm{B}T$, i.e., in the linear part of the graphs in Fig. 2.2, and is simply written as

$$B_\nu(T) = \frac{2k_\mathrm{B}T\nu^2}{c^2} \tag{2.10}$$

(Condon and Ransom, 2016). In fact, before Planck's invention of energy quantization, the Rayleigh-Jeans approximation was the best theoretical description of experimentally derived blackbody spectra. However, it is only a good description at low frequencies, while the modelled intensities are going to infinity at higher frequencies (see red dashed line in Fig. 2.2). This behavior became known as the "ultra-violet catastrophe" (Atkins et al., 2018). Essentially, Planck's law can also be written as a combination of the Rayleigh-Jeans approximation and a quantum correction factor α, i.e.,

$$B_\nu(T) = \frac{2k_\mathrm{B}T\nu^2}{c^2}\alpha\,, \tag{2.11}$$

with

$$\alpha = \frac{h\nu}{k_\mathrm{B}T}\left[\exp\left(\frac{h\nu}{k_\mathrm{B}T}\right) - 1\right]^{-1}. \tag{2.12}$$

One can conclude that the intensity of a blackbody is well described by the Rayleigh-Jeans approximation only if $\alpha \to 1$ (Condon and Ransom, 2016).

2.2 Rotational Spectroscopy

At very low temperatures, characteristic for cold ($< 10-50\,\mathrm{K}$) molecular cloud sources, molecules are mostly in their electronic and vibrational ground states, and only their rotational energy levels are populated. Therefore, the spectral

line radiation from cold molecular clouds is mainly produced by transitions between distinct molecular rotational energy levels[3]. Photons associated with such transitions have frequencies in the radio range of the electromagnetic spectrum, and can be observed with single-dish radio telescopes or interferometers. This section first introduces the classification scheme of molecules in the framework of rotational spectroscopy. Then, the basic equations for the calculation of rotational energy levels and spectra are discussed along with some crucial related concepts.

Molecular Classification

In the framework of rotational spectroscopy, molecules can be separated into five major classes, based on their moment of inertia (MoI). The MoI of any 3D body is described by a symmetric, second-rank tensor $\boldsymbol{I}$. If it is assumed for an arbitrary molecule that the underlying coordinate system (with origin at the center of mass) rotates when the molecule rotates (molecule-fixed axes), the MoI tensor becomes diagonal, and is written as

$$\boldsymbol{I} = \begin{pmatrix} I_a & 0 & 0 \\ 0 & I_b & 0 \\ 0 & 0 & I_c \end{pmatrix} , \tag{2.13}$$

where I_a, I_b, and I_c are the principal MoI components (Gordy and Cook, 1984; Hollas, 1998, 2004; Yamamoto, 2017). Using the principal axes theorem, the MoI tensor can be further transferred into its quadric form, which describes the surface of an ellipsoid, i.e.,

$$f(\mathbf{x}) = \left(\frac{x_1}{\sqrt{1/I_a}} \right)^2 + \left(\frac{x_2}{\sqrt{1/I_b}} \right)^2 + \left(\frac{x_3}{\sqrt{1/I_c}} \right)^2 . \tag{2.14}$$

In rotational spectroscopy, it is convention to chose that

$$I_c \geq I_b \geq I_a \tag{2.15}$$

[3]It is also possible to observe rotational transitions of molecules in their first excited vibrational states at relatively low temperatures, but the focus here is on pure rotational spectra.

(Hollas, 2004; Atkins et al., 2018). In that case, and depending on the actual values of the principal MoI components, the quadric surface representing the MoI tensor will assume different shapes (Hollas, 1998, see Fig. 2.3):

(1) if $I_c = I_b = I_a$, the quadric surface is a sphere,

(2) if $I_c = I_b > I_a$, the quadric surface is a prolate spheroid,

(3) if $I_c > I_b = I_a$, the quadric surface is an oblate spheroid, and

(4) if $I_c \neq I_b \neq I_a$, the quadric surface is a triaxial ellipsoid.

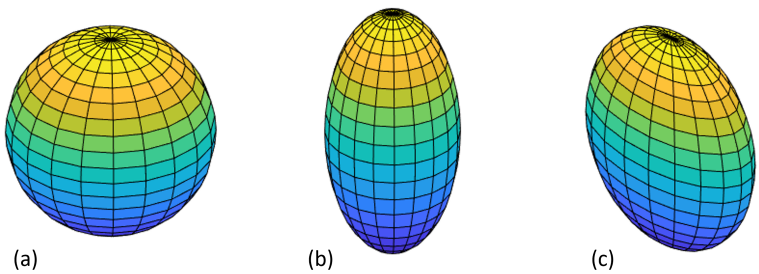

Figure 2.3: Ellipsoidal quadric surfaces resulting from different, relative MoI components (I_a, I_b, and I_c) in Eq. (2.14): (a) sphere ($I_c = I_b = I_a$), (b) prolate spheroid ($I_c = I_b > I_a$), (c) oblate spheroid ($I_c > I_b = I_a$). A triaxial ellipsoid ($I_c \neq I_b \neq I_a$) is a mixture of figures (b) and (c).

The classification of molecules in rotational spectroscopy follows directly from the four cases above (Hollas, 1998, 2004; Yamamoto, 2017):

(1) molecules with $I_c = I_b = I_a$ are called spherical rotors,

(2) molecules with $I_c = I_b > I_a$ are called prolate symmetric rotors,

(3) molecules with $I_c = I_b > I_a = 0$, i.e., special cases of (2), are called linear rotors,

(4) molecules with $I_c > I_b = I_a$ are called oblate symmetric rotors, and

(5) molecules with $I_c \neq I_b \neq I_a$ are called asymmetric rotors.

In fact, those five classes can be reduced to three when summing up classes (2), (3), and (4) under the term symmetric rotors (Atkins et al., 2018). As can be seen, the symmetry of molecules decreases from class (1) to class (5). Based on that, the equations for the calculation of rotational energies become increasingly more complex with increasing molecular asymmetry.

Rotational Energy Levels, Spectra, and Selection Rules

The rotational energy of a molecule is a quantized property, and the rotational energy eigenvalues can be obtained by solving the time-independent Schrödinger equation with the rotational Hamiltonian operator. This way, analytical expressions for the calculation of rotational energies can be found for all molecular classes, except asymmetric rotors. For that class, it is necessary to use the concepts of matrix mechanics to derive approximate solutions[4] (Gordy and Cook, 1984; Hollas, 2004; Yamamoto, 2017; Atkins et al., 2018). In this section, I will not cover the explicit equations for the calculation of rotational energies for the different molecular classes, but rather give a broad overview about some important concepts and approaches.

As a first order approximation, molecules in rotational spectroscopy can be considered as point-masses connected by stiff (rigid) interatomic axes with fixed lengths. This picture of a molecule is summarized under the term rigid rotor approximation. However, the interatomic axes of a molecule are actually not rigid, but undergo lengthening due to centrifugal forces upon rotation. Considering this effect in the calculation of rotational energies requires the use of molecule-dependent rotational distortion constants (Gordy and Cook, 1984; Yamamoto, 2017; Atkins et al., 2018). Distortion constants are a measure of stiffness along the bonds in a molecule (Atkins et al., 2018) and tabulated values (derived from experiments or theory) can be found for many molecules in the literature or in databases.

The rotational energies of all molecular classes are described by at least two good quantum numbers $J = 0, 1, 2, \ldots$ and $M_J = \pm 1, \pm 2, \ldots, \pm J$, which are the respective spectroscopic equivalents of the total angular momentum

[4] In matrix mechanics, quantum mechanical operators are treated as matrices, and the problem of solving the Schrödinger equation is shifted to a matrix diagonalization problem (Gordy and Cook, 1984).

quantum number and the magnetic quantum number, defined for the general case of a rotating quantum object. In the absence of a surrounding electromagnetic field, the rotational energies of a molecules do not directly depend on the value of M_J. However, each level is $(2J + 1)$-fold degenerate because there are $2J + 1$ values of M_J for each value of J. The independence of the rotational energy on quantum number M_J can be interpreted in the sense that the energy is independent of the direction of rotational motion (Atkins et al., 2018). The quantum numbers J and M_J are sufficient for the description of spherical and linear rotor molecules. However, additional quantum numbers are required for more complex molecules with lower symmetry (i.e., prolate and oblate rotors and asymmetric rotors), and if spectral fine and hyperfine structures are considered (Gordy and Cook, 1984; Hollas, 2004; Hirota, 2011; Yamamoto, 2017; Atkins et al., 2018).

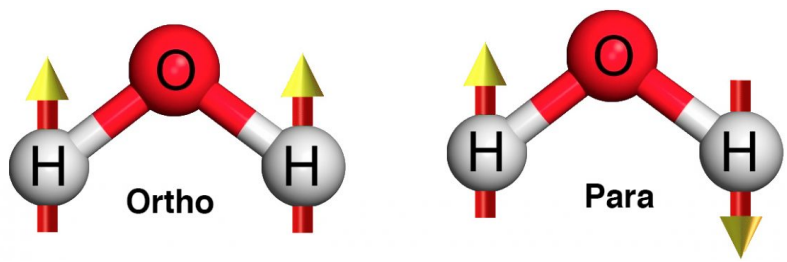

Figure 2.4: Parallel and anti-parallel spins of the otherwise identical hydrogen nuclei in water give rise to two spectroscopically separable forms of water, i.e., ortho-H_2O and para-H_2O. Credit: https://marchenry.org/2014/03/19/separation-orthopara/ (Natur'Eau Quant; retrieval date: 2024-01-20).

In the presence of an external electromagnetic field, interactions between a molecule and the field electrons can give rise to fine-splittings in molecular rotational spectra due to effects like the Zeemann effect (magnetic field) or the Stark effect (electric field) (Gordy and Cook, 1984). For example, the Stark effect partly removes the degeneracy associated with the quantum number $M_J = 0, \pm 1, \pm 2, \ldots, \pm J$ such that the rotational energy levels of a molecule become split into J sub-levels, where each sub-level except the one associated with $M_J = 0$ is doubly degenerate (Hollas, 2004; Atkins et al., 2018). In addition to interactions with external field electrons, "internal" coupling interactions of the electron spin and orbital angular momenta among themselves

as well as with the nuclear spin angular momentum and the total molecular angular momentum can cause fine and hyperfine splittings of rotational energy levels. Such interactions occur in molecules with one or more unpaired electrons (often in radicals such as OH^*, CH^*, or CN^*) and/or non-zero electron orbital angular momentum, as well as in molecules with at least one nucleus with non-zero nuclear spin angular momentum. Examples for the latter case include molecules that contain e.g., H ($I = 1/2$), D ($I = 1$), ^{13}C ($I = 1/2$), N ($I = 1$), or ^{15}N ($I = 1/2$); I is the nuclear spin quantum number (Hirota, 2011; Mangum and Shirley, 2015; Yamamoto, 2017).

An important point to note is that some molecules (including H_2, H_2O, CH_3OH, and CH_4) can be spectroscopically separated into two or more symmetry forms based on the relative nuclear spin of their constructing hydrogen nuclei (Chapovsky and Hermans, 1999). For example, the two hydrogen nuclei in water can have parallel spins or anti-parallel spins, leading to the definitions of ortho-H_2O and para-H_2O, respectively (see Fig. 2.4). Molecules can also have multiple stable atomic configurations (conformers), giving rise to a slightly different rotational behavior, and therefore, different rotational energies. One example is glycine (NH_2CH_2COOH), which has several stable conformers (see also Fig. 1, paper A; Hu et al., 1993).

In the matrix mechanics formalism, the rotational energy eigenvalues E_J of a molecule can be found by diagonalization of the Hamiltonian matrix for rotational motion $\hat{\boldsymbol{H}}_\mathbf{r}$, i.e., (neglecting centrifugal distortion)

$$E_J = \langle \psi_{J,M_J} | \, \hat{\boldsymbol{H}}_\mathbf{r} \, | \psi_{J,M_J} \rangle = \langle J, M_J | \, \hat{\boldsymbol{H}}_\mathbf{r} \, | J, M_J \rangle \, . \tag{2.16}$$

For a molecule-fixed coordinate system with principal axes a, b, and c, the rotational Hamiltonian matrix has the form

$$\hat{\boldsymbol{H}}_\mathbf{r} = \frac{1}{2} \left(\frac{\hat{\boldsymbol{L}}_a^2}{I_a} + \frac{\hat{\boldsymbol{L}}_b^2}{I_b} + \frac{\hat{\boldsymbol{L}}_c^2}{I_c} \right) = \frac{\hat{\boldsymbol{L}}^2}{2I} \, , \tag{2.17}$$

where $\hat{\boldsymbol{L}}$ is the total angular momentum operator. It can be shown that its corresponding eigenvalues are

$$\langle J, M_J | \, \hat{\boldsymbol{L}} \, | J, M_J \rangle = \hbar J(J+1) \, . \tag{2.18}$$

Furthermore, the eigenvalues of the square magnitude of angular momentum are

$$\langle J, M_J | \, \hat{\boldsymbol{L}}^2 \, | J, M_J \rangle = \hbar^2 J(J+1) \, . \tag{2.19}$$

The exact form of the Hamiltonian matrix changes for the different classes of molecules based on their symmetry and the related moment of inertia components (Gordy and Cook, 1984; Hollas, 2004; Yamamoto, 2017; Atkins et al., 2018).

In spectroscopy, the quantity that is actually measured is not energy but frequency[5]. Therefore, energies are commonly converted to so-called term values with dimensions of frequency (Yamamoto, 2017; Atkins et al., 2018). In general, assuming a set of discrete rotational energies $\boldsymbol{E}_{\mathbf{rot}}$, the corresponding term values $\boldsymbol{F}$ are calculated as

$$\boldsymbol{F} = \frac{\boldsymbol{E}_{\mathbf{rot}}}{h} \, . \tag{2.20}$$

Furthermore, using the term value expression, the transition frequency ν for a transition between any two levels with F_i and F_j (where $F_i > F_j$) is given by

$$\nu = F_i - F_j \, . \tag{2.21}$$

A set of such transition frequencies is what generally defines a rotational spectrum. Of course, similar expression are found for electronic and vibrational energies.

It is important to stress that not all transitions between any pairs of energy levels are also allowed. In general, time-dependent perturbation theory is used to derive the spectroscopic selection rules that govern which transitions are allowed and forbidden. Thereby, if the transition rate between two distinct energy levels is zero, this transition is called forbidden. Conversely, all transitions with non-zero transition rates are allowed transitions. By using semi-classical radiation theory, it can be shown that all possible transitions between rotational energy levels of molecules without a permanent electric dipole moment have zero transition rates. Therefore, such molecules are usually not able to produce an observable rotational spectrum. However, even a

[5] Units of wavelength or wavenumber are also used in some spectroscopic disciplines, but the commonly used unit in rotational spectroscopy is frequency (Hollas, 1998).

molecule without a permanent electric dipole moment can produce observable rotational spectral lines if it has e.g., a non-zero magnetic dipole moment or an electric quadrupole moment. The transition rates related to such higher-order poles are however very low. The requirement that a molecule needs to have a permanent electric dipole moment in order to produce an observable rotational spectrum is therefore called the electric dipole approximation (Haken and Wolf, 2006). Examples of molecules with higher-order poles observed in the ISM are O_2 and H_2, which both lack an electric dipole moment, but O_2 has a non-zero magnetic dipole moment and H_2 has a non-zero electric quadrupole moment [J. Black; priv. comm.]. In general, most homo-nuclear, di-atomic molecules and all spherical rotor molecules have no permanent electric dipole moment and therefore, no observable rotational spectrum in the electric dipole approximation. However, some spherical molecules like silane (SiH_4) can become sufficiently distorted during rotation to acquire a small electric dipole moment, resulting in observable spectral lines (Atkins et al., 2018).

In addition to entire classes of molecules that have no observable rotational spectra, most pairs of molecular energy levels are characterized by zero transition rates, even for molecules that do have an observable rotational spectrum. For all symmetric rotor molecules, and for the good quantum numbers J and M_J, it can be found that the selection rules for allowed transitions in the electric-dipole approximation are generally

$$\Delta J = \pm 1 \tag{2.22}$$

and

$$\Delta M_J = 0, \pm 1 \tag{2.23}$$

(Gordy and Cook, 1984; Griffiths, 1995; Hollas, 2004; Yamamoto, 2017; Atkins et al., 2018). There are additional selection rules for prolate and oblate symmetric rotors and asymmetric rotors, as those molecules are governed by additional quantum numbers (see e.g., Gordy and Cook, 1984; Hollas, 2004; Yamamoto, 2017; Atkins et al., 2018).

2.3 Energy Level Populations

Assuming a large total number of molecules of a particular kind within a molecular cloud source, the physical conditions of the source, most importantly H_2 density and kinetic temperature, determine the most probable distribution of molecules among the distinct rotational energy levels of the molecule under consideration. This distribution is commonly referred to as the level population. For a given set of conditions, and within a resulting population, some energy levels are much higher populated than others, meaning that some transitions are much more likely to occur than others. This directly effects the relative strength (or intensity) of spectral lines in a molecular rotational spectrum. This section first discusses the excitation and de-excitation processes that govern the level population at every instant, starting from a simple two-level system. The basic principles are then applied in a simple numeric example for the CO(1-0) transition. Then, the concepts of local thermodynamic equilibrium (LTE) and maser emission are briefly discussed. Eventually, the formulations for the two-level system are expanded to multi-level systems at LTE and non-LTE conditions.

The two-level system

In general, only two types of processes can drive transitions between the different energy levels of a molecule, i.e.,

(1) radiative processes,

(2) collisional processes.

Fig. 2.5 summarizes all radiative and collisional processes in terms of the involved coefficients. Shown is an exemplary two-level system, consisting of a lower energy level l and an upper energy level u, separated by an energy $\Delta E = h\nu$ (where $h\nu$ is photon energy).

Radiative processes

Radiative processes are those in which transition between the energy levels of a molecule are induced by interactions with radiation (photons). The corresponding absorption and emission processes can be broken down to the following three:

(1) stimulated absorption,

(2) stimulated emission,

(3) spontaneous emission.

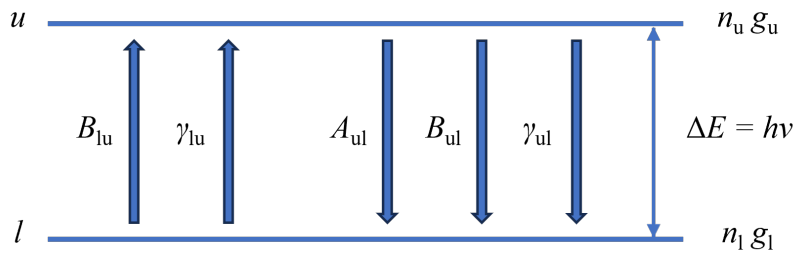

Figure 2.5: Transitions between the energy levels of a two-level system are driven by radiative processes (B_{lu}, B_{ul}, and A_{ul}) and collisional processes (γ_{lu} and γ_{ul}). ΔE is the energy separation between both levels, n_u and n_l are the numbers of molecules in the upper and lower levels, respectively, and g_u and g_l are the statistical weights of both levels.

Stimulated absorption describes the process in which a transition from a lower energy level l to an upper energy level u is driven by the absorption of a photon whose energy equals the energy difference between both levels ($\Delta E = h\nu$). Thereby, the rate of absorption is proportional to the spectral intensity I_ν of the incident radiation at the absorption frequency $\nu = \Delta E/h$. That is, the greater the radiation intensity the greater the number of photons impinging on the molecule and the greater the probability that a photon will be absorbed. The rate is also proportional to the number of molecules in the lower level n_l, because the greater the population of that level, the more likely it is that a photon will encounter a molecule in that level. The rate of stimulated absorption can therefore be written as

$$W_{lu} = B_{lu} n_l I_\nu \,, \tag{2.24}$$

where B_{lu} is the so-called Einstein coefficient of stimulated absorption (Atkins et al., 2018).

Stimulated emission is the process in which a photon is emitted during a transition from an upper energy level to a lower energy level. The rate of stimulated emission is proportional to the intensity of incident radiation at the transition frequency as well as to the number of molecules in the upper energy level n_u, i.e.,

$$W'_\mathrm{ul} = B_\mathrm{ul} n_\mathrm{u} I_\nu \,, \tag{2.25}$$

where B_ul is the Einstein coefficient of stimulated emission. Finally, in spontaneous emission, a molecule can spontaneously emit a photon by making the transition from an upper energy level to a lower energy level even in the absence of radiation. The rate of spontaneous emission is therefore only proportional to the number of molecules in the upper state and can be written as

$$W''_\mathrm{ul} = A_\mathrm{ul} n_\mathrm{u} \,, \tag{2.26}$$

where A_ul is the Einstein coefficient of spontaneous emission. When both spontaneous and stimulated emission are taken into account, the total rate of emission is

$$W_\mathrm{ul} = A_\mathrm{ul} n_\mathrm{u} + B_\mathrm{ul} n_\mathrm{u} I_\nu \tag{2.27}$$

(Atkins et al., 2018).

Assuming thermal equilibrium, the rates of emission and absorption are equal (Kirchhoff's law of thermal radiation; Yamamoto, 2017), which means that the rate of change from one energy level to another is zero. Furthermore, the spectral intensity of radiation can be expressed in terms of blackbody radiation at temperature T. Considering the above expressions for the transition rates, this can be written exemplary for the lower energy level as

$$\frac{\mathrm{d}n_\mathrm{l}}{\mathrm{d}t} = A_\mathrm{ul} n_\mathrm{u} + B_\mathrm{ul} n_\mathrm{u} B_\nu(T) - B_\mathrm{lu} n_\mathrm{l} B_\nu(T) = 0 \,, \tag{2.28}$$

which can be re-arranged to give an expression for the blackbody radiation, i.e.,

$$B_\nu(T) = \frac{A_\mathrm{ul}}{\frac{n_\mathrm{l}}{n_\mathrm{u}} B_\mathrm{lu} - B_\mathrm{ul}} \,. \tag{2.29}$$

Here, the relative population of energy levels $n_\mathrm{l}/n_\mathrm{u}$ can be expressed in terms of a Boltzmann distribution (Eq. 2.6), such that the above equation can be

expressed as

$$B_\nu(T) = \frac{A_{\rm ul}}{B_{\rm ul}} \left[\frac{g_{\rm l}}{g_{\rm u}} \frac{B_{\rm lu}}{B_{\rm ul}} \right]^{-1} \left[\exp\left(\frac{h\nu}{k_{\rm B}T} \right) - 1 \right]^{-1} . \tag{2.30}$$

Comparing this to Planck's law for the spectral intensity of a blackbody (Eq. 2.8), one can conclude that, at thermal equilibrium,

$$g_{\rm u} B_{\rm ul} = g_{\rm l} B_{\rm lu} \tag{2.31}$$

and

$$A_{\rm ul} = \frac{2h\nu^3}{c^2} B_{\rm ul} \, . \tag{2.32}$$

If follows that, if the value of only one Einstein coefficient is known, the values of the other two coefficients can be directly derived from it.

Collisional processes

Collisional processes are those in which transitions between levels are driven by collisions between a molecule with other particles in the gas phase, typically other molecules, atoms, ions, or electrons. Unlike radiative transitions, collisional transitions are generally not confined by strict selection rules (Tennyson and Faure, 2019), such that collisional transitions can also occur between distant pairs of J-levels.

The rates of collisional excitation and de-excitation between two levels u and l, i.e., $C_{\rm lu}$ and $C_{\rm ul}$, respectively, are species dependent and related to each other as

$$\frac{g_{\rm l} C_{\rm lu}}{g_{\rm u} C_{\rm ul}} = \exp\left(-\frac{\Delta E}{k_{\rm B} T_{\rm k}} \right) , \tag{2.33}$$

where $\Delta E = E_{\rm u} - E_{\rm l}$ is the energy difference between two levels and $T_{\rm k}$ is the kinetic temperature (Yamamoto, 2017). As can be seen from the above equation, the excitation rate decreases with increasing level separation ($\Delta J \propto \Delta E$) at a certain temperature, and especially at low temperatures, such that a large number of level pairs with high ΔJ can be excluded from the set of possible transitions.

Values of $C_{\rm ul}$ can be derived from tabulated values of so-called collisional rate coefficients $\gamma_{\rm ul}$ as

$$C_{\rm ul} = n({\rm X})\gamma_{\rm ul}\,, \tag{2.34}$$

where n(X) is the number volume density of the collision partner (van der Tak et al., 2007). Commonly, $\gamma_{\rm ul}$ has units of $\mathrm{cm^3\,s^{-1}}$, and tabulated values can be found in databases for different collision partners, kinetic temperatures, and level pairs. Obtained values of $C_{\rm ul}$ can then be related to $C_{\rm lu}$ via Eq. (2.33). Most basically, collisional rate coefficients are calculated from the potential energy surface of interaction between the collision partners, which is then used in a quantum scattering calculation to derive collisional cross sections $\sigma_{\rm ul}$ for transitions between levels u and l. The thermal average of the cross sections is then calculated over a range of collisional energies $E_{\rm c}$, and used as a major input to calculate the rate coefficient as

$$\gamma_{\rm ul}(T_{\rm k}) = \left[\frac{8}{\pi\mu(k_{\rm B}T_{\rm k})^3}\right]^{1/2} \int_0^\infty E_{\rm c}\sigma_{\rm ul}(E_{\rm c}) \exp\left(-\frac{E_{\rm c}}{k_{\rm B}T_{\rm k}}\right) {\rm d}E_{\rm c}\,, \tag{2.35}$$

where $\mu = m_A m_B/(m_A + m_B)$ is the reduced mass of collision partners A and B, having masses m_A and m_B (Dagdigian, 2019; Lique et al., 2020). Collisional coefficients are very difficult to measure in the laboratory and astronomical models rely almost exclusively on theoretical calculations (Faure, 2019). If collisional coefficients are not available in a database for a certain molecule it is common to use the coefficients for a similar-sized molecule. For molecular cloud environments, it is often assumed that collisional excitation and de-excitation is entirely driven by collisions between a target molecule and molecular hydrogen, because $\mathrm{H_2}$ is by far the most abundant molecule in the gas phase. However, also collisions with hydrogen atoms and electrons can be important at specific conditions (Yamamoto, 2017).

Numeric example: CO(1-0)

Considering all radiative and collisional excitation and de-excitation processes for a two-level system, affected by a radiation field with spectral intensity I_ν, the number of molecules n in the lower level changes over time according to

$$\frac{{\rm d}n_{\rm l}}{{\rm d}t} = A_{\rm ul}n_{\rm u} + B_{\rm ul}n_{\rm u}I_\nu + C_{\rm ul}n_{\rm u} - B_{\rm lu}n_{\rm l}I_\nu - C_{\rm lu}n_{\rm l}\,. \tag{2.36}$$

By using the relations between the Einstein coefficients (Eqs. 2.31 and 2.32), as well as the relation between the collisional excitation and de-excitation rates (Eq. 2.33), Eq. (2.36) can simply be written as

$$\frac{\mathrm{d}n_\mathrm{l}}{\mathrm{d}t} = \beta n_\mathrm{l} + \delta n_\mathrm{u} = 0 \,, \tag{2.37}$$

where

$$\beta = -\frac{g_\mathrm{u}}{g_\mathrm{l}} \left[A_\mathrm{ul} \frac{c^2}{2h\nu^3} I_\nu + C_\mathrm{ul} \exp\left(-\frac{h\nu}{k_\mathrm{B} T_\mathrm{k}} \right) \right] \tag{2.38}$$

and

$$\delta = A_\mathrm{ul} \frac{c^2}{2h\nu^3} I_\nu + A_\mathrm{ul} + C_\mathrm{ul} \,. \tag{2.39}$$

It is furthermore assumed that a steady state is obtained for the energy level population ($\mathrm{d}n_\mathrm{l}/\mathrm{d}t = 0$). When considering particle conservation, i.e., the requirement that

$$n_\mathrm{l} + n_\mathrm{u} = n_\mathrm{tot} \,, \tag{2.40}$$

Eqs. (2.37) and (2.40) give a system of equations that can be solved for n_l and n_u [P. Bergman; priv. comm.].

This is done in the following for the CO(1-0) two-level system, which is characterized by $g_\mathrm{u}/g_\mathrm{l} = 3$, $\nu = 115.271\,\mathrm{GHz}$, $A_\mathrm{ul} = 7.2 \times 10^{-8}\,\mathrm{s}^{-1}$, and $\gamma_\mathrm{ul} = 3.2 \times 10^{-11}\,\mathrm{cm}^3\,\mathrm{s}^{-1}$ (for collisions with $\mathrm{H_2}$ at $T_\mathrm{k} = 10\,\mathrm{K}$)[6]. The spectral intensity of radiation is assumed to be described in terms of blackbody radiation at temperature $T_\mathrm{bg} = T_\mathrm{CMB} \approx 2.7\,\mathrm{K}$, i.e., $I_\nu = B_\nu(T_\mathrm{bg})$, where T_CMB is the temperature of the cosmic microwave background (CMB). Level populations are calculated for this system for $n_\mathrm{tot} = 100\,\mathrm{cm}^{-3}$, $T_\mathrm{k} = 10\,\mathrm{K}$, and $n(\mathrm{H_2}) \in [10, 10^6]\,\mathrm{cm}^{-3}$. The value of $n(\mathrm{H_2})$ determines the collisional de-excitation rate C_ul via Eq. (2.34), and eventually, each value of $n(\mathrm{H_2})$ gives a unique level population $n_\mathrm{u}/n_\mathrm{l}$, which is related to one specific "excitation" temperature T_ex via the Boltzmann distribution (Eq. 2.6) as

$$\frac{n_\mathrm{u}}{n_\mathrm{l}} = \frac{g_u}{g_l} \exp\left(-\frac{h\nu}{k_\mathrm{B} T_\mathrm{ex}} \right) \,. \tag{2.41}$$

[6] LAMDA (Leiden Atomic and Molecular Database; https://home.strw.leidenuniv.nl/~moldata/; Schöier et al., 2005)

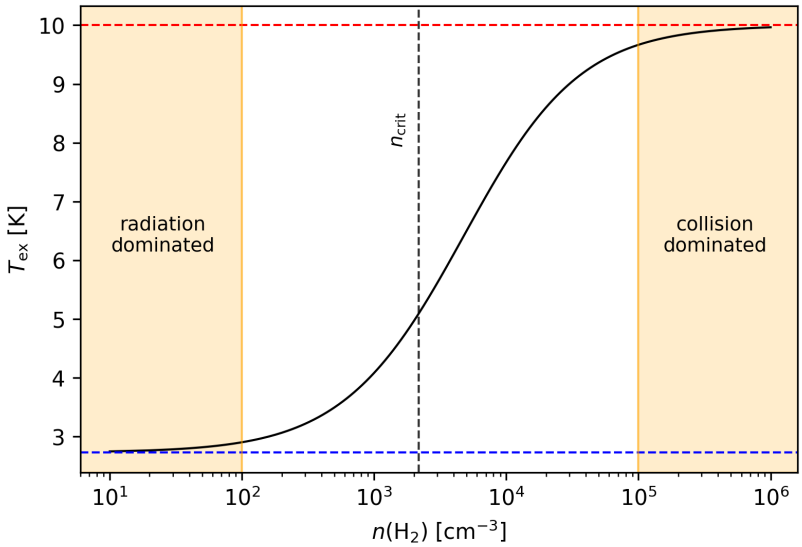

Figure 2.6: Excitation temperature $T_{\rm ex}$ corresponding to the level population $n_{\rm u}/n_{\rm l}$ of the CO(1-0) two-level system as a function of H_2 density, calculated from Eq. (2.41). The population of levels is calculated via Eqs. (2.37) and (2.40). The blue and red dashed lines respectively mark the assumed background temperature (2.7 K) and kinetic temperature (10 K). The shaded yellow areas mark the approximate densities at which the underlying population of levels is dominated by either radiation or collisions. The vertical dashed black line labeled "$n_{\rm crit}$" marks the critical density of CO(1-0), as calculated from Eq. (2.44).

Fig. 2.6 shows the change in excitation temperature as a function of H_2 density. As can be seen, $T_{\rm ex}$ approaches $T_{\rm bg}$ at low densities, but $T_{\rm k}$ at high densities, because in Eqs. (2.38) and (2.39), the terms including $A_{\rm ul}$ dominate at low densities, whereas the terms including $C_{\rm ul}$ dominate at high densities. In these two limits, the relative population of levels $n_{\rm u}$ and $n_{\rm l}$ can therefore be approximated as

$$\frac{n_{\rm u}}{n_{\rm l}} \approx \frac{g_u}{g_l} \exp\left(-\frac{h\nu}{k_{\rm B}T_{\rm bg}}\right), \tag{2.42}$$

and

$$\frac{n_{\rm u}}{n_{\rm l}} \approx \frac{g_u}{g_l} \exp\left(-\frac{h\nu}{k_{\rm B}T_{\rm k}}\right). \tag{2.43}$$

That is, in the low density limit, the level population is thermalized by the background radiation, while in the high density limit, the level population is thermalized by collisions between particles in the gas (shaded orange areas in Fig. 2.6). In intermediate areas, the level population is determined by a combination of radiation and collisions (Yamamoto, 2017).

In order to observe emission from an interstellar molecule, and to prevent cooling by radiation, the upper energy level of a specific transition must be sufficiently populated by collisions. The H_2 density necessary to fulfill that criterion can be estimated (to an order-of-magnitude) by equilibrating the collision and emission rates, i.e., $C_{\rm ul} = A_{\rm ul}$. The so-called critical H_2 density then follows from Eq. (2.34) as

$$n_{\rm crit}(H_2) = \frac{A_{\rm ul}}{\gamma_{\rm ul}} \tag{2.44}$$

(Yamamoto, 2017). The critical H_2 density for the CO(1-0) two-level system is plotted as the vertical dashed black line in Fig. 2.6. Critical densities can be directly related to the typical spatial distribution of observed emission for certain interstellar molecules. For example, the $J = 1 - 0$ transitions of HCN has a spontaneous emission coefficient of $2.4 \times 10^{-5}\,{\rm s}^{-1}$ and a collisional rate coefficient of $2.4 \times 10^{-11}\,{\rm cm}^3\,{\rm s}^{-1}$. Therefore, the critical density of HCN(1-0) is $\sim 1 \times 10^6\,{\rm cm}^{-3}$, as compared to $\sim 2 \times 10^3\,{\rm cm}^{-3}$ for CO(1-0). This means that CO(1-0) emission can arise from regions with far lower density compared to HCN(1-0) (Yamamoto, 2017).

Thermodynamic equilibrium

Assuming a system of molecules of the same kind and a large number of energy levels (i.e., a multilevel system), we can separate three possible equilibrium cases:

(1) statistical equilibrium,

(2) thermal equilibrium,

(3) thermodynamic equilibrium.

In each of these cases, no net change is observed in the total energy level population over time, i.e., there is a constant number of molecules in each

energy level i, giving $\mathrm{d}n_i/\mathrm{d}t = 0$. Then, each pair of energy levels $n_\mathrm{u}/n_\mathrm{l}$ is characterized by an excitation temperature T_ex, according to Eq. (2.41). If the excitation temperature changes from one level pair to another, the system is in statistical equilibrium. If, on the other hand, the excitation temperature is constant for all level pairs, the system is in thermal equilibrium, and the level population is well described by a Boltzmann distribution (Eq. 2.6) at that temperature. The system is furthermore in thermodynamic equilibrium, if the constant temperature is equal to the thermodynamic temperature T of the system. It is common to separate a large system into subsystems, and to allow for variations in, e.g., temperature and pressure between the subsystems, while assuming that each subsystem for itself is in so-called local thermodynamic equilibrium (LTE).

Based on the above definitions, both the low-density and high-density limits introduced in the previous section via Eqs. (2.42) and (2.43), respectively, are describing systems in thermal equilibrium. In the low-density limit, where the level population is determined by the radiation background temperature T_bg, the thermal equilibrium can be further specified as a radiative equilibrium. Systems in the high-density limit, characterized by the (H_2) kinetic temperature T_k of the system, are often assumed to be not only in thermal equilibrium but in (local) thermodynamic equilibrium. Therefore, whenever discussing "LTE conditions" in the following text, it will be assumed that $T_\mathrm{ex} = T_\mathrm{k} = T$. However, because this equality is often just an approximation, I will not make the replacements in the equations. Furthermore, whenever discussing "non-LTE conditions", I am referring to conditions in which a system is neither in thermodynamic nor in thermal equilibrium, but in statistical equilibrium, i.e., to conditions in which T_ex must be considered as a variable. It should be however noted that the possibility of having thermal equilibrium is not strictly excluded from the term "non-LTE conditions", when considering that a system can be in thermal equilibrium without being in thermodynamic equilibrium.

In astrochemical studies of molecular clouds, it is common to start from the assumption of LTE conditions. However, if LTE conditions are evidently not met for a molecular species in a certain source region, non-LTE treatments

must be considered[7]. As will be discussed in section 4.3, the population diagram method can be used as an indicator if LTE conditions are met (or are at least a good approximation). In general, the distinction between LTE and non-LTE conditions is crucial for the analysis and modeling of spectral line data, and will be discussed further at various places in the following sections and in the next chapter.

Maser Emission

Usually, the lower energy level of a pair of levels is higher populated than the upper level, giving $n_\mathrm{u} g_\mathrm{l} / n_\mathrm{l} g_\mathrm{u} < 1$. However, for certain level pairs and under specific conditions, the upper level can become higher populated than the lower level, i.e., $n_\mathrm{u} g_\mathrm{l} / n_\mathrm{l} g_\mathrm{u} > 1$, which is called population inversion. This arises from highly non-LTE conditions because, according to Eq. (2.41), an inverted population always corresponds to a negative excitation temperature. Population inversion can result in an exponential amplification of stimulated emission by the background radiation, and the corresponding phenomenon is known as microwave amplification of stimulated emission of radiation (maser). However, population inversion only occurs for certain molecules, for a limited number of level pairs, and in a limited range of physical conditions. Therefore, maser emission, though very bright, often originates from localized source regions. In the interstellar medium, maser emission has been observed for some transitions of, e.g., OH, SiO, H_2O, H_2CO, and CH_3OH (Yamamoto, 2017).

Multilevel system at LTE conditions

At LTE conditions, the energy level population of a multi-level system is simply described in terms of a Boltzmann distribution at (thermodynamic) temperature $T = T_\mathrm{ex}$, which is often assumed as the (H_2) gas kinetic temperature T_k in a molecular cloud setting. Thereby, the population n_i of the energy level with energy E_i relative to the population n_j of another energy level with $E_j < E_i$, as well as relative to the total particle population n_tot is

[7] Because excitation and de-excitation rates are highly species-dependent, it can differ from species to species if LTE conditions are met or not.

respectively determined from Eqs. (2.6) and (2.4), written slightly adjusted as

$$\frac{n_i}{n_j} = \frac{g_i}{g_j} \exp\left(-\frac{h\nu}{k_\mathrm{B} T_\mathrm{ex}}\right) \tag{2.45}$$

and

$$\frac{n_i}{n_\mathrm{tot}} = \frac{g_i}{Q_\mathrm{rot}} \exp\left(-\frac{E_i}{k_\mathrm{B} T_\mathrm{ex}}\right), \tag{2.46}$$

where Q_rot is the so-called rotational partition function, defined via Eq. (2.5) as

$$Q_\mathrm{rot} = \sum_i g_i \exp\left(-\frac{E_i}{k_\mathrm{B} T_\mathrm{ex}}\right). \tag{2.47}$$

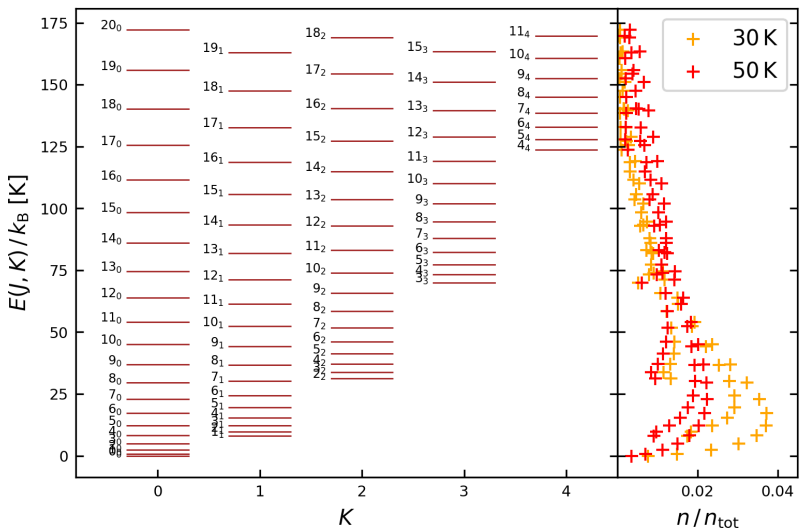

Figure 2.7: Left: rotational energy level diagram of methyl acetylene (CH_3CCH), created from tabulated values in CDMS (Cologne Database for Molecular Spectroscopy; https://cdms.astro.uni-koeln.de/; Müller et al., 2001, 2005), and showing energy levels with $E(J, K) < 175\,\mathrm{K}$. The plot shows E- and A-species combined. **Right:** equilibrium energy level population, calculated from Eq. (2.46) for two different excitation temperatures T_ex, i.e., 30 K (orange marks) and 50 K (red marks). Credit: P. Bergman for providing the *Python* code used to create this plot.

The left panel of Fig. 2.7 shows the rotational energy level diagram of methyl acetylene (CH_3CCH) for energy levels with $E(J, K) < 175\,\mathrm{K}$. Furthermore, the right panel shows the equilibrium population of energy levels, calculated from Eq. (2.46) for two different excitation temperatures T_{ex}, i.e., 30 K (orange marks) and 50 K (red marks). As can be seen, higher energy levels get populated at the expense of lower energy levels as the temperature increases. Because the population in a certain upper level is directly proportional to the emission rate of photons during transitions $u \rightarrow l$, the equilibrium temperature directly affects the set and relative strengths of observable spectral lines. In the particular case shown in Fig. 2.7 (right) for 30 K, the level population is narrow and concentrated in the lower energy level range. This leads to a relatively small set of observable spectral lines with comparatively high individual intensities. On the other hand, at 50 K, the level population is broader, leading to a larger set of spectral lines with lower individual intensities. That is, the total intensity of CH_3CCH emission gets distributed over a larger number of spectral lines with increasing temperature. However, under the assumption of thermal radiation, the total intensity is still increasing with increasing temperature.

Multilevel systems at non-LTE conditions

Assuming that the system of molecules is neither in LTE nor in thermal equilibrium, but in statistical equilibrium (SE), each pair of energy levels in the total energy level population has its own characteristic excitation temperature, according to Eq. (2.41). In this case, there is no trivial, analytical way to determine the total energy population for a (rotational) energy level system. Instead, numerical approaches have to be used that aim to solve a set of differential equations, where each equation is similar to the one stated for the two-level system (Eq. 2.36). The basic principle is the same: each equation considers the change in the population of one level over time according to the rates of radiative and collisional transitions. However, in the case of a multilevel system, there are a multitude of possible excitation and de-excitation processes, especially considering that significant collisional transitions can be caused between many pairs of levels. Most basically, assuming a total number of N energy levels and a radiation source with spectral intensity I_ν to interact with the molecules, the set of differential equations to be solved can be written

compactly as

$$\frac{\mathrm{d}n_i}{\mathrm{d}t} = \sum_{j\neq i}^{N} n_j P_{ji} - n_i \sum_{j\neq i}^{N} P_{ij} = 0\,, \tag{2.48}$$

where

$$P_{ij} = \begin{cases} A_{ij} + B_{ij} I_\nu + C_{ij} & , \text{if } i > j \\ B_{ij} I_\nu + C_{ij} & , \text{if } i < j \end{cases} \tag{2.49}$$

(Rybicki and Hummer, 1991; van der Tak et al., 2007). In the case of a multilevel system and a total number of molecules n_{tot}, particle conservation requires that

$$\sum_{i}^{N} n_i = n_{\mathrm{tot}}\,. \tag{2.50}$$

It is important to note that, in Eq. (2.49), A_{ij} and B_{ij} are zero when there is no allowed radiative transition between levels i and j. Following the discussion of collisional processes above, C_{ij} can in principle be non-zero for all i and j. It will be discussed in section 3.2 how the above set of equations is implemented into physical models describing the spectral line intensity from cold molecular cloud sources at non-LTE conditions.

2.4 Radiative Transfer

As was discussed in the previous section, the intensity of spectral lines depends on the population of molecular energy levels, which further depends on the physical conditions in a source. However, the final intensity that is emitted by a molecular cloud at a certain frequency does not only depend on the physical conditions in the cloud, but also on interactions of the cloud with the surrounding radiation field, and, most importantly, the change of intensity as radiation is traveling through the cloud.

Basic equations

The intensity from a molecular cloud source is conceptually defined via the equations of radiative transfer. Then, it is assumed that the cloud interacts with some background radiation field, having spectral intensity $I_\nu = B_\nu(T_{\mathrm{bg}})$. Upon entering the molecular cloud, the background radiation will start to

interact with molecules inside the cloud by means of absorption and stimulated emission, causing transitions between energy levels and the absorption and emission of photons. In addition, the molecules release photons by means of spontaneous emission. Furthermore, collisions between molecules and other particles in the cloud lead to further transitions between energy levels. Thereby, every emitted photon in the cloud can interact with molecules in between the position of release and the edge of the cloud, leading to a non-trivial chain of absorption and emission processes. The effectiveness of these processes depends on the composition and physical conditions (largely density and temperature) of the cloud, but can be generally quantified in terms of the absorbance α_ν (m^{-1}) and the emissivity ϵ_ν ($\mathrm{W\,Hz^{-1}\,sr^{-1}\,m^{-3}}$), which are both position-dependent. With these two parameters, any change in spectral intensity $\mathrm{d}I_\nu$ of the radiation due to absorption and emission along an infinitesimal propagation $\mathrm{d}x$ in the cloud can be written as the following radiative transfer equation:

$$\mathrm{d}I_\nu(x) = -\alpha_\nu(x) I_\nu \,\mathrm{d}x + \epsilon_\nu(x)\,\mathrm{d}x\,. \tag{2.51}$$

The spectral intensity I_ν emerging from the cloud at $x = L$ can be obtained by integration of Eq. (2.51) over all positions x along the path through the cloud, i.e.,

$$\int_0^L \mathrm{d}I_\nu(x) = I_\nu(L) - I_\nu(0) = \int_0^L \Big[-\alpha_\nu(x) I_\nu + \epsilon_\nu(x)\Big]\,\mathrm{d}x\,, \tag{2.52}$$

from which it follows that

$$I_\nu(L) = I_\nu(0) + \int_0^L \Big[-\alpha_\nu(x) I_\nu + \epsilon_\nu(x)\Big]\,\mathrm{d}x\,. \tag{2.53}$$

This means that the spectral intensity at $x = L$ is given by the initial spectral intensity of the background plus an integral factor taking into account the absorption of incoming radiation by molecules in the cloud as well as the intrinsic emission of the molecules.

It is common to rewrite Eq. (2.51) in terms of the so-called source function S_ν with dimensions of spectral intensity ($\mathrm{W\,Hz^{-1}\,sr^{-1}\,m^{-2}}$) as well as the

(differential) optical depth $\mathrm{d}\tau_\nu$ (dimensionless), respectively defined as

$$S_\nu(x) = \frac{\epsilon_\nu(x)}{\alpha_\nu(x)} \tag{2.54}$$

and

$$\mathrm{d}\tau_\nu(x) = \alpha_\nu(x)\,\mathrm{d}x\,. \tag{2.55}$$

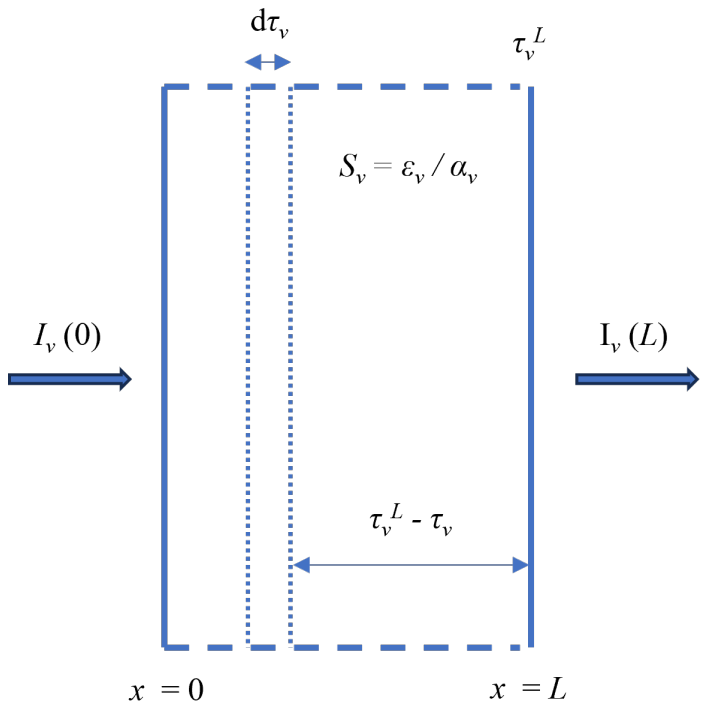

Figure 2.8: When background radiation with spectral intensity $I_\nu(0) = B_\nu(T_{\mathrm{bg}})$ enters a molecular cloud at $x = 0$, it starts to interact with molecules via absorption and stimulated emission. The source function S_ν considers the ratio of emissivity ϵ_ν and absorbance α_ν at a certain position. Based on the optical depth τ_ν of the medium, Eq. (2.66) calculates the final spectral intensity $I_\nu(L)$ coming from the cloud at $x = L$, taking into account all possible processes of emission, absorption, and re-absorption.

Assuming a physically and chemically homogeneous medium inside the cloud, both the emissivity and the absorbance as well as the source function and differential optical depth do not longer depend on position, but are constant everywhere, i.e.,

$$S_\nu = \frac{\epsilon_\nu}{\alpha_\nu} \tag{2.56}$$

and

$$\mathrm{d}\tau_\nu = \alpha_\nu \, \mathrm{d}x \,. \tag{2.57}$$

Dividing now both sides of Eq. (2.51) by α_ν while inserting Eqs. (2.56) and (2.57) yields

$$\mathrm{d}I_\nu = -I_\nu \, \mathrm{d}\tau_\nu + S_\nu \, \mathrm{d}\tau_\nu \,. \tag{2.58}$$

The integration to derive the final spectral intensity is therefore no longer over position but over optical depth τ_ν, i.e.,

$$\int_0^{\tau_\nu^L} \mathrm{d}I_\nu, \tag{2.59}$$

where τ_ν^L is the optical depth at $x = L$, defined as

$$\tau_\nu^L = \alpha_\nu L \,, \tag{2.60}$$

while, in general, the optical depth at any depth x into the cloud is defined as

$$\tau_\nu = \alpha_\nu x \,, \tag{2.61}$$

such that the initial optical depth at $x = 0$ is zero (Yamamoto, 2017).

The integration in Eq. (2.59) is approached by first moving $I_\nu \, \mathrm{d}\tau_\nu$ in Eq. (2.58) to the left while multiplying by the integration factor $\exp(\tau_\nu)$, i.e.,

$$\begin{aligned}
\mathrm{e}^{\tau_\nu} \Big[\mathrm{d}I_\nu + I_\nu \, \mathrm{d}\tau_\nu \Big] &= \mathrm{e}^{\tau_\nu} S_\nu \, \mathrm{d}\tau_\nu & (2.62)\\
\mathrm{e}^{\tau_\nu} \, \mathrm{d}I_\nu + \mathrm{e}^{\tau_\nu} I_\nu \, \mathrm{d}\tau_\nu &= \mathrm{e}^{\tau_\nu} S_\nu \, \mathrm{d}\tau_\nu & (2.63)\\
\mathrm{d}\Big[\mathrm{e}^{\tau_\nu} I_\nu \Big] &= \mathrm{e}^{\tau_\nu} S_\nu \, \mathrm{d}\tau_\nu & (2.64)
\end{aligned}$$

Integrating the last equation from the starting point $\tau_\nu = 0$ at $x = 0$ with

initial value I_ν^0 gives

$$\int_0^{\tau_\nu^L} \mathrm{d}\left[\mathrm{e}^{\tau_\nu} I_\nu\right] = \mathrm{e}^{\tau_\nu^L} I_\nu(L) - I_\nu(0) = \int_0^{\tau_\nu^L} \mathrm{e}^{\tau_\nu} S_\nu \, \mathrm{d}\tau_\nu \,, \tag{2.65}$$

which can be rearranged to give

$$I_\nu(L) = I_\nu(0)\, \mathrm{e}^{-\tau_\nu^L} + \int_0^{\tau_\nu^L} \mathrm{e}^{-[\tau_\nu^L - \tau_\nu]} S_\nu \, \mathrm{d}\tau_\nu \,. \tag{2.66}$$

That is, each slab $\mathrm{d}\tau_\nu$ contributes $S_\nu \, \mathrm{d}\tau_\nu \exp\left(-\left[\tau_\nu^L - \tau_\nu\right]\right)$ to the emitted radiation, where $S_\nu \mathrm{d}\tau_\nu$ corresponds to the intrinsic emission of molecules in the cloud and $\exp\left(-\left[\tau_\nu^L - \tau_\nu\right]\right)$ corresponds to the attenuation of this radiation by molecules in between the emitting slab and the edge of the cloud at $x = L$ (see Fig. 2.8) (Draine, 2011). Assuming that the source function is constant under the integration, Eq. (2.66) simplifies to

$$I_\nu(L) = I_\nu(0)\, \mathrm{e}^{-\tau_\nu^L} + S_\nu \left[1 - \mathrm{e}^{-\tau_\nu^L}\right] \tag{2.67}$$

$$= B_\nu(T_\mathrm{bg})\, \mathrm{e}^{-\tau_\nu^L} + S_\nu \left[1 - \mathrm{e}^{-\tau_\nu^L}\right] \tag{2.68}$$

where the last expression describes the case in which $I_\nu(0)$ can be approximated as the spectral intensity of a blackbody at background temperature T_bg (Eq. 2.8).

Spectral line radiation

The above equations of radiative transfer are valid for both continuum radiation over a large bandwidth as well as spectral line radiation. Spectral lines are generally associated with a drastic change of emission and absorption properties over very small frequency intervals. In the following, the focus will be on spectral line radiation, and in particular, spectral line emission.

If the focus is on the description of spectral line radiation, the absorbance and the emissivity are defined as

$$\alpha_\nu = \frac{h\nu}{4\pi}(n_\mathrm{l} B_\mathrm{lu} - n_\mathrm{u} B_\mathrm{ul})\phi(\nu) \tag{2.69}$$

and

$$\epsilon_\nu = \frac{h\nu}{4\pi} n_\mathrm{u} A_\mathrm{ul} \phi(\nu)\,, \tag{2.70}$$

respectively (van der Tak et al., 2007; Yamamoto, 2017). n_u and n_l are the populations of an arbitrary pair of upper and lower energy levels at a certain position x on the path through the cloud. Furthermore, $\phi(\nu)$ is the spectral line profile, satisfying the normalization relation

$$\int \phi(\nu)\mathrm{d}\nu = 1 \tag{2.71}$$

(Yamamoto, 2017). Here, it is assumed that the line profiles for stimulated absorption, stimulated emission, and spontaneous emission are the same. In the ISM, spectral lines are predominantly affected by Doppler broadening (van der Tak et al., 2007, see section 2.5), such that they can be well approximated as Gaussians. With the above definitions of absorbance and emissivity, as well as the relations between the Einstein coefficients (Eqs. 2.31 and 2.32), the source function (Eq. 2.56) becomes

$$S_\nu = \frac{\epsilon_\nu}{\alpha_\nu} = \frac{n_\mathrm{u} A_\mathrm{ul}}{n_\mathrm{l} B_\mathrm{lu} - n_\mathrm{u} B_\mathrm{ul}} = \frac{2h\nu^3}{c^2} \left[\frac{n_\mathrm{l}}{n_\mathrm{u}} \frac{g_\mathrm{u}}{g_\mathrm{l}} - 1 \right]^{-1}, \tag{2.72}$$

which is independent of the spectral line profile. Assuming statistical equilibrium (SE), the energy levels are populated according to Eq. (2.41), i.e.,

$$\frac{n_\mathrm{u}}{n_\mathrm{l}} = \frac{g_u}{g_l} \exp\left(-\frac{h\nu}{k_\mathrm{B} T_\mathrm{ex}} \right).$$

For the SE case, the source function can therefore be written as

$$S_\nu = \frac{2h\nu^3}{c^2} \left[\exp\left(\frac{h\nu}{k_\mathrm{B} T_\mathrm{ex}} \right) - 1 \right]^{-1}. \tag{2.73}$$

For a system in thermal equilibrium, it is furthermore true that

$$S_\nu = B_\nu(T_\mathrm{ex}) \tag{2.74}$$

(see Eq. 2.8), which means that the source function is equal to the spectral

intensity of a blackbody and can be described by a constant temperature $T_{\rm ex}$ at all frequencies (Yamamoto, 2017). However, in SE, the value of $T_{\rm ex}$ differs with frequency, i.e., from one transition (or spectral line) to another (see section 2.3).

Using the relations between the Einstein coefficients, it can be furthermore found that the absorption coefficient can also be expressed as

$$\alpha_\nu = \frac{c^2}{8\pi\nu^2}\frac{g_{\rm u}}{g_{\rm l}} n_{\rm l} A_{\rm ul}\left(1 - \frac{g_{\rm l}}{g_{\rm u}}\frac{n_{\rm u}}{n_{\rm l}}\right)\phi(\nu)\,, \tag{2.75}$$

and at SE, this can be written as

$$\alpha_\nu = \frac{c^2 n_{\rm u} A_{\rm ul}}{8\pi\nu^2}\left[\exp\left(\frac{h\nu}{k_{\rm B}T_{\rm ex}}\right) - 1\right]\phi(\nu)\,. \tag{2.76}$$

Based on the general definition of optical depth (Eq. 2.61), the optical depth of a spectral line in the frequency interval defined by the line profile is obtained by integration of the absorbance over the path length through the source, i.e.,

$$\begin{aligned}
\tau_\nu &= \int_0^L \alpha_\nu(x)\,{\rm d}x && (2.77)\\
&= \frac{c^2 A_{\rm ul}}{8\pi\nu^2}\left[\exp\left(\frac{h\nu}{k_{\rm B}T_{\rm ex}}\right) - 1\right]\phi(\nu)\int_0^L n_{\rm u}(x)\,{\rm d}x && (2.78)\\
&= \frac{c^2 N_{\rm u} A_{\rm ul}}{8\pi\nu^2}\left[\exp\left(\frac{h\nu}{k_{\rm B}T_{\rm ex}}\right) - 1\right]\phi(\nu)\,. && (2.79)
\end{aligned}$$

Here, $N_{\rm u}$ is introduced as the upper level column density, which will be important again in section 4.1. Furthermore, with the normalization relation in Eq. (2.71), integration over the line profile yields the total optical depth associated with the spectral line, i.e.,

$$\int \tau_\nu\,{\rm d}\nu = \frac{c^2 N_{\rm u} A_{\rm ul}}{8\pi\nu^2}\left[\exp\left(\frac{h\nu}{k_{\rm B}T_{\rm ex}}\right) - 1\right]. \tag{2.80}$$

2.5 Spectral Line Shape

Spectral lines are not infinitely narrow "lines" at one single frequency, but have a width that spreads over a range of frequencies. This width directly depends on the ambient physical conditions, most importantly pressure and temperature, but is also affected by fundamental quantum effects. In the following, the effects of lifetime broadening, pressure broadening, and thermal Doppler broadening, are introduced and discussed for the CO(1-0) line. Note that in this section, the symbols "v" and "f" are respectively used for velocity and frequency, to not confuse v and ν. A major part of the information and equations in this section were taken from an online lecture, which does not exist anymore. Similar content is found in https://cefrc.princeton.edu/sites/g/files/toruqf1071/files/2018_hanson_plecture6.pdf (Princeton University; retrieval date: 2026-08-13) and https://superlidar.colorado.edu/Classes/Lidar2006/Lecture8.pdf (University of Colorado Boulder; retrieval date: 2026-08-13).

Lifetime broadening and natural linewidth

A gas phase molecule that is in a certain state at a certain instant will not remain in that state indefinitely. It will rather change its state by interactions with radiation or other particles (see section 2.3). The lifetime τ and the energy E of a state are related to each other by the uncertainty principle as

$$\Delta\tau\Delta E \approx \hbar\,. \tag{2.81}$$

That is, the energy is uncertain (spread out) as $\Delta E \approx \hbar/\Delta\tau$, from which it follows that the associated frequency f is also spread out over a range of frequencies as

$$\Delta f = \frac{\Delta E}{h} \approx \frac{1}{2\pi\Delta\tau}\,. \tag{2.82}$$

If the lifetime is very well determined the spread in frequency is at its maximum and the spread in lifetime can be replaced by the value τ, i.e.,

$$\Delta f \approx \frac{1}{2\pi\tau}\,. \tag{2.83}$$

As can be seen, the spread in frequency increases with decreasing lifetime. Spectral lines that result from transitions involving the considered state will

be accordingly spread out in frequency. This phenomenon is known as the lifetime broadening of spectral lines (Gordy and Cook, 1984; Atkins et al., 2018).

If it is assumed that a molecule is completely isolated from radiation or other particles it can only change from an excited state u by means of spontaneous emission, characterized by the corresponding Einstein coefficient A_{ul} (see last section). The lifetime of the molecule in state u is then given as

$$\tau_{\mathrm{u}} = \frac{1}{A_{\mathrm{ul}}}\,, \tag{2.84}$$

and the resulting spread in frequency of a spectral line is called its natural linewidth (Gordy and Cook, 1984; Atkins et al., 2018).

Considering only the effect of lifetime broadening, the frequency profile of a spectral line $\phi(f)$ is Lorentzian with

$$\phi(f) = \frac{z/4\pi^2}{(f - f_0) + (z/4\pi)^2}\,, \tag{2.85}$$

where

$$z = \sum_{j<i} A_{ij}\,, \tag{2.86}$$

and f_0 is the rest frequency of a given transition. A_{ij} is the Einstein coefficient of spontaneous emission for transitions between levels i and j. Furthermore, in the presence of radiation, the rates of stimulated emission have to be added as well. The blue line in Fig. 2.9 shows the natural linewidth of the CO(1-0) line with $f_0 = 115.271\,\mathrm{GHz}$ and $z = A_{\mathrm{ul}} = 7.2 \times 10^{-8}\,\mathrm{s}^{-1}$, calculated from Eq. (2.85).

Pressure broadening

Collisions between molecules in the gas phase are an efficient way to induce changes in molecular states (see section 2.3). Considering a collisional de-excitation rate C_{ul} from level u to level l, the collisional lifetime of a state can be defined as

$$\tau_{\mathrm{col}} = \frac{1}{C_{\mathrm{ul}}}\,. \tag{2.87}$$

The associated contribution to the width of a spectral line is referred to as collisional broadening or, because the collision frequency is proportional to pressure, as pressure broadening (Gordy and Cook, 1984; Atkins et al., 2018). Taking into account both the natural linewidth and pressure broadening, the frequency profile $\phi(f)$ is still described by Eq. (2.85), but now

$$z = \sum_{j<i} (A_{ij} + 2C_{ij}) \tag{2.88}$$

(Gordy and Cook, 1984).

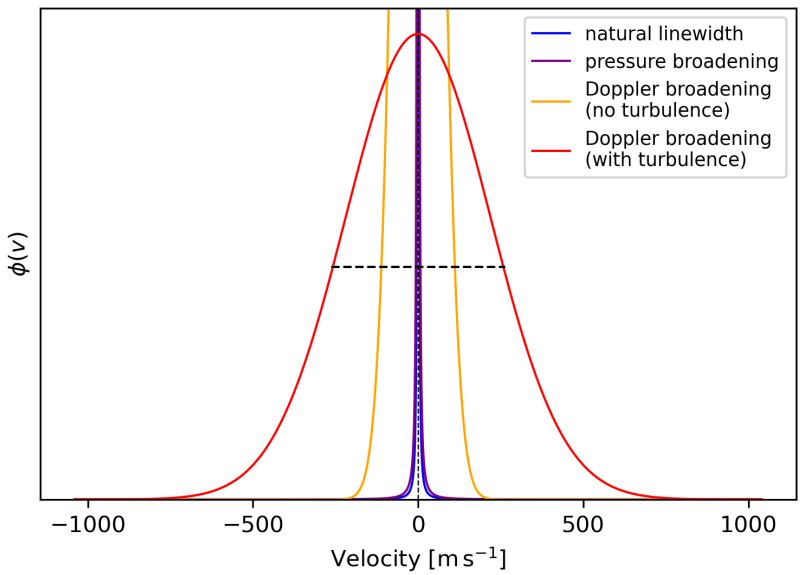

Figure 2.9: Effects of lifetime broadening (Eqs. 2.85 and 2.86; blue line), pressure broadening (Eqs. 2.85 and 2.88; purple line), and thermal Doppler broadening (Eqs. 2.92, 2.93, and 2.94; yellow and red lines) on the shape of the CO(1-0) line. The frequency axis was converted to velocity via $v = c(f_0 - f)/f_0$. The vertical dashed black line marks the CO(1-0) rest frequency f_0 at $v = 0$, and the horizontal dashed black line marks the (turbulent) Doppler line width.

The purple line in Fig. 2.9 shows the profile of a pressure broadened CO(1-0) line, calculated from Eqs. (2.85) and (2.88). For collision partner H_2, the

CO(1-0) collisional rate coefficient is $\gamma_{\rm ul} = 3.3 \times 10^{-11}\,{\rm cm^3\,s^{-1}}$ at $T_{\rm k} = 10\,{\rm K}$[8]. The collisional de-excitation rate is then given as $C_{\rm ul} = n({\rm H_2})\gamma_{\rm ul}$, where $n({\rm H_2})$ is the volume density of H_2. A value of $n({\rm H_2}) = 10^{12}\,{\rm cm^{-3}}$ has been chosen for the example in Fig. 2.9. At lower values, the pressure broadened line profile coincides with the natural line profile[9]. It follows that the process of pressure broadening is negligible for spectral lines produced by molecules in molecular clouds where H_2 densities are typically in the range of $10^4 - 10^7\,{\rm cm^{-3}}$ (van Dishoeck et al., 2013).

Thermal Doppler broadening

The molecules in a gas mixture move at different velocities v and in different directions relative to an observer at rest. In thermal equilibrium, the velocities are distributed according to a Maxwell-Boltzmann distribution, that depends on the gas temperature. Along the line of sight of the observer, some molecules will approach while others will recede. According to the Doppler effect, the frequency of emitted radiation from the molecules will be different depending on weather they approach or recede. For molecules moving perpendicular to the line of sight, the radiation frequency will be unaffected (Gordy and Cook, 1984; Atkins et al., 2018). Assuming a transition rest frequency f_0 and non-relativistic velocities $v \ll c$, the frequency of radiation emitted by approaching and receding molecules is given by

$$f_{\rm app} = (1 + \frac{v}{c}) f_0 \tag{2.89}$$

and

$$f_{\rm rec} = (1 - \frac{v}{c}) f_0\,, \tag{2.90}$$

respectively. That is, the observed frequency will be higher than the rest frequency for approaching molecules, but lower than the rest frequency for receding molecules. The corresponding shift between observed frequency and

[8] LAMDA (Leiden Atomic and Molecular Database; https://home.strw.leidenuniv.nl/~moldata/; Schöier et al., 2005)

[9] Considering the collisional rate coefficient for higher temperatures does not change this, as the value of $\gamma_{\rm ul}$ for CO(1-0) increases only slightly to $3.8 \times 10^{-11}\,{\rm cm^3\,s^{-1}}$ at the maximum available temperature of 3 000 K.

rest frequency (due to the Doppler effect) is therefore

$$\Delta f_{\mathrm{D}} = f_{\mathrm{obs}} - f_0 = \pm \frac{v}{c} f_0 \tag{2.91}$$

(Atkins et al., 2018). Considering only one velocity component, say v_x, the molecular velocities are Gaussian distributed, from which it follows that the observed frequency shifts will also be Gaussian distributed[10]. Furthermore, the width of the velocity distribution depends on temperature, such that the frequency distribution depends on temperature as well. It is generally increasing with increasing temperature. The broadening of spectral lines due to the described shift of observed frequencies is therefore called (thermal) Doppler broadening (Gordy and Cook, 1984; Atkins et al., 2018).

The frequency profile $\phi(f)$ of a Doppler broadened spectral line is described by the Gaussian profile

$$\phi(f) = \frac{\exp(-\Delta f_{\mathrm{D}}^2 / \delta f_{\mathrm{D}}^2)}{\delta f_{\mathrm{D}} \sqrt{\pi}} \,, \tag{2.92}$$

where

$$\delta f_{\mathrm{D}} = \frac{f_0}{c} \sqrt{\frac{2 k_{\mathrm{B}} T}{m}} \tag{2.93}$$

is the (Doppler) linewidth at half maximum (Gordy and Cook, 1984; Atkins et al., 2018). Turbulent gas motions can be considered as well by adding a term for the root-mean square of the turbulent gas velocity v_{turb} to the Doppler linewidth, which then becomes

$$\delta f_{\mathrm{D}} = \frac{f_0}{c} \sqrt{\frac{2 k_{\mathrm{B}} T}{m} + v_{\mathrm{turb}}^2} \,. \tag{2.94}$$

The yellow line in Fig. 2.9 shows the shape of a Doppler broadened CO(1-0) spectral line, calculated from Eqs. (2.92) and (2.93), i.e., neglecting any turbulence. The assumed temperature is 10 K, which is typical for a cold molecular cloud environment. The red line further shows the line profile considering turbulence via Eq. (2.94) with $v_{\mathrm{turb}} = 0.3\,\mathrm{km\,s^{-1}}$, which is also typical for a cold molecular cloud. The horizontal dashed black line shows the (turbulent)

[10] The consideration of only one velocity component is sufficient for the characterization of the line-of-sight molecular velocities.

Doppler line width. As can be seen, at typical molecular cloud conditions, the effect of Doppler broadening clearly dominates over the effects of lifetime broadening and pressure broadening, while the effect of turbulence further dominates over the effect of temperature (and molecule mass).

The frequency profile of a spectral line considering the combined effect of lifetime broadening, pressure broadening, and Doppler broadening is described by a Voigt profile (convolution of a Lorentzian and a Gaussian profile), which has no simple analytical form. Most basically, a Lorentzian profile falls off slower than a Gaussian profile such that the core of a spectral line is best described by a Gaussian while the wings are better described by a Lorentzian. However, as indicated above, spectral lines emitted by molecules in molecular cloud environments are usually well fitted by simple Gaussians, as their shape is largely dominated by Doppler broadening.

2.6 Antenna Theory

Molecules in cold molecular cloud environments are emitting radiation as spectral lines over narrow frequency intervals. In order to analyze the abundances of molecules in a certain source region, the emitted spectral intensity I_ν from the source must be captured with a radio telescope in a certain bandwidth. The basics of single-dish observations are discussed in this section, starting with some background to the measurement and calibration of radio signals. It follows a discussion of the concepts of source size and beam size as well as the demands on surface and pointing accuracy.

Rayleigh-Jeans limit, system temperature, and noise

Radio astronomers are often operating in the limit $h\nu \ll k_\mathrm{B}T$, such that the received intensity I_ν from a source can be well described by the Rayleigh-Jeans approximation (Eq. 2.10; Condon and Ransom, 2016; Yamamoto, 2017). By using this relation, the spectral intensity of a source at a certain frequency ν can also be expressed in terms of the corresponding source temperature T_S as

$$T_\mathrm{S}(\nu) = \frac{I_\nu c^2}{2k_\mathrm{B}\nu^2} \,. \tag{2.95}$$

However, when measured with a radio antenna, the source signal is superimposed on signals from the cosmic microwave background (T_{CMB}), other radio background sources in the sky (T_{sky}), the atmosphere (T_{atm}), the ground beneath the antenna (T_{ground}), and the receiver system (T_{RX})[11]. The overlay of the measured signals is what defines the total system temperature, i.e.,

$$T_{\mathrm{sys}} = T_{\mathrm{S}} + T_{\mathrm{CMB}} + T_{\mathrm{sky}} + T_{\mathrm{atm}}\left[1 - \mathrm{e}^{-\tau_{\nu}^{\mathrm{atm}}}\right] + T_{\mathrm{ground}} + T_{\mathrm{RX}} + \dots\,, \quad (2.96)$$

where $\tau_{\nu}^{\mathrm{atm}}$ is the optical depth of the atmosphere at frequency ν (Condon and Ransom, 2016). Of course, the system temperature and all contributions to it are frequency-dependent, but for simplicity, this dependence is neglected in the notation above. At millimeter and submillimeter wavelengths, the noise contributions from the atmosphere and the receiver system are usually the largest. The system temperature further defines the RMS (root mean square) noise temperature σ_T, which is approximately given by the ideal radiometer equation as

$$\sigma_T \approx \frac{T_{\mathrm{sys}}}{\sqrt{\Delta\nu t_{\mathrm{int}}}}\,, \quad (2.97)$$

where t_{int} is the integration time, and $\Delta\nu$ is the bandwidth (Condon and Ransom, 2016). As can be seen, the noise temperature can be reduced by longer integration times. In addition, different calibration and switching methods are used to minimize the effects from distracting signals, and to filter out the desired source signal.

Calibration and switching techniques

When targeting an astronomical source with a telescope inside the Earth's atmosphere, the source signal gets attenuated by the optical depth of the atmosphere at the observed frequency. However, the optical depth is not constant, but changes over time due to short-term variations in atmospheric conditions, including temperature, pressure, and humidity. An integral part of all observation runs is therefore the repeated determination of those parameters, followed by the calibration of the receiver system to the determined values. In radio astronomy, a common calibration method is the so-called chopper-wheel method (Jewell, 2002; Wilson, 2013).

[11] Additional noise arises from artificial radio frequency interference (RFI) from e.g., television, radio, and mobile network.

Effects from the noise sources in Eq. (2.96) are minimized by using different switching techniques, i.e., position-switching, beam-switching, and frequency-switching. The contribution from the receiver system is further minimized by cooling it to cryogenic temperatures. In position- and beam-switching, the signal from a reference position at a certain offset from the source is measured in repeating intervals during an observation run, and then subtracted from the source signal. Thereby, the offset to the source position must be large enough such that it is completely free of any target radiation. In position-switching, the main reflector of the telescope is moved to switch between both positions, while in beam-switching, only the sub-reflector is moved. Therefore, the offset can be arbitrary in position-switching, but is limited in beam-switching due to mechanical reasons. The switching is faster and more stable with beam-switching, but the maximum offset must be considered when observing extended sources. It is common to observe the same amount of time on-source and off-source. In frequency switching, the center frequency is switched to an offset frequency for half of the observing time, and the spectra observed at the offset frequency are then subtracted from those observed at the center frequency. The spectra at the offset frequency still contain the signal and can be integrated together with the spectra at the center frequency after some processing. The required integration time to reach a certain noise level is therefore reduced by about 50 %. However, this method is most suitable for observations of a limited number of known target spectral lines in frequency bands otherwise free of signals, because there is otherwise the risk of loosing signal during subtraction [E. Wirström, P. Bergman, C. Horellou; priv. comm.].

The underlying principle in the three switching methods is essentially the same. That is, approximately half of the observing time is used to measure the on-source or on-frequency intensity I_ν^{on} in a certain bandwidth, while the remaining observation time is spend to measure the off-source or off-frequency intensity I_ν^{off}. The intensity difference

$$\Delta I_\nu = I_\nu^{\mathrm{on}} - I_\nu^{\mathrm{off}} \tag{2.98}$$

is then obtained and converted to the corresponding radiation temperature

T_R, which is given as

$$T_\mathrm{R}(\nu) = \frac{\Delta I_\nu c^2}{2k_\mathrm{B}\nu^2} \tag{2.99}$$

in the Rayleigh-Jeans limit (Wilson, 2013; Mangum and Shirley, 2015; Yamamoto, 2017). This temperature is now close to the source temperature as would be measured outside the Earth's atmosphere.

Beam size, source size, and beam filling

Both the telescope beam and the observed source have an extension on the sky, and if the beam is larger than the source, the measured intensity will be only a fraction of the true source intensity. This effect is called beam dilution. If the source size is known, the fraction of the source that is filling the beam can be quantified via the so-called beam-filling factor, making it possible to correct for beam dilution.

The beam size of a single-dish antenna is derived from the power pattern of a parabolic reflector, which is given by the square of the electric field pattern. Assuming a cosine-tapered illumination by incoming plane waves from a far distant source, the electric field pattern of a parabolic reflector can be written as

$$f(l) = \frac{\cos \pi l}{1 - 4l^2}\,, \tag{2.100}$$

where l is a measure of the reflection angle at different points of the reflector (Condon and Ransom, 2016). Fig. 2.10 shows a plot of the (normalized) field pattern $f_\mathrm{n}(l)$ (left), and the corresponding normalized power pattern $P_\mathrm{n}(l) = f_\mathrm{n}^2(l)$ (right), which has Gaussian shape. The beam size θ (in radians) is commonly expressed in terms of the full width at half maximum of that Gaussian, which is commonly called the half-power beam width (HPBW) in this context. It can generally be approximated as

$$\theta_\mathrm{HPBW}(\lambda) \approx 1.2\frac{\lambda}{D}\,, \tag{2.101}$$

where λ is the wavelength of radiation and D is the aperture diameter (Condon and Ransom, 2016). The half-power beam width is indicated by the red dashed line in Fig. 2.10 (right).

A source on the sky covers a solid angle Ω_S, and the spatial extension of the source is embedded in the basic equation of the source temperature T_S (Eq. 2.95), which has dimensions of $\mathrm{K\,sr^{-1}}$. The source temperature (or brightness) distribution can therefore be written as a position-dependent parameter $T_\mathrm{S}(\nu, \mathbf{r})$, where $\mathbf{r}$ is a position-vector in a coordinate system with $(0, 0)$ at the source center.

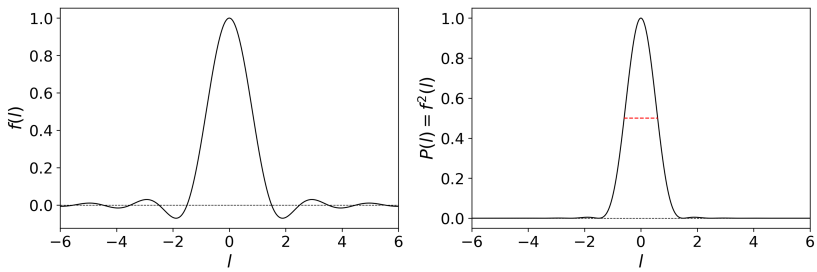

Figure 2.10: Left: normalized field pattern $f(l)$ of a parabolic reflector, calculated from Eq. (2.100). **Right:** normalized power pattern $P(l) = f^2(l)$ of a parabolic reflector. The dashed red line marks the HPBW of the Gaussian beam.

When a telescope is pointed at a source with a certain temperature distribution, the measured total power per unit bandwidth is

$$\mathcal{P}(\nu) = k_\mathrm{B} T_\mathrm{A} = \frac{1}{2} A_\mathrm{e} \int T_\mathrm{S}(\nu, \mathbf{r}) P_\mathrm{n}(\nu, \mathbf{r}) \, \mathrm{d}\mathbf{r} \,, \tag{2.102}$$

where A_e is the effective collecting area of the telescope and $P_\mathrm{n}(\nu, \mathbf{r})$ is the normalized power pattern of the telescope beam (Fig. 2.10, right), here expressed in terms of $\mathbf{r}$ in the same coordinate system as the source. Furthermore, T_A is the power-equivalent antenna temperature, defined via the so-called Nyquist theorem ($\mathcal{P} = k_\mathrm{B} T$). Considering that a beam with a normalized power pattern has beam solid angle

$$\Omega_\mathrm{B}(\nu) = \int P_\mathrm{n}(\nu, \mathbf{r}) \, \mathrm{d}\mathbf{r} \,, \tag{2.103}$$

and by using the antenna theorem ($A_\mathrm{e} \Omega_\mathrm{B} = \lambda^2$; A_e: effective collecting area of the antenna) with the Rayleigh-Jeans approximation (Eq. 2.10), it follows

from Eq. (2.102) that the antenna temperature can be written as

$$T_{\mathrm{A}}(\nu) = \frac{\int_{\mathrm{S}} T_{\mathrm{S}}(\nu, \mathbf{r}) P_{\mathrm{n}}(\nu, \mathbf{r}) \, \mathrm{d}\mathbf{r}}{\int P_{\mathrm{n}}(\nu, \mathbf{r}) \, \mathrm{d}\mathbf{r}} \,, \tag{2.104}$$

That is, the antenna temperature is the normalized beam-weighted average of the source (or sky) temperature distribution (Wilson, 2013).

An important definition is the main beam solid angle Ω_{mb}, defined as the region of the normalized power pattern $P_{\mathrm{n}}(\nu, \mathbf{r})$ that contains the principal response, i.e., the response out to the first zero in Fig. 2.10 (right). Any responses outside this region are called sidelobes, or very far from it, stray radiation. The main beam solid angle is related to the total beam solid angle as

$$\eta_{\mathrm{mb}}(\nu) = \frac{\Omega_{\mathrm{mb}}(\nu)}{\Omega_{\mathrm{B}}(\nu)} \,, \tag{2.105}$$

where η_{mb} is called the main beam efficiency. With the definition of main beam efficiency, the measured antenna temperature is usually converted to the so-called main beam temperature

$$T_{\mathrm{mb}}(\nu) = \frac{T_{\mathrm{A}}(\nu)}{\eta_{\mathrm{mb}}(\nu)} \,, \tag{2.106}$$

which then provides a better estimate of the intrinsic source temperature (Condon and Ransom, 2016). Typical values of η_{mb} are $0.5-0.9$, depending on the telescope and the frequency. The main beam solid angle of a circular antenna is related to the Gaussian HPBW as

$$\Omega_{\mathrm{mb}}(\nu) = \frac{\pi}{4 \ln(2)} \, \theta_{\mathrm{HPBW}}(\nu)^2 \approx 1.133 \, \theta_{\mathrm{HPBW}}(\nu)^2 \tag{2.107}$$

(Condon and Ransom, 2016).

For the simple case of having a uniform temperature distribution, it follows from Eq. (2.104) that

$$T_{\mathrm{A}}(\nu) = T_{\mathrm{S}}(\nu) \frac{\Omega_{\mathrm{S}}(\nu)}{\Omega_{\mathrm{B}}(\nu)} = T_{\mathrm{S}}(\nu) \, f_{\mathrm{uni}} \,, \tag{2.108}$$

where f_{uni} is introduced as the beam-filling factor for the uniform case. This provides the most intuitive interpretation of the beam-filling factor: the measured antenna temperature will be equal to the intrinsic source temperature if the source and beam solid angles are equal, i.e., in the case that $f_{\mathrm{uni}} = 1$. However, if the source solid angle is smaller than the beam solid angle, the antenna temperature will be smaller than the actual source temperature due to beam dilution.

Often more accurately, it can be assumed that the source temperature distribution is Gaussian with

$$T_{\mathrm{S}}(\nu, \mathbf{r}) = T_0(\nu) \exp\left(-4 \ln 2 \frac{\mathbf{r}^2}{\theta_{\mathrm{S}}^2}\right), \tag{2.109}$$

where $T_0(\nu)$ is the peak temperature at the source center and θ_S is the full width at half maximum. Equivalently, the normalized power pattern can be written as

$$P_{\mathrm{n}}(\nu, \mathbf{r}) = \exp\left(-4 \ln 2 \frac{\mathbf{r}^2}{\theta_{\mathrm{B}}^2}\right), \tag{2.110}$$

where $\theta_{\mathrm{B}} = \theta_{\mathrm{HPBW}}$. Assuming the beam center coincides with the source center at $(0, 0)$, inserting the above equations into Eq. (2.104) yields

$$T_{\mathrm{A}}(\nu) = T_0(\nu) \frac{\theta_{\mathrm{S}}^2}{\theta_{\mathrm{S}}^2 + \theta_{\mathrm{B}}^2} = T_0(\nu)\, f_{\mathrm{Gauss}}\,. \tag{2.111}$$

Here, the interpretation of the beam-filling factor is less intuitive because having equal source and beam sizes does not give $f_{\mathrm{Gauss}} = 1$, but $f_{\mathrm{Gauss}} = 0.5$. This is the case because Eq. (2.111) calculates T_{A} by scaling a single value of the temperature distribution, i.e., the peak temperature. In fact, f_{Gauss} only approaches unity if $\theta_{\mathrm{S}} \gg \theta_{\mathrm{B}}$, i.e., for very small beams compared to the source. However, the basic principle remains the same: the measured antenna temperature largely depends on the ratio of source size and beam size, and decreases with increasing beam size.

For extended sources in nearby molecular clouds it can often be assumed that $f \approx 1$ (Wilson, 2013). Nevertheless, the effect of beam size must be considered when dealing with, e.g., emission from low-abundance molecules

from a small sub-region of a source, or with maser emission (see section 2.3), which always originates from very small sub-regions. Choosing a single-dish telescope with a higher angular resolution or an interferometer can be appropriate in such cases. For the molecules in the appended papers, there is evidence for extended emission and beam average (LTE) column densities are calculated assuming a beam filling factor of unity (see section 4.2).

An estimate of the source size, and with that, the beam-filling factor, can be derived from Eq. (2.111) by making observations of the same source with (i) two telescopes with different dish sizes or (ii) with the same telescope at two different frequencies. In the first case, the two telescopes need to observe the same frequency (spectral line), and in the second case, the two frequencies (spectral lines) must have (approximately) the same on-sky intensity distribution. Both corresponds to making observations with two different beam sizes $\theta_{\mathrm{B},1}$ and $\theta_{\mathrm{B},2}$ (according to Eq. 2.101), giving two different antenna temperatures $T_{\mathrm{A},1}$ and $T_{\mathrm{A},2}$, i.e.,

$$T_{\mathrm{A},1}(\nu) = T_0(\nu)\frac{\theta_{\mathrm{S}}^2}{\theta_{\mathrm{S}}^2 + \theta_{\mathrm{B},1}^2} \tag{2.112}$$

and

$$T_{\mathrm{A},2}(\nu) = T_0(\nu)\frac{\theta_{\mathrm{S}}^2}{\theta_{\mathrm{S}}^2 + \theta_{\mathrm{B},2}^2}\,. \tag{2.113}$$

Defining the ratio

$$R = \frac{T_{\mathrm{A},1}(\nu)}{T_{\mathrm{A},2}(\nu)} = \frac{\theta_{\mathrm{S}}^2 + \theta_{\mathrm{B},2}^2}{\theta_{\mathrm{S}}^2 + \theta_{\mathrm{B},1}^2} \tag{2.114}$$

makes it possible to solve for the source size

$$\theta_{\mathrm{S}} = \sqrt{\frac{\theta_{\mathrm{B},2}^2 - R\,\theta_{\mathrm{B},1}^2}{R-1}}\,. \tag{2.115}$$

Surface and pointing accuracy

There are some further requirements to ensure that the antenna gain $G(\nu, \mathbf{r})$ (which is directly proportional to the received spectral power) is always at maximum during observations. First, the gain depends on the surface accuracy η_{surf} of a parabolic dish, which is set during telescope construction. If

σ_{surf} is the surface error and λ is the wavelength of observation, the surface accuracy is given by

$$\eta_{\mathrm{surf}}(\lambda) = \exp\left[-\left(\frac{4\pi\sigma_{\mathrm{surf}}}{\lambda}\right)^2\right]. \tag{2.116}$$

Essentially, a radio telescope works reasonably well for wavelengths $\lambda > 16\,\sigma_{\mathrm{surf}}$ (Condon and Ransom, 2016) (see Fig. 2.11, left). Another requirement in order to maximize the gain during an observation is that the telescope is pointed straight at the source at every time with highest precision. If G_0 is the peak gain of a dish, the fractional gain G/G_0 is a function of the pointing error σ_{point}, i.e.,

$$\frac{G}{G_0} = \exp\left[-4\ln 2\left(\frac{\sigma_{\mathrm{point}}}{\theta_{\mathrm{HPBW}}}\right)^2\right] \tag{2.117}$$

(Condon and Ransom, 2016). Thus, keeping pointing errors within 10 % of the beam size ensures that the gain G is $> 97\,\%$ of the peak gain G_0 (see Fig. 2.11, right).

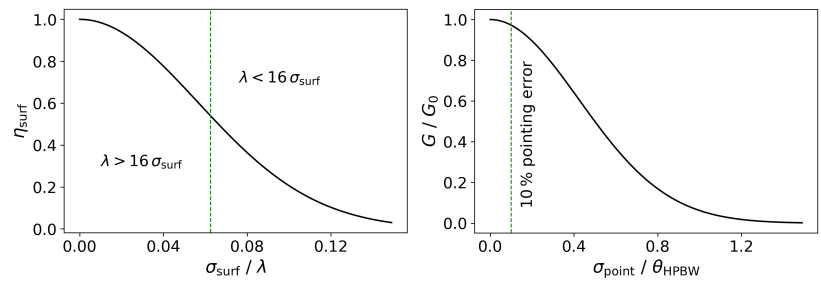

Figure 2.11: Left: surface accuracy η_{surf} of a parabolic dish, calculated from Eq. (2.116). A radio telescope works reasonably well for $\lambda > 16\,\sigma_{\mathrm{surf}}$. **Right:** fractional gain G/G_0 of a telescope as a function of pointing error σ_{point}.

CHAPTER 3

Modeling Spectral Line Intensities

This chapter covers the concepts and equations needed for the modeling of spectral line intensities for molecules at LTE conditions and non-LTE conditions. In case of LTE conditions, calculating spectral line intensities is relatively straightforward using the theoretical framework described in section 3.1. However, in case of non-LTE conditions, sophisticated non-LTE radiative transfer models must be utilized to calculate spectral line intensities. Section 3.2 introduces the basic setup of the non-LTE radiative transfer model `ALI`, which was extensively used in papers B and C. Then, using some simple numeric examples, section 3.3 discusses how the equations of radiative transfer are used to calculate the emergent spectral line intensity of a model source. Lastly, section 3.4 introduces the equations for the convolution of a source intensity distribution with a Gaussian telescope beam.

3.1 LTE Conditions

To calculate the spectral line intensity I_ν for a molecule whose excitation is governed by LTE conditions is trivial and does not require any assumptions about source geometry. As was discussed in section 2.4, for the case of LTE conditions, the source function for spectral line radiation can simply be written as $S_\nu = B_\nu(T_{\rm ex})$ (Eq. 2.74), where it is assumed that $T_{\rm ex} = T_{\rm k} = T$. Inserting this into Eq. (2.68) gives

$$I_\nu = B_\nu(T_{\rm bg})\,{\rm e}^{-\tau_\nu} + B_\nu(T_{\rm ex})\Big[1 - {\rm e}^{-\tau_\nu}\Big]\,. \tag{3.1}$$

That is, the only parameters that need to be estimated are source kinetic temperature $T_{\rm k}$, background temperature $T_{\rm bg}$, and optical depth τ_ν.

When carrying out observations towards a molecular cloud source, the above definition of spectral intensity can then be used to specify the expression for the radiation intensity, i.e., Eq. (2.99). Essentially, the measured on-source/on-frequency intensity $I_\nu^{\rm on}$ is then given by Eq. (3.1), while the off-source/off-frequency intensity $I_\nu^{\rm off}$ can simply be taken as

$$I_\nu^{\rm off} = B_\nu(T_{\rm bg})\,. \tag{3.2}$$

Then, the measured intensity difference ΔI_ν is

$$\Delta I_\nu = I_\nu^{\rm on} - I_\nu^{\rm off} = \Big[B_\nu(T_{\rm ex}) - B_\nu(T_{\rm bg})\Big]\Big[1 - {\rm e}^{-\tau_\nu}\Big] \tag{3.3}$$

(Mangum and Shirley, 2015; Yamamoto, 2017). Here, it is common to introduce the Rayleigh-Jeans equivalent temperature of blackbody radiation intensity as

$$J_\nu(T) = \frac{B_\nu(T)c^2}{2k_{\rm B}\nu^2} = \frac{h\nu}{k_{\rm B}}\left[\exp\left(\frac{h\nu}{k_{\rm B}T}\right) - 1\right]^{-1}\,, \tag{3.4}$$

where $B_\nu(T)$ is given by Planck's law (Mangum and Shirley, 2015), i.e., Eq. (2.8). It then follows that Eq. (3.3) can be rewritten as

$$\Delta I_\nu = \frac{2k_{\rm B}\nu^2}{c^2}\Big[J_\nu(T_{\rm ex}) - J_\nu(T_{\rm bg})\Big]\Big[1 - {\rm e}^{-\tau_\nu}\Big]\,. \tag{3.5}$$

In the Rayleigh-Jeans limit, the measured radiation temperature $T_{\rm R}$ can then be defined as

$$T_{\rm R}(\nu) = \frac{\Delta I_\nu c^2}{2k_{\rm B}\nu^2} = \Big[J_\nu(T_{\rm ex}) - J_\nu(T_{\rm bg})\Big]\Big[1 - {\rm e}^{-\tau_\nu}\Big]\,. \tag{3.6}$$

Under the assumption of LTE conditions, and by considering the beam filling factor f (Eq. 2.108), the relation to the measured antenna temperature is

$$T_{\rm A}(\nu) = fT_{\rm R}(\nu) = f\,\Big[J_\nu(T_{\rm ex}) - J_\nu(T_{\rm bg})\Big]\Big[1 - {\rm e}^{-\tau_\nu}\Big]\,. \tag{3.7}$$

The above equations simplify further if it is assumed that we have optically thin conditions with $\tau_\nu \to 0$. The remainder of this chapter focuses on the concepts and equations for the modeling of spectral line intensities for non-LTE conditions.

3.2 Non-LTE Conditions: ALI

For a molecule whose excitation is governed by non-LTE conditions, sophisticated non-LTE radiative transfer (RT) models must be utilized to calculate line intensities. The underlying idea of such models will be discussed in this section via the example of the ALI (accelerated lambda iteration) model, developed by P. Bergman (OSO) and based on the formulation by Rybicki and Hummer (1991).

The ALI model is a 2D model that assumes a spherically symmetric molecular cloud source with radius R, internally separated into a number of shells, and interacting with a background radiation field with $B_\nu(T_{\rm bg})$, where $T_{\rm bg}$ is the background temperature[1] (Fig. 3.1). In its baseline version, it is assumed that the cloud only consists of H_2 and a target molecule "mol", and that it has kinetic temperature $T_{\rm k}$, volume density $n(H_2)$, and abundance $X({\rm mol}) = n({\rm mol})/n(H_2)$. The effect of dust opacity (i.e., absorbance) $\kappa_{\rm d}$ can be included as well, in which case a total source function must be considered, taking into account the combined effects of absorbance by molecules and dust.

[1] It is also possible to consider another blackbody source at the center of the cloud, in order to model the effect of, e.g., a protostar. There is also a version of ALI that is suited for the modeling of molecular emission lines from comets.

Many of the physical conditions, like temperature, density, and abundance, can be described with constants or radial gradients.

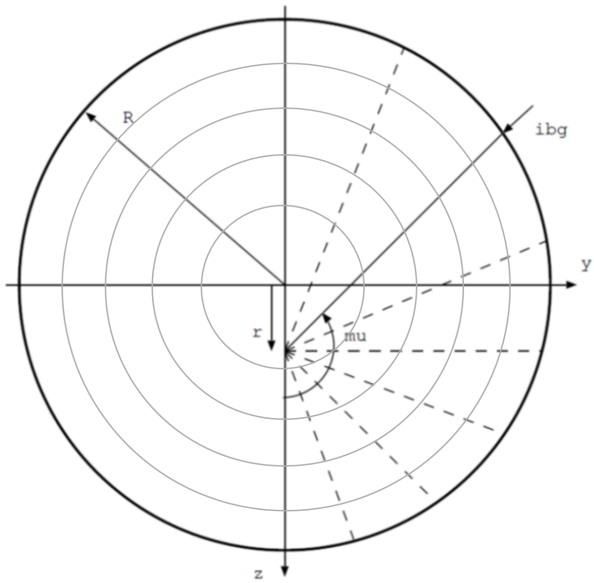

Figure 3.1: Schematic cut through a spherically symmetric molecular cloud source as considered in `ALI`. Credit: P. Bergman (OSO).

The major goal of every non-LTE RT model is to obtain a consistent SE (statistical equilibrium) energy level population for the target molecule at every position $\mathbf{r}$ in the cloud. According to Eqs. (2.72), (2.75), and (2.77), the level populations are then used to determine the source function $S_\nu(\mathbf{r})$, absorbance $\alpha_\nu(\mathbf{r})$, and optical depth $\tau_\nu(\mathbf{r})$, respectively. These parameters are then further used to calculate the emergent intensity coming from the cloud, utilizing the RT equations from section 2.4. An integral feature of the `ALI` model is that it can assume a velocity field, in which the molecules are moving. Following the discussion of spectral line shape in section 2.5, this gives an intensity distribution around a considered transition frequency. Effectively, the `ALI` model assumes a Doppler broadened frequency (or velocity) profile whose width depends on the position-dependent values of kinetic temperature

and turbulent velocity $v_{\rm turb}$ (Eqs. 2.92 and 2.94). It is furthermore possible to assume radial velocity gradients to model an expanding or contracting cloud. The effect of a velocity field on the shape of the spectral line intensity profile of a cloud is discussed in more detail in section 3.3.

With a few simple approximations, the number of positions $\mathbf{r}$ to consider decreases significantly (see Fig. 3.1). First of all, based on the assumption that the cloud is spherically symmetric, only positions in one half of a sphere, and only one position per shell need to be considered (if it is assumed that each shell is physically and chemically homogeneous). For simplicity, the considered positions can be taken to be points along a line through the center of the cloud (e.g., points along the z-axis). The level population at every point $(0, 0, z)$ is affected by the absorption and emission of photons, i.e., by the level populations, at other surrounding positions (x, y, z). To obtain the level population at exemplary point $(0, 0, r)$, different paths at different possible angles are considered (dashed lines), through which that point receives radiation from other points in the cloud. Along every path, is is assumed that the initial radiation intensity is the background intensity $I_\nu(0) = B_\nu(T_{\rm bg})$ ("ibg" in Fig. 3.1).

When first entering the cloud, and along with particle collisions, the background radiation will produce a certain level population at a point (y, z) close to the edge, according to Eq. (2.48), written slightly adjusted as

$$\frac{\mathrm{d}}{\mathrm{d}t} n_i(y,z) = \sum_{j\neq i}^{N} n_j(y,z) P_{ji} - n_i(y,z) \sum_{j\neq i}^{N} P_{ij} = 0\,, \tag{3.8}$$

where now

$$P_{ij} = \begin{cases} A_{ij} + B_{ij} I_\nu(0) + C_{ij} & , \text{if } i > j \\ B_{ij} I_\nu(0) + C_{ij} & , \text{if } i < j\,. \end{cases} \tag{3.9}$$

The level population gives the values of $S_\nu(y, z)$, $\alpha_\nu(y, z)$, and $\tau_\nu(y, z)$, which gives a certain radiation intensity $I_\nu(y, z)$, according to Eq. (2.67), written slightly adjusted as

$$I_\nu(y,z) = I_\nu(0)\,\mathrm{e}^{-\tau_\nu(y,z)} + S_\nu(y,z)\left[1 - \mathrm{e}^{-\tau_\nu(y,z)}\right] \tag{3.10}$$

This intensity is then used as the "background intensity" $I_\nu(0)$ for the next point (y, z) along the considered path, and so forth until reaching point $(0, r)$. At that point, the average intensity $\langle I(0,r)\rangle$ is then obtained by integration over solid angle Ω (considering all paths to that point) and frequency, i.e.,

$$\langle I(0,r)\rangle = \frac{1}{4\pi}\int \mathrm{d}\Omega \int I_\nu(y,z)\,\mathrm{d}\nu. \tag{3.11}$$

Note that Eqs. (3.8) – (3.10) must be solved for a range of frequencies to consider the spread in intensity. The final level population at is then obtained as

$$\frac{\mathrm{d}}{\mathrm{d}t}n_i(0,r) = \sum_{j\neq i}^{N} n_j(0,r)P_{ji} - n_i(0,r)\sum_{j\neq i}^{N} P_{ij} = 0\,, \tag{3.12}$$

with

$$P_{ij} = \begin{cases} A_{ij} + B_{ij}\langle I(0,r)\rangle + C_{ij} & , \text{if } i > j \\ B_{ij}\langle I_\nu(0,r)\rangle + C_{ij} & , \text{if } i < j\,. \end{cases} \tag{3.13}$$

Of course, the equations above are written for the particular point $(0, r)$, but can be written more generally for an arbitrary position $\mathbf{r}$ as

$$\frac{\mathrm{d}}{\mathrm{d}t}n_i(\mathbf{r}) = \sum_{j\neq i}^{N} n_j(\mathbf{r})P_{ji} - n_i(\mathbf{r})\sum_{j\neq i}^{N} P_{ij} = 0\,, \tag{3.14}$$

with

$$P_{ij} = \begin{cases} A_{ij} + B_{ij}\langle I(\mathbf{r})\rangle + C_{ij} & , \text{if } i > j \\ B_{ij}\langle I_\nu(\mathbf{r})\rangle + C_{ij} & , \text{if } i < j\,, \end{cases} \tag{3.15}$$

where

$$\langle I(\mathbf{r})\rangle = \frac{1}{4\pi}\int \mathrm{d}\Omega \int I_\nu(\mathbf{r}')\,\mathrm{d}\nu\,, \tag{3.16}$$

with

$$I_\nu(\mathbf{r}') = I''_\nu\,\mathrm{e}^{-\tau_\nu(\mathbf{r}')} + S_\nu(\mathbf{r}')\left[1 - \mathrm{e}^{-\tau_\nu(\mathbf{r}')}\right]. \tag{3.17}$$

In the last equation, $\mathbf{r}'$ denotes another position at a given distance from $\mathbf{r}$, while I''_ν denotes the received spectral intensity at $\mathbf{r}'$, obtained at a previous position $\mathbf{r}''$. Thereby, $\mathbf{r}$, $\mathbf{r}'$, and $\mathbf{r}''$ are lying on a line connecting the outside of the cloud with point $\mathbf{r}$.

In order to obtain a consistent set of level populations throughout the cloud, the above equations must be solved iteratively, and simultaneously for all considered positions (shells) and a number of angles. This process can be separated into three major steps:

(1) Assume LTE conditions at a constant excitation temperature $T_{\rm ex}$, giving the initial level populations $n_i^{\rm ini}$ in all shells.

(2) Solve the set of SE and RT equations (Eqs. 3.14 – 3.17) to obtain $\langle I(\mathbf{r})\rangle$ in every shell.

(3) Calculate new level populations $n_i^{\rm new}$ based on $\langle I(\mathbf{r})\rangle$.

Then, steps (2) and (3) are repeated until convergence, i.e., until the difference between $n_i^{\rm new}$ and $n_i^{\rm old}$ is smaller than a considered boundary value[2]. Accelerated lambda iteration (that gives ALI its name) is a specific method to solve the above set of differential equations (Rybicki and Hummer, 1991). The derivation of molecular column densities using non-LTE RT models (as is done in papers B and C), is further described in section 4.4.

Alternative models exist for both simpler and more complex considerations. For example, in the RT model RADEX[3], the direct interdependences of level populations and radiation intensities in different parts of the cloud are neglected. Instead, a global average intensity $\langle I_\nu\rangle$ is obtained by considering a geometrically averaged photon escape probability β, such that

$$\langle I_\nu\rangle = S_\nu(1-\beta)\,. \tag{3.18}$$

Essentially, β depends on the optical depth of the medium and takes different values for different approximations and geometries (van der Tak et al., 2007). An often used approximation is the so-called large velocity gradient (LVG) model, in which it is assumed that velocity gradients in the cloud are sufficiently large such that a released photon will not interact with molecules in between its point of release and the edge of the cloud. In that case,

$$\beta_{\rm LVG} = \frac{1-{\rm e}^{-\tau_\nu}}{\tau_\nu} \tag{3.19}$$

[2]For a smooth convergence, the current level population can be taken as a fraction of $n_i^{\rm new} + n_i^{\rm old}$.

[3]https://home.strw.leidenuniv.nl/~moldata/radex.html.

(Gußmann, 1979; de Jong et al., 1980; van der Tak et al., 2007), such that $\beta_{\mathrm{LVG}} \to 1$ if $\tau_\nu \ll 1$, but $\beta_{\mathrm{LVG}} \approx 1/\tau_\nu \to 0$ if $\tau_\nu \gg 1$. That is, the escape probability approaches unity for low optical depths, but $1/\tau_\nu$ for high optical depths. On the other hand, a more complex treatment is provided in, e.g., the RT model `LIME`[4], which calculates the level populations and radiation field iteratively like `ALI`, but in 3D to treat treat asymmetrical source geometries (Brinch and Hogerheijde, 2010).

3.3 Emergent Line Intensity

This section uses some simple numeric examples to showcase the calculation of the emergent spectral line intensity of a model cloud using the RT equations introduced in section 2.4. First, this is done for the simplest case of calculating the intensity only at a certain transition frequency, neglecting any line broadening processes. Eventually, the numeric example is expanded to discuss the influence of a velocity field on the width of the modeled spectral line profile.

No line broadening

Assuming a consistent SE level population was obtained for all positions in a model cloud, the emergent intensity of the cloud at a certain transition frequency is calculated by using Eq. (2.66) for lines of sight (LOSs) through the cloud. Considering a spherically symmetric cloud in a 3D coordinate system, observed from the outside, the intensity emerging from the cloud surface at position (x, y) is then given by

$$I_\nu(x,y) = I_\nu^{\mathrm{bg}}\, \mathrm{e}^{-\tau_\nu(x,y)} + \int_{\tau_\nu^0=0}^{\tau_\nu(x,y)} S_\nu(\mathbf{r})\, \mathrm{e}^{-[\tau_\nu(x,y)-\tau_\nu(\mathbf{r})]}\, \mathrm{d}\tau_\nu\,, \tag{3.20}$$

where I_ν^{bg} is the background radiation intensity, $\tau_\nu(x,y)$ is the total optical depth for the considered LOS, and $S_\nu(\mathbf{r})$ and $\tau_\nu(\mathbf{r})$ are the source function and optical depth at position $\mathbf{r} = (x, y, z)$ inside the cloud. The total optical depth is given as

$$\tau_\nu(x,y) = \int_0^{L(x,y)} \alpha_\nu(\mathbf{r})\, \mathrm{d}z\,, \tag{3.21}$$

[4] https://github.com/lime-rt/lime.

where $L(x, y)$ is the path length through the cloud at position (x, y), and $\alpha_\nu(\mathrm{r})$ is the absorbance at position r. Equivalently, $\tau(\mathbf{r})$ is the cumulative optical depth defined via the above integral up to a certain depth z, while $\mathrm{d}\tau_\nu = \alpha_\nu(\mathbf{r})\,\mathrm{d}z$ (Eq. 2.55).

Numerically, solving Eq. (3.20) above can be approached by first dividing the cloud into a number of N shells, each characterized by specific values $S_{\nu,i}$ and $\alpha_{\nu,i}$. Then, Eq. (2.67) is utilized stepwise, starting from the outside of the cloud and following a LOS through the different shells. At a given (plane) distance $d(x, y) = \sqrt{x^2 + y^2}$ from the cloud center at $(x, y) = (0, 0)$, the total chord (path) length through the cloud is given as

$$L(x, y) = 2\sqrt{R^2 - d(x, y)^2} = \sum_i^N L_i(x, y)\,, \tag{3.22}$$

where R is the cloud radius. Furthermore, $L_i(x, y)$ is the chord length through the ith shell, given as

$$L_i(x, y) = 2\left(\sqrt{r_{\mathrm{out}}^2 - d(x, y)^2} - \sqrt{r_{\mathrm{in}}^2 - d(x, y)^2}\right)\,, \tag{3.23}$$

where r_{in} is the inner radius and r_{out} is the outer radius of the shell. Some shells contribute twice to the change in intensity along a path through the cloud. To take this into account, one can define segments $\Delta z_i^{\mathrm{far}} = \Delta z_i^{\mathrm{near}} = L_i/2$ and order them as

$$[\Delta z_N^{\mathrm{far}}, \ldots, \Delta z_1^{\mathrm{far}}, \Delta z_1^{\mathrm{near}}, \ldots, \Delta z_N^{\mathrm{near}}]\,, \tag{3.24}$$

giving a total number of $2N$ chord length segments for each LOS. Calling the segments with subscript j, Eq. (2.67) then becomes

$$I_{\nu,j}(x, y) = I_{\nu,j-1}(x, y)\,\mathrm{e}^{-\Delta\tau_{\nu,j}} + S_{\nu,j}(1 - \mathrm{e}^{-\Delta\tau_{\nu,j}})\,, \tag{3.25}$$

where $\Delta\tau_{\nu,j} = \alpha_{\nu,j}\Delta z_j$.

The above equations are used in a simple numeric example, considering a model cloud with radius $R = 2 \times 10^{17}\,\mathrm{cm}$, divided into 50 shells, assuming background intensity $I_\nu^{\mathrm{bg}} = 2.7\,\mathrm{K}$. The source function at the cloud center is

$S_\nu = 10\,\mathrm{K}$; it is assumed to linearly decrease with radius to reach 3 K in the outermost shell. For simplicity, the absorbance is assumed to be constant at $\alpha_\nu = 5 \times 10^{-18}\,\mathrm{cm}^{-1}$. Eq. (3.25) is then solved for a grid of (x, y) values, giving the intensity map, shown in Fig. 3.2. Using this equation to update the intensity in steps while going through the separate shell segments is equivalent to the single expression

$$I_\nu(x,y) = I_\nu^{\mathrm{bg}}\,\mathrm{e}^{-\tau_\nu(x,y)} + \sum_j^{2N} S_{\nu,j}(1 - \mathrm{e}^{-\Delta\tau_{\nu,j}})\,\mathrm{e}^{-[\tau_\nu(x,y)-\tau_\nu(\mathbf{r})]}\,, \tag{3.26}$$

which is furthermore equivalent to the analytical expression above (Eq. 3.20). Here, the total optical depth is given as

$$\tau_\nu(x,y) = \sum_j^{2N} \alpha_{\nu,j}\Delta z_j\,, \tag{3.27}$$

while $\tau_\nu(\mathbf{r})$ is the cumulative optical depth up to a certain segment j.

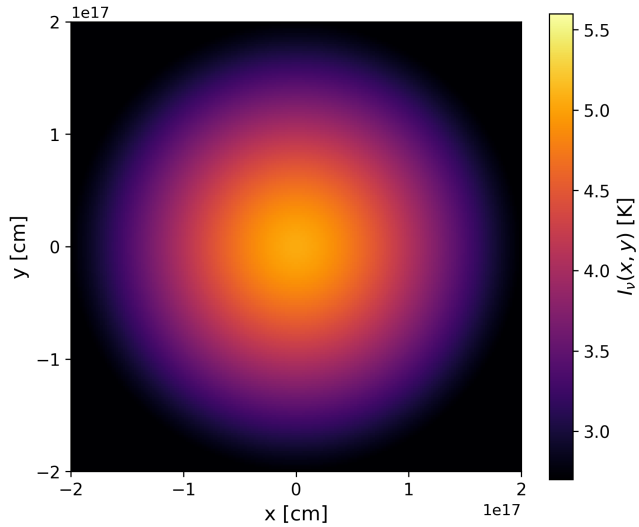

Figure 3.2: Intensity map $I(x, y)$ calculated from Eq. (3.25) for a cloud with $R = 2 \times 10^{17}\,\mathrm{cm}$, divided into 50 shells with varying S_ν and constant $\alpha_\nu = 5 \times 10^{-18}\,\mathrm{cm}^{-1}$.

The importance of optical depth

The optical depth is a crucial parameter that determines how many photons from the background radiation or from a certain depth in the cloud are actually able to escape the cloud. First, the total optical depth gives a direct estimate of how much of the background radiation survives the journey through the cloud. As can be seen from Eqs. (3.20) and (3.26), at $\tau_\nu(x, y) \ll 1$, the attenuation of the background intensity is negligible and it strongly contributes to the final emergent intensity. However, at $\tau_\nu(x, y) \gg 1$, the contribution of the background intensity to the emergent intensity becomes very small, meaning that most of the intensity is produced inside the cloud itself. Furthermore, defining

$$\tau_\nu(x, y) - \tau_\nu(\mathbf{r}) = \tau_\nu^{\text{diff}}\,, \tag{3.28}$$

the cloud attenuation factor $\exp(-\tau_\nu^{\text{diff}})$ determines how much of the radiation emitted at a certain depth survives the passage to the surface. Equivalent to the case of the background radiation, if τ_ν^{diff} is high, almost none of the radiation from the considered depth will leave the cloud.

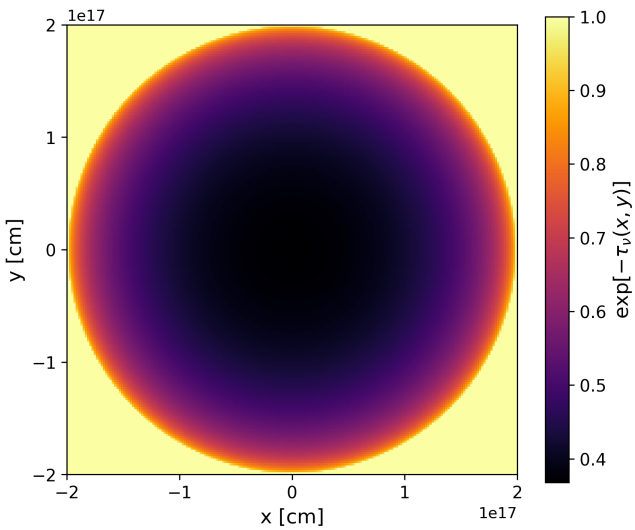

Figure 3.3: Background attenuation factor $\exp[-\tau_\nu(x, z)]$; $\tau_\nu(x, z)$ calculated from Eq. (3.27).

Considering the $\tau_\nu(x, y)$ map calculated from Eq. (3.27), Fig. 3.3 shows the attenuation factor ($\exp[-\tau_\nu(x, y)]$) for the background intensity. As can be seen, at the considered conditions, about 40 % of the background intensity contributes to the emergent intensity for central LOSs. Fig. 3.4 shows the intensity map calculated for a higher absorbance of $2 \times 10^{17}\,\mathrm{cm}^{-1}$. At those conditions, almost none of the background radiation contributes to the emergent intensity on the near side of the cloud as $\exp[-\tau_\nu(x, y)] \approx 0$ for almost all LOSs. Furthermore, the cyan contour in Fig. 3.4 marks the $\tau_\nu(\mathbf{r})$ surface that corresponds to $\tau_\nu^{\mathrm{diff}} = 3$, defined via Eq. (3.28), while also marking a critical depth z_{crit} via the z-dependency of $\tau_\nu(\mathrm{r})$. Photons emitted from depths $z > z_{\mathrm{crit}}$ are likely to be reabsorbed by material in front of it, while most photons that actually leave the cloud are coming from depths $z < z_{\mathrm{crit}}$. That is, at large optical depths, information is lost about where in the cloud the radiation is coming from, and the actual depth up to which one can look into a cloud becomes limited.

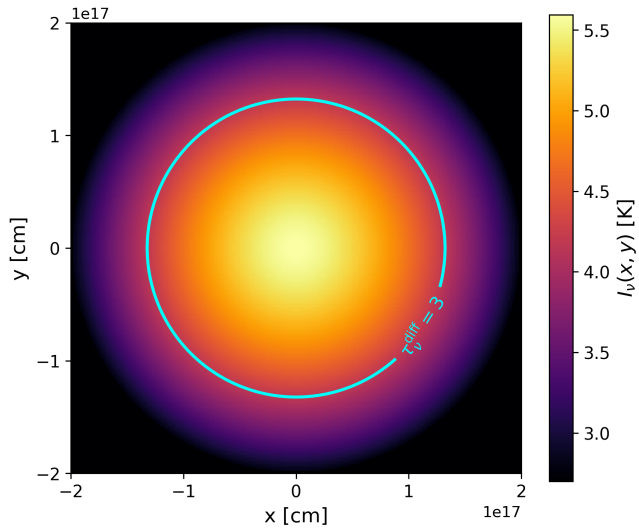

Figure 3.4: Same as Fig. 3.2 but for $\alpha_\nu = 2 \times 10^{-17}\,\mathrm{cm}^{-1}$. The dashed cyan contour marks the $\tau_\nu(\mathbf{r})$ surface that corresponds to $\tau_\nu^{\mathrm{diff}} = 3$ (Eq. 3.28).

In general, and still assuming the absorbance is constant in all shells, the total optical depth increases linearly with increasing absorbance. However,

the emergent intensity will go through a maximum before falling off. This is shown in Fig. 3.5 for the longest LOS through the cloud center at $(0, 0)$. At very high optical depths, the intensity approaches the source function of the outermost shell (3 K here), which is an extreme limiting case in which all photons escaping the cloud are coming from this shell, and at which the emergent intensity looks uniform. For most molecular lines, such extreme conditions are rarely reached. However, spectral lines of CO are an exception and can reach very high optical depths.

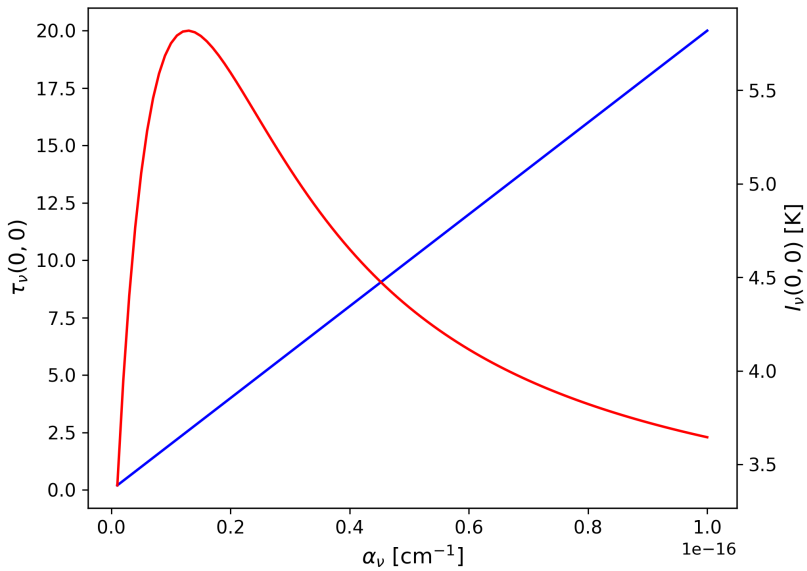

Figure 3.5: Total optical depth $\tau_\nu(x, y)$ (blue) and emergent intensity $I_\nu(x, y)$ (red) for the central LOS at $(0, 0)$ as a function of absorbance α_ν, assumed to be constant in all shells.

Considering a velocity field

The expressions and figures for the numeric examples above are all valid for a single frequency. However, as was discussed in section 2.5, the emergent line intensity from a cloud is actually spread out in frequency or, equivalently, velocity due to the motions of molecules in the gas. In the following, concepts and equations are expressed in the velocity domain.

In cold molecular cloud sources, the velocity profile $\phi(v)$ is a Doppler broadened (Gaussian) profile that is largely determined by the turbulent gas velocity v_{turb} (see section 2.5, Eqs. 2.94). It can be written as

$$\phi(v) = \frac{1}{v_{\mathrm{turb}}\sqrt{\pi}} \exp\left(-\frac{v^2}{v_{\mathrm{turb}}^2}\right), \tag{3.29}$$

where $1/v_{\mathrm{turb}}\sqrt{\pi}$ is the normalization constant from the requirement that $\int \phi(v)\,\mathrm{d}v = 1$ (Eq. 2.71). Allowing for LOS gas motions with velocity v_{LOS} towards or away from an observer and using the general relation between v_{turb} and the full width at half maximum Δv of the Gaussian profile, i.e.,

$$v_{\mathrm{turb}} = \frac{\Delta v}{\sqrt{4\ln 2}}, \tag{3.30}$$

the velocity profile can be written equivalently as

$$\phi(v) = \frac{\sqrt{4\ln 2}}{\Delta v\sqrt{\pi}} \exp\left[-4\ln 2\left(\frac{v - v_{\mathrm{LOS}}}{\Delta v}\right)^2\right], \tag{3.31}$$

where v_{LOS} is the LOS projected velocity of the radial velocity v_{rad}, when considering an expanding or contracting cloud. In general v_{rad} has a negative/positive sign in the contracting/expanding case.

In order to expand the numeric example above to account for a velocity profile, the absorbance is calculated as

$$\alpha_v = \alpha_0\,\phi(v), \tag{3.32}$$

where α_0 is the peak absorbance, assumed to be given by the SE level population in a certain shell (Eq. 2.75)[5]. Then, Eq. (3.25) is applied for all LOSs and a range of velocities v. In the following, it is assumed that $\Delta v = 0.5\,\mathrm{km\,s^{-1}}$ while considering $v \in [-1.5, 1.5]\,\mathrm{km\,s^{-1}}$, split into 200 velocity channels. Fur-

[5]The units of α_0 are $\mathrm{cm^{-1}\,(km\,s^{-1})^{-1}}$, such that integrating the absorbance profile over velocity yields units of $\mathrm{cm^{-1}}$. Hence, the optical depth τ_ν, derived by integration of the absorbance along a LOS (Eq. 3.21), has dimensions of $\mathrm{(km\,s^{-1})^{-1}}$ and becomes dimensionless by integration over velocity.

thermore, the assumed values for R, I_v^{bg}, and S_v are the same as in the example above, but only $N = 20$ shells are considered.

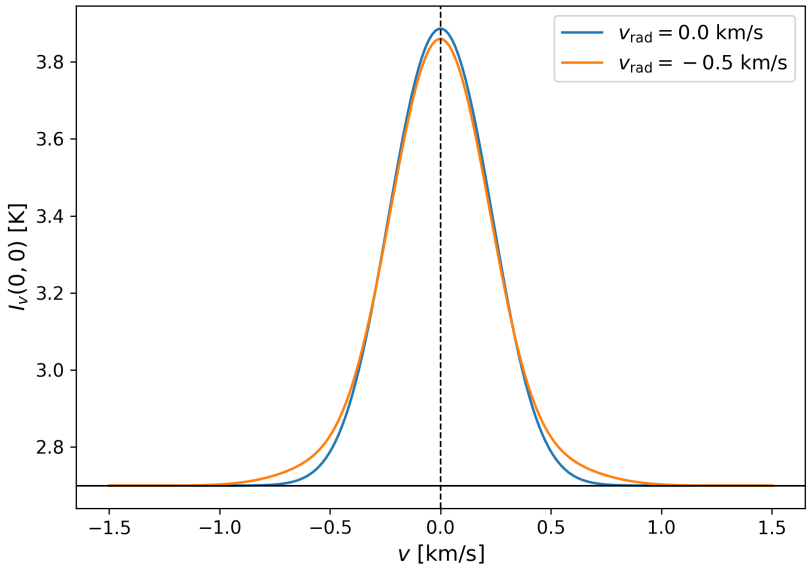

Figure 3.6: Emergent intensity I_v for the central LOS at $(0, 0)$ assuming $\alpha_0 = 10^{-18}\,\mathrm{cm}^{-1}$ and a velocity profile described by Eq. (3.31) for $v_{\mathrm{rad}} = 0\,\mathrm{km\,s}^{-1}$ (static case; blue) and $v_{\mathrm{rad}} = -0.5\,\mathrm{km\,s}^{-1}$ (contracting case; orange).

Fig. 3.6 shows the emergent intensity as a function of velocity for the central LOS, assuming $\alpha_0 = 10^{-18}\,\mathrm{cm}^{-1}$. As can be seen, the intensity "baseline" is at the background intensity $I_\nu^{\mathrm{bg}} = 2.7\,\mathrm{K}$. The blue line is for the case of having no net gas motions towards or away from an observer, i.e., $v_{\mathrm{LOS}} = v_{\mathrm{rad}} = 0\,\mathrm{km\,s}^{-1}$ (static case). The orange line is for the case of a contracting cloud, assuming that molecules in the outermost five shells are moving towards the center of the cloud with constant radial velocity $v_{\mathrm{rad}} = -0.5\,\mathrm{km\,s}^{-1}$. That is, from the perspective of an observer, molecules on the near side of the cloud are receding while molecules on the far side are approaching. Effectively, the molecules in the outermost five shells are emitting and absorbing photons at fundamentally different velocities (frequencies) than molecules in the central part of the cloud, giving rise to the observed line wing emission on both sides. The

red-shifted wing (on the right side) stems from receding molecules on the near side, while the blue-shifted wing (on the left side) stems from approaching molecules on the far side.

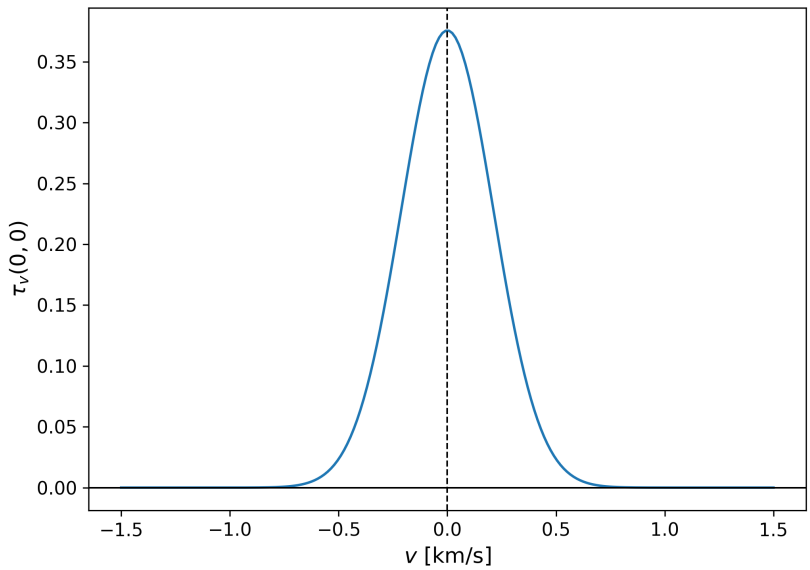

Figure 3.7: Optical depth τ_ν for the central LOS at $(0, 0)$ calculated via Eqs. (3.27) and (3.32) for $\alpha_0 = 10^{-18}\,\mathrm{cm}^{-1}$ and a velocity profile with $v_{\mathrm{rad}} = 0\,\mathrm{km\,s}^{-1}$ (static case).

It is important to note that, in an optically thin medium and under the simplified conditions considered here, it is not possible to separate between a contracting cloud and an expanding cloud based on the intensity distribution, because both cases produce the same symmetric outcome. That is, reversing the sign of v_{rad}, molecules on the near side would approach while molecules on the far side would recede, but the intensity distribution would look the same. The optical depth is an important factor here, because in an optically thin medium, an observer receives photons from deep cloud layers. Of course, as the absorbance is now a function of velocity, also the optical depth becomes a function of velocity (Eq. 3.27). The optical depth profile for the central LOS and the static case ($v_{\mathrm{rad}} = 0\,\mathrm{km\,s}^{-1}$) is shown in Fig. 3.7.

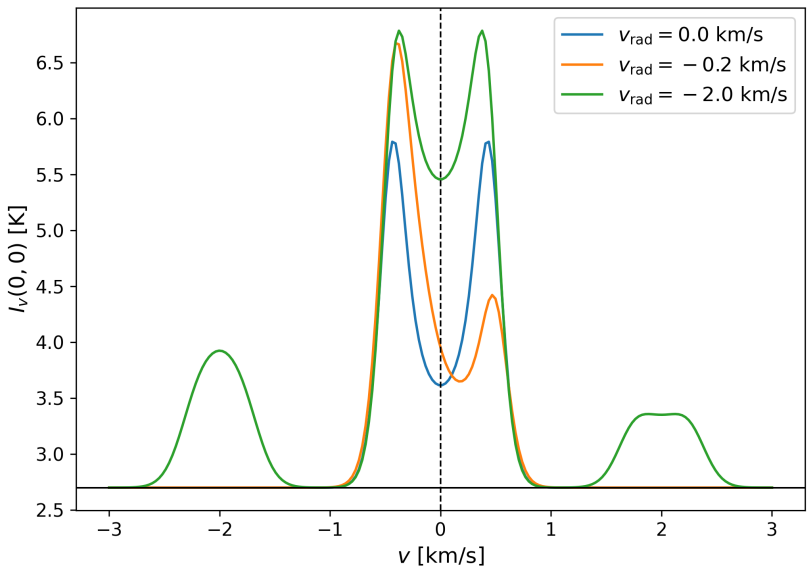

Figure 3.8: Same as Fig. 3.6 but for $\alpha_0 = 5 \times 10^{-17}\,\mathrm{cm}^{-1}$ and contracting cases with $v_{\rm rad} = -0.2\,\mathrm{km\,s}^{-1}$ (orange line) and $v_{\rm rad} = -2.0\,\mathrm{km\,s}^{-1}$ (green line).

Fig. 3.8 shows the emergent intensity distribution for the central LOS, assuming a higher absorbance of $\alpha_0 = 5 \times 10^{-17}\,\mathrm{cm}^{-1}$. In case of a static cloud (blue line), the intensity shows a strong symmetric dip, which arises from the (self-)absorption of photons by molecules along the LOS to the observer. That is, the optical depth for the central LOS becomes high and reaches a peak of about 17 (the shape is the same as in Fig. 3.7). Comparing to Fig. 3.5, $I_v(0,0)$ is in the regime past the peak intensity. If the absorbance would be increased even further, to values $> 10^{-16}\,\mathrm{cm}^{-1}$, one would observe a dip that reaches down to the value of the source function in the outermost shell, i.e., down to 3 K. The orange line in Fig. 3.8 is for a contracting cloud with $v_{\rm rad} = -0.2\,\mathrm{km\,s}^{-1}$. An asymmetry emerges for the same reason already mentioned above: the molecules in the far side shells, the central shells, and near side shells are moving at different velocities and photons emitted by the molecules in different cloud regions interact less with molecules in other re-

gions[6]. For the case of an expanding cloud, the profile would appear mirrored. It is important to note that there are still interactions between photons and molecules in the different shells of the cloud because of the velocity profile (turbulent gas velocity), which is assumed to be same for all positions in the cloud. In the current example $\Delta v = 0.5\,\mathrm{km\,s^{-1}}$ while $v_{\mathrm{rad}} = -0.2\,\mathrm{km\,s^{-1}}$. If we instead assume a radial velocity that is significantly larger than Δv, photons from the far side shells, central shells, and near side shell become fully decoupled, giving rise to three distinct velocity components. This is shown in Fig. 3.8 for $v_{\mathrm{rad}} = -2\,\mathrm{km\,s^{-1}}$ (green line). As can be seen, the optical depth in the central cloud shells becomes large enough for significant self-absorption. Some self-absorption is also observed for the emission from molecules on the near side (the peak at $v_{\mathrm{rad}} = 2\,\mathrm{km\,s^{-1}}$). The *o*-$H_2S(1_{1,0}\text{-}1_{0,1})$ line analyzed in paper C shows an asymmetric profile with an infall signature that is modeled with `ALI`.

3.4 Beam Convolution

In order to model the intensity of a spectral line as would be observed when pointing a telescope at the cloud, the emergent spectral line intensity of the cloud must be convolved with an assumed beam shape function. The following convolution method is also used to calculate beam convolved column densities in papers B and C (see section 4.4).

Assuming a 2D Gaussian beam (section 2.6), the beam-shape function can be written in matrix notation as

$$g(\mathbf{r}) = \frac{1}{2\pi}\det(\Sigma)^{-1/2}\exp\left[-\frac{1}{2}\left\langle \mathbf{r}-\mathbf{r}_{0,\mathrm{b}}\left|\Sigma^{-1}\right|\mathbf{r}-\mathbf{r}_{0,\mathrm{b}}\right\rangle\right], \tag{3.33}$$

where $\mathbf{r}_{0,\mathrm{b}} = (x_{0,\mathrm{b}}, y_{0,\mathrm{b}})$ is the assumed beam center, and

$$\Sigma = \begin{pmatrix}\sigma_x^2 & 0\\ 0 & \sigma_y^2\end{pmatrix} \tag{3.34}$$

[6] In the LVG approximation of some non-LTE radiative transfer codes it is basically assumed that velocity gradients in the different layers of a cloud are large enough such that photons emitted at one position in a cloud do never interact with molecules in another part of a cloud. Therefore, non-local effects such as self-absorption cannot be considered with such models.

is the covariance matrix, containing the Gaussian standard deviations σ_x and σ_y, which, for a circular beam, can be expressed in terms of the half power beam width θ_{HPBW} as

$$\sigma_x = \sigma_y = \frac{\theta_{\mathrm{HPBW}}}{2\sqrt{2\ln 2}}\,. \tag{3.35}$$

Based on the distance D to the cloud (in cm), the beam width is converted from arcsec to centimeter via

$$\theta_{\mathrm{cm}} = \frac{D_{\mathrm{cm}}\theta_{\mathrm{arcsec}}}{60^2 \times 180/\pi}\,. \tag{3.36}$$

Numerically, and assuming an intensity distribution $I_v(x, y)$ at a certain velocity, the beam convolved (average) intensity $\langle I_v \rangle$ is then calculated as

$$\langle I_v \rangle = \sum I_v(x, y)\, g(x, y)\, \Delta r = T_{\mathrm{A}}\,, \tag{3.37}$$

where $\Delta r = \Delta x\, \Delta y$. Following the discussion in section 2.6, $\langle I_v \rangle$ can be identified as a modeled antenna temperature T_{A}. One of the most basic properties derived from radio-astronomical spectral line observations is the integrated line intensity, simply defined as

$$\int T_{\mathrm{A}}\, \mathrm{d}v\,. \tag{3.38}$$

The above equations are applied for the numeric example of a static cloud with $\alpha_0 = 10^{-18}\,\mathrm{cm}^{-1}$ from the previous section. The top panel of Fig. 3.9 shows the emergent source intensity for $v = 0\,\mathrm{km\,s}^{-1}$. The bottom panel further shows the beam shape function as calculated from Eq. (3.33) for $\theta_{\mathrm{HPBW}} =$ 45" and a distance of 300 pc. Then, Fig. 3.10 shows T_{A} calculated from Eq. (3.37) for the 200 velocity channels in the interval $v = [-1.5, 1.5]\,\mathrm{km\,s}^{-1}$ and for $\theta_{\mathrm{HPBW}} = 1$" (blue) and $\theta_{\mathrm{HPBW}} = 45$" (orange). It is assumed that the beam center and the source center coincide at $(0, 0)$ and the background intensity $T_{\mathrm{bg}} = 2.7\,\mathrm{K}$ was subtracted from the spectrum. As can be seen, for a very narrow ("pencil") beam, the modeled antenna temperature coincides with the emergent spectral line intensity for the central LOS (Fig. 3.6), which is shown as red dashed line. However, for a larger beam, the modeled antenna temperature becomes significantly lower due to the decreasing emergent intensity with increasing distance from the (plane) source center.

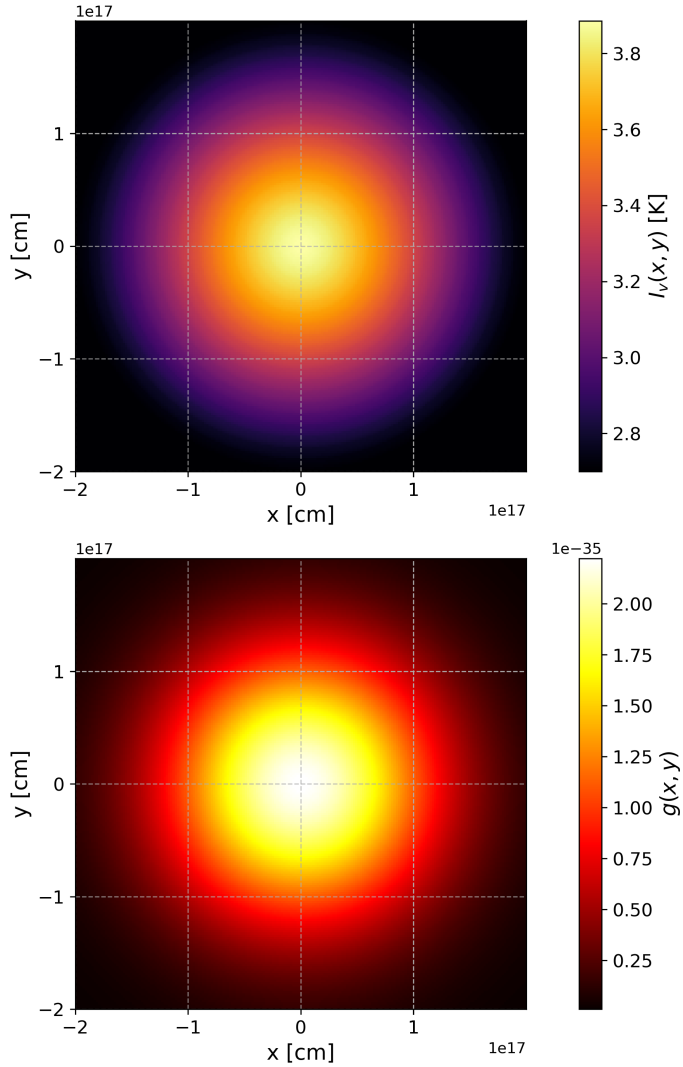

Figure 3.9: Top: emergent spectral intensity at velocity $v = 0\,\mathrm{km\,s^{-1}}$ for the numeric example of a static cloud with $\alpha_0 = 10^{-18}\,\mathrm{cm^{-1}}$. **Bottom:** Gaussian beam shape function calculated from Eq. (3.33) for a beam size of $\theta_{\mathrm{HPBW}} = 45$” and a source distance of 300 pc.

The two modeled antenna temperatures can be used to demonstrate the calculation of the beam-filling factor via Eq. (2.111). First, an estimate of the source size is derived via Eq. (2.115), giving $\theta_S = 49$". For $\theta_\mathrm{B} = 45$", the beam filling factor is $f_\mathrm{Gauss} = 0.54$. The corrected antenna temperature corresponding to $\theta_\mathrm{B} = 45$" is then $T_\mathrm{A}/f_\mathrm{Gauss} = 1.19\,\mathrm{K}$, which is equal to T_A corresponding to $\theta_\mathrm{B} = 1$" (or $I_\nu(0,0)$).

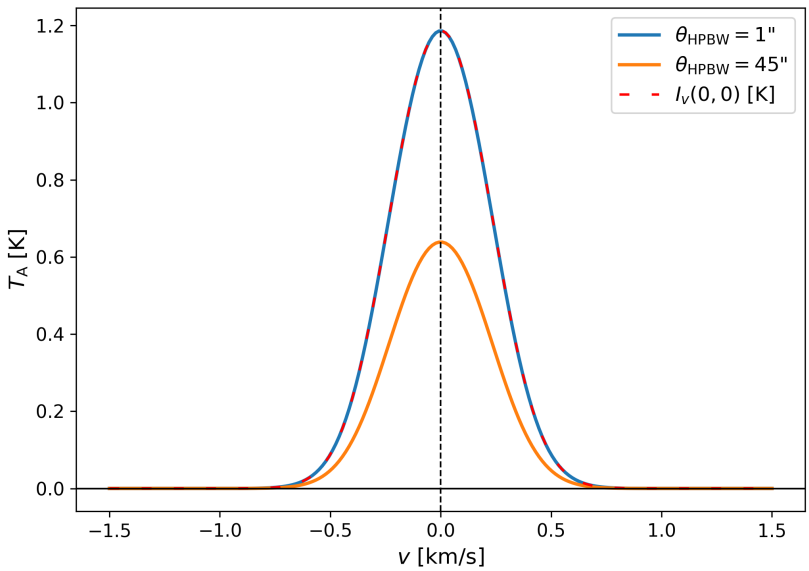

Figure 3.10: Beam convolved (average) emergent intensity $T_\mathrm{A} = \langle I_v \rangle$ calculated from Eq. (3.37), assuming $\theta_\mathrm{HPBW} = 1$" (blue line) and $\theta_\mathrm{HPBW} = 45$" (orange line). The red dashed line shows the emergent intensity for the central LOS as shown in Fig. 3.6 for the static case. The background intensity $T_\mathrm{bg} = 2.7\,\mathrm{K}$ was subtracted from the spectrum.

It is important to note that, when observing a source with a telescope beam, not only the intensity becomes an average over the beam, but also the optical depth. The beam average optical depth τ_v^beam is calculated as

$$\tau_v^\mathrm{beam} = \sum \tau_v(x,y)\, g(x,y)\, \Delta r\,, \tag{3.39}$$

and has qualitatively the same features as the beam average intensity.

CHAPTER 4

Molecular Column Density Calculation

When pointing a radio telescope towards a cold molecular cloud source, it gathers photons emitted by gas phase molecules during transitions between their rotational energy levels. The area from which the photons are gathered is constrained by the telescope beam size, which depends on the dish size of the telescope and the observing frequency. Furthermore, the depth up to which photons are gathered is limited by the optical depth of the gas. Then, the number of received photons in the frequency interval that defines a spectral line produces a certain (beam average) integrated line intensity, which is directly proportional to the number of emitting molecules within the limiting area of the beam on the sky. Hence, measured integrated line intensities can be used to infer the number of molecules within the "column" defined by the beam of a telescope. This number is therefore called the column density of a molecule. This chapter presents the tools for the calculation of molecular column densities from measured spectral line intensities. Section 4.1 covers the basic definitions and discusses the case of having LTE conditions. Then, section 4.2 discusses the influence of optical depth and section 4.3 introduces the population diagram method. Lastly, section 4.4 discusses the column density calculation for the case of non-LTE conditions.

4.1 Basic Definitions and LTE Conditions

If $n(\mathrm{mol})$ is the number volume density of molecule "mol", and considering a path with length L through a cloud, the basic definition of molecular column density is

$$N(\mathrm{mol}) = \int_0^L n(\mathrm{mol})\,\mathrm{d}z\,. \tag{4.1}$$

However, there is no way to directly probe the volume density of a molecule in a cloud without an additional assumption about the cloud geometry. Instead, the relation between spectral line intensity and the underlying level population is used to calculate the column density of a molecule. The equation for that is derived from the equations presented in sections 2.3 and 2.4. The upper level column density N_u has been already introduced as a parameter in Eq. (2.79) for the optical depth of a spectral line. It essentially gives the number of molecules (per unit sky area) in an upper energy level along a line of sight through the cloud. Re-arranging Eq. (2.79) for N_u gives

$$N_\mathrm{u} = \frac{8\pi\nu^2}{c^2 A_\mathrm{ul}} \left[\exp\left(\frac{h\nu}{k_\mathrm{B}T_\mathrm{ex}}\right) - 1\right]^{-1} \int \tau_\nu\,\mathrm{d}\nu\,. \tag{4.2}$$

Assuming statistical equilibrium, the upper level column density of a molecule is related to its total column density N_tot via the rotational partition function Q_rot as

$$\frac{N_\mathrm{u}}{N_\mathrm{tot}} = \frac{g_\mathrm{u}}{Q_\mathrm{rot}} \exp\left(-\frac{E_\mathrm{u}}{k_\mathrm{B}T_\mathrm{ex}}\right) \tag{4.3}$$

(see Eqs. 2.46 and 2.47). Inserting Eq. (4.2) into Eq. (4.3) then gives

$$N_\mathrm{tot} = \frac{8\pi\nu^2}{c^2 A_\mathrm{ul}} \frac{Q_\mathrm{rot}}{g_\mathrm{u}} \exp\left(\frac{E_\mathrm{u}}{k_\mathrm{B}T_\mathrm{ex}}\right) \left[\exp\left(\frac{h\nu}{k_\mathrm{B}T_\mathrm{ex}}\right) - 1\right]^{-1} \int \tau_\nu\,\mathrm{d}\nu\,. \tag{4.4}$$

If the excitation of a molecule is governed by LTE conditions, the complete level population is constrained by a single excitation temperature T_ex, which, in the high density limit, can be assumed to be the gas kinetic temperature T_k of the source (section 2.3). Therefore, if an estimate of T_k exists for a cloud, calculating the column density of a molecule becomes trivial for LTE conditions. Furthermore, in case of LTE conditions, the calculated column

density will be the same regardless of the observed spectral line. This is in strong contrast to the case of non-LTE conditions, where the population of different level pairs is characterized by different values of $T_{\rm ex}$. In this case, wrongly assuming the same $T_{\rm ex} = T_{\rm k}$ for different lines therefore gives different values of $N_{\rm tot}$. It follows that the column density calculation for molecules governed by non-LTE conditions is non-trivial and requires the use of non-LTE radiative transfer models (section 4.4).

4.2 Influence of Optical Depth

As a first order approximation, it can often be assumed that the optical depth of a molecular transition is much smaller than unity, especially when observing complex molecules where the emission is spread over many spectral lines. This defines the so-called optically thin approximation. Essentially, if $\tau_\nu \ll 1$, and if LTE conditions are assumed, the expression for the measured antenna temperature towards a source (Eq. 3.7) can be written as

$$T_{\rm A}(\nu) = f\left[J_\nu(T_{\rm ex}) - J_\nu(T_{\rm bg})\right]\tau_\nu\,. \tag{4.5}$$

Inserting this into the expression for the total column density of a molecule (Eq. 4.4), yields

$$N_{\rm tot}^{\rm thin} = \frac{8\pi\nu^2}{c^2 A_{\rm ul}}\frac{Q_{\rm rot}}{g_{\rm u}}\exp\left(\frac{E_{\rm u}}{k_{\rm B}T_{\rm ex}}\right)\left[\exp\left(\frac{h\nu}{k_{\rm B}T_{\rm ex}}\right)-1\right]^{-1} \frac{1}{f\left[J_\nu(T_{\rm ex}) - J_\nu(T_{\rm bg})\right]}\int T_{\rm A}(\nu)\,{\rm d}\nu\,, \tag{4.6}$$

where $\int T_{\rm A}(\nu)\,{\rm d}\nu$ is the integrated intensity, which was already defined in Eq. (3.38). It is allowed to remove the term including $J_\nu(T)$ from the integral, because it does not vary substantially across the frequency width of a typical spectral line (Mangum and Shirley, 2015). Often, $J_\nu(T_{\rm ex}) \gg J_\nu(T_{\rm bg})$, in which case $J_\nu(T_{\rm bg})$ can be neglected. However, in cold sources where $T_{\rm ex}$ is typically not much higher than $T_{\rm bg}$, $J_\nu(T_{\rm bg})$ must be considered. Essentially, as $T_{\rm A}(\nu)$ is an average over the antenna beam (sections 2.6 and 2.4), the derived column density is also an average over the antenna beam.

In optically thin conditions ($\tau_\nu \ll 1$), a telescope pointed at a molecular cloud source will gather photons from all depths into the source. However, in optically thick conditions ($\tau_\nu \gg 1$), photons from deep source layers can get absorbed by molecules in the foreground (section 3.3), such that the number of photons that leave the source, and is counted by the telescope, is lower than the number of actually emitted photons. It follows that the column density derived from an optically thick line with the optically thin approximation underestimates the true column density of a molecule. One way to take this into account is to use an estimate of the line optical depth and to apply the correction factor

$$C_\tau = \frac{\tau_\nu}{1 - \mathrm{e}^{-\tau_\nu}} = \frac{1}{\beta_{\mathrm{LVG}}} \,. \tag{4.7}$$

The total column density obtained from an optically thick line is then given as

$$N_{\mathrm{tot}} = C_\tau N_{\mathrm{tot}}^{\mathrm{thin}} \tag{4.8}$$

(Goldsmith and Langer, 1999; Mangum and Shirley, 2015). As can be seen, the correction factor is the inverse of the photon escape probability β for the LVG model (Eq. 3.19). This basically means that optically thin and optically thick conditions directly refer to high respective low photon escape probabilities, as $\beta_{\mathrm{LVG}} \to 1$ if $\tau_\nu \ll 1$, but $\beta_{\mathrm{LVG}} \to 0$ if $\tau_\nu \gg 1$.

One way to estimate the optical depth of a spectral line is by using the so-called double-isotopologue method, in which the measured line intensities of two isotopologues with a well established abundance ratio are required (Yamamoto, 2017). That is, having isotopologues iso_1 and iso_2 with isotopic ratio R_{iso} and measured integrated intensities, the optical depth can be derived from the following equation:

$$\frac{\int T_{\mathrm{A}}(\mathrm{iso}_1)\,\mathrm{d}v}{\int T_{\mathrm{A}}(\mathrm{iso}_2)\,\mathrm{d}v} = \frac{1 - \mathrm{e}^{-\tau_\nu}}{1 - \mathrm{e}^{-\tau_\nu / R_{\mathrm{iso}}}} \,. \tag{4.9}$$

This method was used in paper A to derive the optical depth of the H_2CO(1-0) line. Another way is to solve Eq. (4.4) for the optical depth, starting from an estimated initial value $N_{\mathrm{tot}} = N_{\mathrm{tot}}^{\mathrm{thin}}$, and then using Eqs. (4.7) and (4.8) to iteratively update the value of N_{tot} until convergence. This method was used in paper B to estimate the optical depth of observed $C^{18}O$(1-0) lines. It

is also possible to use non-LTE radiative transfer modeling to estimate the optical depth of a line (section 3.4). This was done in paper C to derive the optical depth of CS and SO lines.

4.3 The Population Diagram Method

Another way to derive the total column density of a molecule without the need to assume an excitation temperature is by using the so-called population diagram method (Goldsmith and Langer, 1999; Yamamoto, 2017). To apply that method, the measured intensities of several spectral lines of the same molecule are required, from a range of upper level energies as wide as possible. The basis of this method is that, at LTE conditions, the relative intensities of a set of spectral lines are constrained by the underlying level population. The corresponding upper level column densities of the spectral lines can be calculated as

$$N_{\rm u} = f\frac{8\pi k_{\rm B}\nu^2}{hc^3 A_{\rm ul}}\left(\frac{1-{\rm e}^{-\tau_\nu}}{\tau_\nu}\right)\int T_{\rm A}(\nu)\,{\rm d}\nu \tag{4.10}$$

(Goldsmith and Langer, 1999). If the emission fills the beam (i.e., if $f = 1$), and if the considered line is optically thin (i.e., if $\tau_\nu \ll 1$), the above expression becomes

$$N_{\rm u}^{\rm thin} = \frac{8\pi k_{\rm B}\nu^2}{hc^3 A_{\rm ul}}\int T_{\rm A}(\nu)\,{\rm d}\nu\,. \tag{4.11}$$

If the line is optically thick, it has to be treated as discussed before for the case of total column density (Goldsmith and Langer, 1999). The total column density is related to the upper state column density by Eq. (4.3), which can be rearranged to give

$$\ln\left(\frac{N_{\rm u}}{g_{\rm u}}\right) = \ln\left(\frac{N_{\rm tot}}{Q_{\rm rot}}\right) - \frac{E_{\rm u}}{T_{\rm ex}}\,. \tag{4.12}$$

Here it is assumed that $E_{\rm u}$ is given in units of Kelvin as compared to Eq. (4.3), where $k_{\rm B}$ is included. The above equation describes a straight line in the $E_{\rm u}$ – $\ln(N_{\rm u}/g_{\rm u})$ – plane, which defines a so-called population diagram (or rotation diagram). The y-intercept of this line is $\ln(N_{\rm tot}/Q_{\rm rot})$, while the slope of the line is $-1/T_{\rm ex}$ (Goldsmith and Langer, 1999; Mangum and Shirley, 2015). If integrated intensities for several lines of the same molecule are available, they

can be used to derive upper state column densities, which can then be plotted in a population diagram (see example in Fig. 4.1).

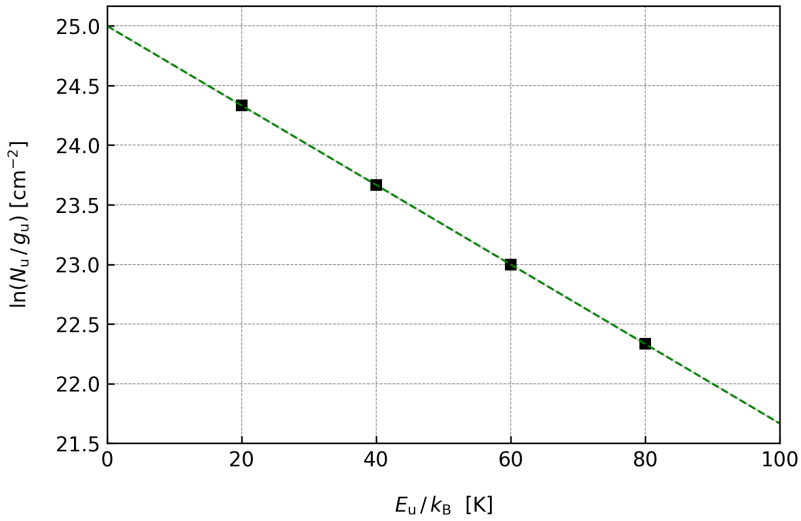

Figure 4.1: Hypothetical population diagram for perfect LTE conditions. The four data points are assumed to be calculated from Eq. (4.11) for spectral lines resulting from transitions $u \rightarrow l$ with upper level energies E_u/k_B of 20 K, 40 K, 60 K, and 80 K.

At perfect LTE conditions, the data points in a population diagram will fall on a straight line because the complete energy level population is constrained by the same excitation temperature T_{ex} (sometimes called rotation temperature in this context). Thereby, the line fit is best constrained if the upper levels of the observed lines have a large separation in E_u. Then, the value of T_{ex} can be derived from the slope of the line and, assuming LTE conditions in the high-density limit, can be used to estimate the gas kinetic temperature $T_k = T_{ex}$. Furthermore, the total column density of the considered molecule can be directly derived from the y-intercept. In non-LTE conditions, the data points in a population diagram will deviate from a straight line because T_{ex} is not the same for the different considered spectral lines. The population diagram method is therefore a useful tool to estimate whether or not the ex-

citation of a molecule is governed by LTE conditions. It was used in papers A, B, and C to check the validity of the LTE assumption and to derive some of the molecular column densities.

4.4 Non-LTE Conditions

As was already mentioned in section 4.1, using Eq. (4.4) to calculate the column density of a molecule whose excitation is governed by non-LTE conditions is not trivial, because $T_{\rm ex}$ differs for different spectral lines and is, generally, largely unknown. That is, the approximation that $T_{\rm ex} = T_{\rm k}$ for all spectral lines does not apply in non-LTE conditions. In extreme cases of having masing lines, the excitation temperature can even be negative. Therefore, to derive the column density for a molecule in non-LTE conditions, it is necessary to use non-LTE radiative transfer models to simulate spectral line intensities, assuming a set of physical parameters, including molecular abundance $X(\rm mol) = n(\rm mol)/n(H_2$. Then, a statistical analysis is required to derive the parameters that best reproduce some measured line intensities. Eventually, the best fit value of $X(\rm mol)$ can be used to calculate a beam weighted (convolved) column density estimate. Examples in the following discussion will be based on the `ALI` model, which was introduced in section 3.2. However, the basic principles are independent of the used non-LTE model.

Statistical analysis

Choosing the frequentist approach, a χ^2 analysis can be used to derive the best-fit value of molecule abundance $X(\rm mol)$[1]. For that, a large number of non-LTE radiative transfer models must be run for varying values of $X(\rm mol)$. It is also possible to vary other parameters such as kinetic temperature or H_2 density, simultaneously. Each model produces a separate set of integrated line intensities $[I_{\rm mod,1}, I_{\rm mod,2}, \ldots, I_{\rm mod,}N]$ for N considered spectral lines. Then, for each model, a χ^2 value is calculated as

$$\chi^2 = \sum_i^N \frac{(I_{{\rm mod},i} - I_{{\rm obs},i})^2}{\sigma^2_{{\rm obs},i}}\,, \tag{4.13}$$

[1]It is also possible to use another statistical framework like Bayesian inference.

where $I_{\mathrm{obs},i}$ is the observed integrated line intensity of the ith spectral line and $\sigma_{\mathrm{obs},i}$ is the corresponding standard deviation. It is common to work with the reduced χ^2 value χ^2_{red}, which is obtained by dividing the χ^2 value by the $N - p$ degrees of freedom of the model, i.e.,

$$\chi^2_{\mathrm{red}} = \frac{\chi^2}{(N-p)}\,, \tag{4.14}$$

where N is still the number of modeled spectral lines and p is the number of simultaneously varied model parameters. In general, the difference between observed and modeled data is minimized at the minimum χ^2_{red} value $\min\left(\chi^2_{\mathrm{red}}\right)$, and the best-fit model parameters are given by the corresponding model. Obviously, a perfect fit between modeled and observed data is obtained when $\chi^2 = \chi^2_{\mathrm{red}} = 0$. However, a perfect fit is not the criterion for a good model, because there are always uncertainties related to a measurement, and a good model should deviate from the data by about as much as the uncertainties. This conditions is fulfilled when $\chi^2_{\mathrm{red}} \approx 1$. A value of $\chi^2_{\mathrm{red}} \gg 1$ might indicate underfitting (too simple model) or underestimated uncertainties, while $\chi^2_{\mathrm{red}} \ll 1$ might indicate overfitting (too flexible model) or overestimated uncertainties. Those are important points to consider when interpreting the obtained χ^2_{red} minimum.

Uncertainties related to the model parameters are generally determined as follows. Simultaneously varying three parameters such as $X(\mathrm{mol})$, $n(\mathrm{H_2})$, and T_{k} spans a 3D parameter space, where each point has a particular χ^2_{red} value. Thereby, the best-fit model defines one point in the parameter space, corresponding to $\min\left(\chi^2_{\mathrm{red}}\right)$. A 3D uncertainty ellipsoid (or contour) can be defined around this point, whose shape, orientation, and extension embody information about the relation between parameters, as well as the level of confidence with which we can state that the value of one parameter lies in a certain interval. The uncertainty contour is generally defined as the set of points

$$\sigma_{\mathrm{cont}} = \left\{\min\left(\chi^2_{\mathrm{red}}\right) + \alpha_p\right\}, \tag{4.15}$$

where α_p is a number depending on the desired level of confidence and the number of model parameters p; for example, for the 1-σ contour (68 % confidence) and for $p = 3$, $\alpha_p = 3.5$ (Lampton et al., 1976). If σ_1^2, σ_2^2, and σ_3^2 are the variances of the three parameters, the simplest case is the special case

of having a sphere centered at the point with $\chi^2_{\min}$. In this case, the three variances are equal ($\sigma_1^2 = \sigma_2^2 = \sigma_3^2$) and the corresponding covariance matrix is simply

$$\mathrm{Cov} = \begin{pmatrix} \sigma_1^2 & 0 & 0 \\ 0 & \sigma_1^2 & 0 \\ 0 & 0 & \sigma_1^2 \end{pmatrix}, \tag{4.16}$$

meaning that the three parameters have equal uncertainties and are uncorrelated, i.e., each parameter can be varied independently of the other parameters without significantly changing the modeling outcome. If all three variances are different ($\sigma_1^2 \neq \sigma_2^2 \neq \sigma_3^2$), the contour takes the shape of a triaxial ellipsoid. If the major axes of this ellipsoid are aligned with the axes of the underlying 3D parameter space, we have the (still diagonal) covariance matrix

$$\mathrm{Cov} = \begin{pmatrix} \sigma_1^2 & 0 & 0 \\ 0 & \sigma_2^2 & 0 \\ 0 & 0 & \sigma_3^2 \end{pmatrix}. \tag{4.17}$$

In this case, the parameter uncertainties have different magnitudes, but the parameters are still uncorrelated. Lastly, in the general case of correlated parameters with different uncertainties, the covariance matrix becomes

$$\mathrm{Cov} = \begin{pmatrix} \sigma_1^2 & c_{12} & c_{13} \\ c_{12} & \sigma_2^2 & c_{23} \\ c_{13} & c_{23} & \sigma_3^2 \end{pmatrix}, \tag{4.18}$$

corresponding to a tilted triaxial ellipsoid, i.e., the major axes of the ellipsoid are not aligned with the axes of the underlying 3D parameter space. In the above matrix, c_{ij} are the covariances for parameter pairs i and j, providing information about parameter correlations by means of the correlation coefficients

$$\rho_{ij} = \frac{c_{ij}}{\sigma_i \sigma_j}, \tag{4.19}$$

where σ_i and σ_j are the standard deviations (square root of the variances) of parameters i and j. Determining the correlation coefficients is equivalent to normalizing the covariance matrix by $\sigma_i \sigma_j$, i.e., constructing the correlation

matrix

$$\mathrm{Corr} = \begin{pmatrix} 1 & \rho_{12} & \rho_{13} \\ \rho_{12} & 1 & \rho_{23} \\ \rho_{13} & \rho_{23} & 1 \end{pmatrix} . \tag{4.20}$$

In general, $\rho_{ij} \in [-1, 1]$, and the cases $\rho_{ij} = 1$ and $\rho_{ij} = -1$ indicate a perfect positive/negative correlation between parameters i and j, respectively, while $\rho_{ij} = 0$ indicates no correlation. The uncertainties of the parameters are furthermore given by the six points on the contour that maximize the orthogonal distance to the three axes of the underlying coordinate system.

Of course, in practice, the model outcomes do not always allow the construction of a closed contour around a single χ^2_{red} minimum. Furthermore, running non-LTE radiative transfer models can be computationally expensive and time consuming. Therefore, the sampled set of points in the 3D parameter space can be relatively coarse, in which case it becomes difficult to construct the full uncertainty ellipsoid, which is then only sampled by elliptic slices. One common way to construct these slices is by varying two parameters, p_1 and p_2, at a time, while the third one, p_3, is fixed. Then, considering the same grid of values for p_1 and p_2, p_3 is varied to another value. This method has been used to derive the parameter uncertainties for the non-LTE models in papers B and C.

Numeric example: constructing the $1\,\sigma$ ellipsoid

The following example summarizes attempts to construct the full $1\,\sigma$ uncertainty contour from a sample of slices through a 3D parameter space. Even though not used in any of the appended papers, the method works well as an illustration of the mentioned concepts and has the potential to speed up the uncertainty analysis in future work.

The example is based on non-LTE modeling results with `ALI` for the column density determination of the $^{12}C^{32}S$, $^{12}C^{34}S$, and $^{13}C^{32}S$ isotopologues towards the methanol hotspot in B5 (see paper C); for simplicity, the isotopologues will be denoted CS, $C^{34}S$, and ^{13}CS. The χ^2_{red} statistic utilized here is the same as in the paper, which can be checked for details about the modeling process. Most basically, the statistic is produced by comparing measured integrated line intensities of a number of CS, $C^{34}S$, and ^{13}CS lines to modeled

line intensities[2], determined for constant values of $n(\mathrm{H_2}) = 1.6 \times 10^4\,\mathrm{cm^{-3}}$ and $T_\mathrm{k} = 20\,\mathrm{K}$. Grids of $N(\mathrm{C^{34}S}) - N(^{13}\mathrm{CS})$ are sampled at constant values of $N(\mathrm{CS})$. Note that the column density used in the modeling process is related to the abundance as $N(\mathrm{mol}) = 2/3\,R\,X(\mathrm{mol})$, where R is the assumed source radius (see also text on beam convolution below). Using a logarithmic scale, the considered value ranges are $\log[N(\mathrm{CS})/\mathrm{cm^{-2}}] \in [13.32, 13.48]$, $\log[N(\mathrm{C^{34}S})/\mathrm{cm^{-2}}] \in [12.2, 12.7]$ and $\log[N(^{13}\mathrm{CS})/\mathrm{cm^{-2}}] \in [11.5, 12.0]$. Furthermore, a step size of $\log[\Delta N/\mathrm{cm^{-2}}] = 0.025$ is used for $N(\mathrm{C^{34}S})$ and $N(^{13}\mathrm{CS})$. For $N(\mathrm{CS})$, the used step size is $\log[\Delta N/\mathrm{cm^{-2}}] = 0.02$, which is reduced to 0.01 close to the uncertainty limits.

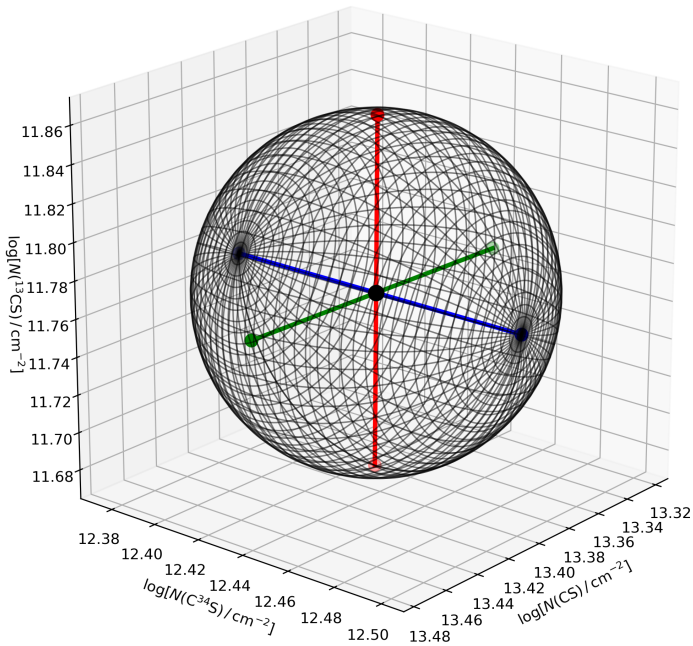

Figure 4.2: Full $1\,\sigma$ uncertainty ellipsoid for a set of `ALI` models in the $N(\mathrm{CS}) - N(\mathrm{C^{34}S}) - N(^{13}\mathrm{CS})$ parameter space. The black dot marks the ellipsoid center (best fit), while the red, green, and blue points and connecting lines correspond to the parameter uncertainties (see text for details).

[2]Line intensities of $\mathrm{C^{33}S}$ are considered as well, but this has no major effect on the final results.

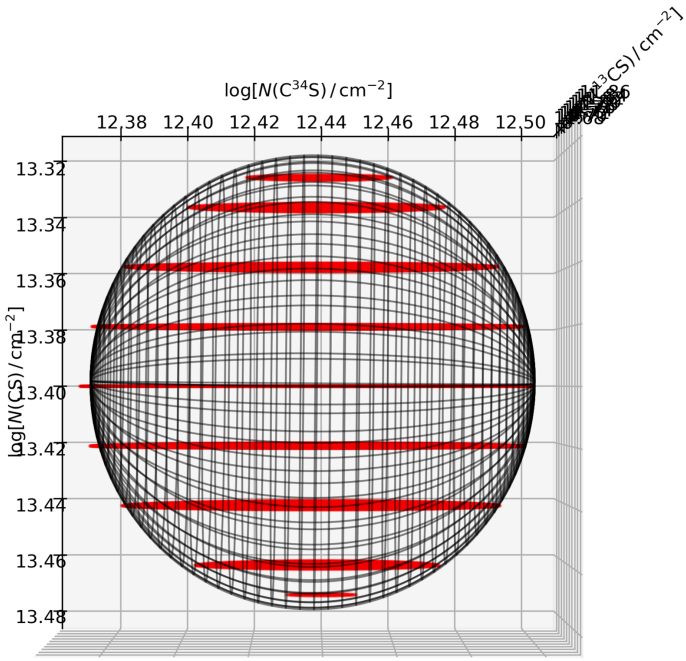

Figure 4.3: Full $1\,\sigma$ uncertainty ellipsoid for a set of `ALI` models in the $N(\mathrm{CS})-N(\mathrm{C}^{34}\mathrm{S})-N(^{13}\mathrm{CS})$ parameter space, shown with $N(^{13}\mathrm{CS})$ as z-axis. The red areas mark all the points that lie inside the elliptic $1\,\sigma$ contours at different $N(\mathrm{CS})$.

Fig. 4.2 shows the full $1\,\sigma$ uncertainty contour, determined from the χ^2_{red} statistic. Also shown are the six points and the connecting lines that maximize the separation of surface points along the three axes of the ellipsoid. The utilized model data are all the 3D points that lie inside the elliptic $1\,\sigma$ contours in the different sampled $N(\mathrm{C}^{34}\mathrm{S})-N(^{13}\mathrm{CS})$ planes (and at a certain $N(\mathrm{CS})$). These points are marked by the red areas in Fig. 4.3, clearly showing the slicing at different values of $N(\mathrm{CS})$. Fig. 4.4 further shows the top view onto the slices and the ellipsoid, with $N(\mathrm{CS})$ as z-axis. To determine the full $1\,\sigma$ contour, all N data points that lie inside the elliptic $1\,\sigma$ contours are stored in a $N \times 3$ matrix $\mathbf{D}$ with columns $N(\mathrm{CS})$, $N(\mathrm{C}^{34}\mathrm{S})$, and $N(^{13}\mathrm{CS})$. Then, the statistical spread of the data is determined via the covariance matrix $\mathrm{Cov}(\mathbf{D})$

(Eq. 4.18; determined in `Python` using the `numpy.cov` function). Calculating the correlation matrix via Eqs. (4.19) and (4.20) yields

$$\mathrm{Corr}(\mathbf{D}) = \begin{pmatrix} 1 & -0.003 & -0.005 \\ -0.003 & 1 & -0.003 \\ -0.005 & -0.003 & 1 \end{pmatrix}, \tag{4.21}$$

which is showing that the three considered parameters are essentially fully uncorrelated. This is the case because changing the column density of one isotopologue has no effect on the line intensities of the other isotopologues, leading to a very slow change in χ^2_{red} when gradually changing only, e.g., $N(^{13}\mathrm{CS})$.

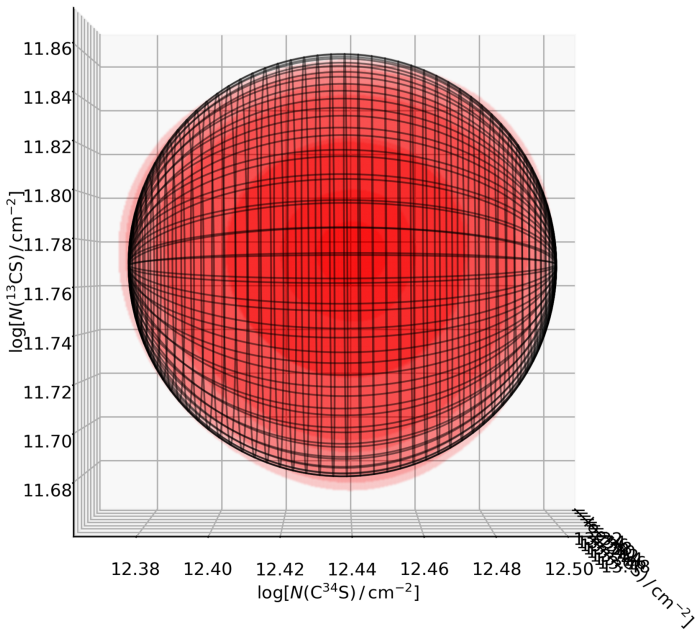

Figure 4.4: Same as Fig. 4.3 but with $N(\mathrm{CS})$ as z-axis.

Eventually, the ellipsoid shown in Figs. 4.2 – 4.4 is constructed from the covariance matrix $\mathrm{Cov}(\mathbf{D})$. Thereby, the orientation and extension of the el-

lipsoid are determined by the eigenvectors and eigenvalues (diagonal elements) of $\mathrm{Cov}(\mathbf{D})$, respectively. Specifically, if the eigenvalues are denoted λ_i, it can be shown that, for an ellipsoid with

$$\frac{p_1^2}{r_1^2} + \frac{p_2^2}{r_2^2} + \frac{p_3^2}{r_3^2} \leq 1\,, \tag{4.22}$$

the maximum extension along the ith axis is $r_i = \sqrt{5\lambda_i}$. The factor of five comes from the mean-square distance of points filling the ellipsoid. That is, considering the special case of sphere with radius R and volume V, the mean-square distance of points from the center is

$$\langle r^2 \rangle = \frac{1}{V} \int_0^R r^2 \,\mathrm{d}V = \frac{3}{5} R^2\,. \tag{4.23}$$

Then, for a sphere with

$$\frac{p_1^2}{R^2} + \frac{p_2^2}{R^2} + \frac{p_3^2}{R^2} \leq 1\,, \tag{4.24}$$

it is found that $3\langle p_i^2 \rangle = \langle r^2 \rangle = 3/5\, R^2$, from which it follows that

$$\langle p_i^2 \rangle = \frac{1}{5} R^2\,. \tag{4.25}$$

In general, the eigenvalues of $\mathrm{Cov}(\mathbf{D})$ are the variances of the parameters p_i, i.e.,

$$\lambda_i = \mathrm{Var}(p_i) = \langle p_i^2 \rangle - \langle p_i \rangle^2\,. \tag{4.26}$$

For a sphere centered at $\langle r \rangle = (0, 0, 0)$, $\langle p_i \rangle = 0$, and it follows that the radius of the sphere is related to the eigenvalues as

$$R = \sqrt{5\lambda_i}\,. \tag{4.27}$$

It can be shown that the same holds if the sphere is centered at an arbitrary center $\langle r \rangle$. Furthermore, extending to the general case of an ellipsoid yields $r_i = \sqrt{5\lambda_i}$.

As was discussed above, the best fit lies at the center of the ellipsoid, while the uncertainties of the three parameters are given by the six points on the

surface of the ellipsoid that maximize the orthogonal distance to the three axes. For the current example, those points and the intersecting lines are shown in Fig. 4.2. As can be seen, in case of uncorrelated parameters (an axes-aligned ellipsoid), the uncertainties are actually determined by the maximum extension of the ellipsoid along the three axes, i.e., by $r_i = \sqrt{5\lambda_i}$. It is found that

$$\begin{aligned} \log[N(\mathrm{CS})/\mathrm{cm}^{-2}] &= 13.40 \pm 0.08\,, \\ \log[N(\mathrm{C}^{34}\mathrm{S})/\mathrm{cm}^{-2}] &= 12.44 \pm 0.06\,, \\ \log[N(^{13}\mathrm{CS})/\mathrm{cm}^{-2}] &= 11.77 \pm 0.09\,, \end{aligned}$$

which translates to

$$\begin{aligned} N(\mathrm{CS}) &= 2.5(+0.5, -0.4) \times 10^{13}\,\mathrm{cm}^{-2}\,, \\ N(\mathrm{C}^{34}\mathrm{S}) &= 2.7(+0.4, -0.4) \times 10^{12}\,\mathrm{cm}^{-2}\,, \\ N(^{13}\mathrm{CS}) &= 5.9(+1.4, -1.1) \times 10^{11}\,\mathrm{cm}^{-2}\,. \end{aligned}$$

For $N(\mathrm{CS})$, those values are the same as the estimates in paper C, and for $N(\mathrm{C}^{34}\mathrm{S})$ and $N(^{13}\mathrm{CS})$ they are very close (not more than 0.1 difference). The method used in the paper to estimate the uncertainties requires much more manual steps and is susceptible to error. Contrary to that, the method described here only requires storing calculated χ^2_{red} values in a table format for the sampled slices, which are then used to construct the full uncertainty ellipsoid.

Beam Convolution

The abundance $X(\mathrm{mol}) = n(\mathrm{mol})/n(\mathrm{H_2})$ and the column density $N(\mathrm{mol})$ of a molecule are related to each other through Eq. (4.1). Considering the central path through a spherical cloud with radius R gives

$$N(\mathrm{mol}) = \int_{-R}^{R} n(\mathrm{H_2})\, X(\mathrm{mol})\, \mathrm{d}z\,. \tag{4.28}$$

However, this equation is for a single line of sight (LOS) through the model cloud, but the column density is generally an average over all LOSs covered by a telescope beam. Considering all LOSs through the cloud, and assum-

ing constant values of $n(\mathrm{H_2})$ and $X(\mathrm{mol})$, the source average column density N_{source} is given by

$$N_{\mathrm{source}}(\mathrm{mol}) = \frac{4}{3} R\, n(\mathrm{H_2})\, X(\mathrm{mol}). \tag{4.29}$$

This estimate is used in most of the `ALI` models in papers B and C, and in the numeric example above. In general, the modeling can be done either in abundance space or in column density space (using one of the two equations above), but eventually, the beam convolved column density must be calculated from the abundance.

Following the numerical shell model introduced in section 3.3, and assuming a Gaussian beam shape function $g(x, y)$ described by Eq. (3.33), the beam convolved column density $N_{\mathrm{beam}}(\mathrm{mol})$ is calculated as

$$N_{\mathrm{beam}}(\mathrm{mol}) = \sum N(x, y)\, g(x, y)\, \Delta x \Delta y\,, \tag{4.30}$$

where $N(x, y)$ is the column density for the LOS at plane position (x, y), calculated as

$$N(x, y) = \sum_i n_i(\mathrm{H_2})\, X_i(\mathrm{mol})\, L_i(x, y)\,, \tag{4.31}$$

where $L(x, y)$ is the chord length through the ith shell (Eq. 3.22), characterized by specific values of $\mathrm{H_2}$ density and molecular abundance. Assuming constant values of $n(\mathrm{H_2})$ and $X(\mathrm{mol})$, Eq. (4.30) simplifies to

$$N_{\mathrm{beam}}(\mathrm{mol}) = n(\mathrm{H_2})\, X(\mathrm{mol}) \sum g(x, y)\, L(x, y)\, \Delta x \Delta y\,. \tag{4.32}$$

Using this numeric beam convolution method, it is straightforward to calculate column density estimates for off-center positions by shifting the beam center away from the source center.

CHAPTER 5

Summary of Appended Papers

This chapter provides a brief summary of the papers this thesis is based on, i.e., paper A, paper B, and paper C, which can be found in the appendix. The three papers investigate different aspects of the gas phase molecular content and chemistry observed towards the so-called methanol hotspot in the Barnard 5 dark cloud. Therefore, this chapter starts with a short separate section on the source region and its general characteristics.

5.1 The Barnard 5 Methanol Hotspot

The three papers appended to this thesis all focus on the same source region, i.e., the so-called methanol hotspot in the Barnard 5 (B5) dark cloud. B5 is part of a catalog of 349 dark clouds, summarized in Barnard et al. (1927). It is located in the Perseus molecular cloud complex at a distance of approximately 300 pc (Zucker et al., 2018). The thesis front cover shows part of the cloud complex, with B5 marked with a white box. Fig. 5.1 further shows the H_2 column density map for B5, created from HGBS[1] (Herschel Gould Belt survey) data. As can be seen, B5 has an elongated structure extending over approximately 1.2 pc from north to south and is about 0.4 pc wide at its broadest extension. It hosts the Class I protostar IRS1 in the southern part (black cross in Fig. 5.1). Observations have further shown that the cloud contains filamentary structures and some potentially prestellar cores (Pineda et al., 2011, 2015; Schmiedeke et al., 2021).

The methanol hotspot (hereafter B5-Hotspot) is the position of maximum methanol (CH_3OH) emission in B5, located in the northern part of the cloud (black cross in Fig. 5.1). Specifically, it is located in between two dense cores, i.e., East 189 and East 286, which are not gravitationally bound and not expected to form stars in the future (Sadavoy, 2013). B5-Hotspot was first described in Wirström et al. (2014), who also report the detection of gas phase water towards this position. The only other cold dark cloud source with a detection of gas phase water is the prototypical prestellar core L1544 (Caselli et al., 2012). The kinetic temperature and density at B5-Hotspot are about 10 –20 K and 2×10^4 cm^{-3} (Taquet et al., 2017; Carl et al., 2026a,b). The high abundances of gas phase methanol and water at B5-Hotspot suggest a very efficient release of ice species from dust grains, especially as methanol is thought to be almost exclusively formed by grain surface reactions at low temperatures (see section 1.2; Eq. 1.27). Further evidence for the efficient ice mantle desorption comes from the detection of gas phase complex organic molecules (COMs), i.e., acetaldehyde (CH_3CHO), methyl formate (CH_3OCHO), and dimethyl ether (CH_3OCH_3), by Taquet et al. (2017). However, there are also feasible gas phase formation routes for some of those molecules (e.g., Vasyunin et al., 2017).

[1] http://www.herschel.fr/cea/gouldbelt/en/index.php.

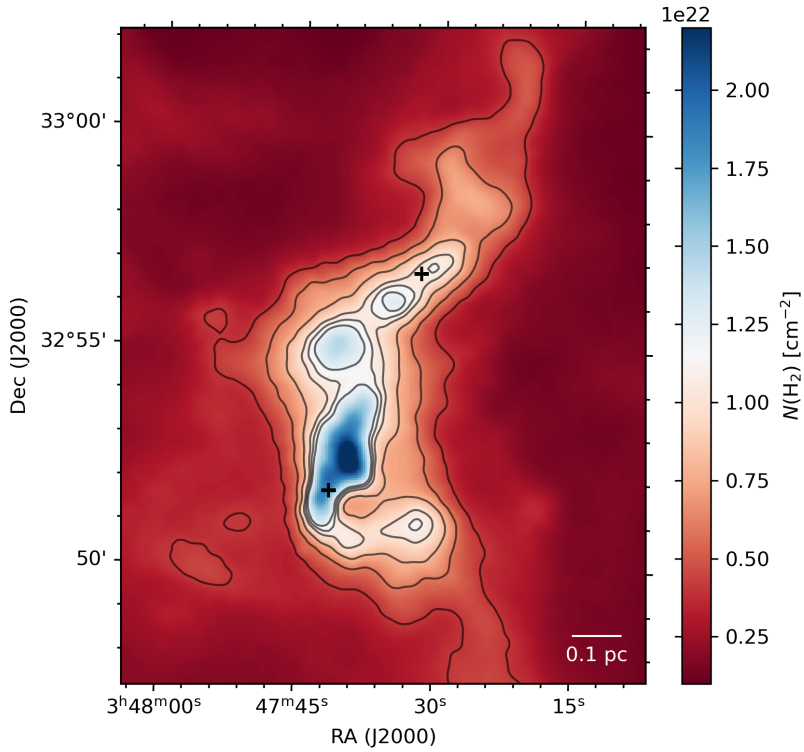

Figure 5.1: H_2 column density map for the B5 dark cloud, created from HGBS data. The black contours mark $N(H_2) = [0.4, 0.6, 0.8, 1.0, 1.1, 1.2] \times 10^{22}\,\mathrm{cm}^{-2}$. The black crosses mark the positions of the Class I protostar IRS1 in the south and B5-Hotspot in the north.

The mechanism that leads to the efficient desorption of ices at B5-Hotspot is largely unknown. Considering the low temperature and relatively high density at the position, as well as the strongly localized peak emission of methanol and the large distance to the IRS1 protostar in the south, thermal desorption, UV desorption, and cosmic ray desorption can be mostly ruled out. Reactive desorption is also rather unlikely, because it is not clear what process could cause the required localized increase in methanol formation efficiency at that specific position. A possible explanation might be enhanced grain-grain col-

lisions due to, e.g., a collision of cloud fragments on the large scale. Grain collisions have been invoked into an astrochemical model by Kalvāns and Silsbee (2022), showing that significant fractions of an ice mantle can be desorbed in a grain-grain collision event. Assuming that grain collisions are causing the desorption would mean that thermal desorption is, after all, the underlying mechanism releasing ice species into the gas phase, as part of the collisional energy is transferred into heat.

Regardless of the exact nature of the efficient ice desorption, the high abundances of gas phase water and COMs at a position not related to active star-formation and not characterized as a dense core make B5-Hotspot a unique dark cloud environment to study the chemistry of different types of interstellar molecules.

5.2 Paper A: Deep Search for Glycine Conformers in Barnard 5

Paper A investigates the possible presence of the simplest biotic amino acid glycine (NH_2CH_2COOH) at the position of B5-Hotspot. This study is motivated by the high gas phase abundances of COMs observed at B5-Hotspot as well as by the astrobiological hypothesis that fundamental biotic molecules such as amino acids and nucleobases could form in dark clouds (see sections 1.2 and 1.3). Despite various observational efforts over the past 40 years, neither glycine nor any other amino acid has been securely identified in the ISM. Yet, Ioppolo et al. (2021) recently showed in experiments and models that glycine could form at low temperatures and in the absence of energetic radiation. The main formation route is found to be

$$NH_2CH_2{}^* + HOCO^* \longrightarrow NH_2CH_2COOH\,. \tag{5.1}$$

Another simple molecule that can form via hydrogenation of the $HOCO^*$ radical at grain surfaces is the five-atom COM formic acid (HCOOH). HCOOH has two conformers, i.e., (*t*)*rans*-HCOOH and (*c*)*is*-HCOOH, with the *trans* conformer being lower in energy. At B5-Hotspot, the c/t ratio of HCOOH is about 0.06 (Taquet et al., 2017), which is extremely far from the equilibrium ratio of $c/t < 10^{-50}$, calculated by García de la Concepción et al. (2022) for

B5-Hotspot. In case of HCOOH, and at grain surfaces, the low-energy *trans* conformer is formed from the high-energy *cis* conformer of $HOCO^*$, i.e.,

$$c\text{-}HOCO^* + H \longrightarrow t\text{-}HCOOH\,, \tag{5.2}$$

while the high-energy *cis* conformer is formed from the low-energy t-$HOCO^*$ conformer, i.e.,

$$t\text{-}HOCO^* + H \longrightarrow c\text{-}HCOOH \tag{5.3}$$

(see Fig. 1, paper A). Given that most of the $HOCO^*$ radical is in its low-energy *trans* conformer (Goumans et al., 2008), the latter reaction can significantly increase the *c*-HCOOH abundance. A similar mechanism might be at work for glycine, which has several stable conformers. The two lowest-energy conformers are denoted NH_2CH_2COOH-I and NH_2CH_2COOH-II (hereafter, Gly-I and Gly-II). Equivalently to *t*-HCOOH, the low-energy Gly-I conformer is formed from *c*-$HOCO^*$, while the high-energy Gly-II conformer is formed from *t*-$HOCO^*$ (see Fig. 1, paper A), such that a non-equilibrium Gly-II/Gly-I ratio can be expected.

A simple LTE calculation was used to identify the Gly-I and Gly-II transitions that might produce observable spectral lines, assuming that the glycine abundance and distribution is similar to other COMs at B5-Hotspot. Using the OSO 20 m telescope, 14 Gly-I and 14 Gly-II transitions were targeted in the frequency range between approximately 71.1 GHz and 77.9 GHz. Pointed observations were made for a total of about 150 hr, resulting in a $T_{\rm mb}$ noise level of 4.2 – 6.2 mK. None of the targeted transitions has a corresponding spectral line detected. A line stacking method is used to further decrease the noise, which still does not result in a detection. However, sensitive upper limit column densities and abundances are derived for both conformers. The most stringent upper limit for the total glycine abundance (Gly-I plus Gly-II) is 2×10^{-10}, which is lower than the abundance of the least abundant COM, i.e., acetaldehyde (3.6×10^{-10}), observed at B5-Hotspot. Utilizing the updated $N(H_2)$ column density from Carl et al. (2026b), the upper limit abundance is 3.8×10^{-10}. The derived upper limit abundance is largely comparable to the upper limits from other studies investigating the possible presence of glycine in a cold molecular cloud source (Ceccarelli et al., 2000; Jiménez-Serra et al., 2016).

Contributions to paper A

For paper A, I was responsible for the data reduction, data analysis, and for main-authoring all parts of the paper. The data was taken by E. Wirström and H. Olofsson, and the proposals were written by E. Wirström. The original script for the line stacking was written by P. Bergman.

5.3 Paper B: The Distribution of Complex Organic Molecules in Barnard 5

In order to set constraints on the efficient desorption mechanism at B5-Hotspot as well as the formation conditions of COMs at low temperatures, paper B investigates the distribution of COMs in the area around B5-Hotspot. For that, several transitions of CH_3CHO, CH_3OCHO, and CH_3OCH_3, as well as the five-atom COMs HCOOH and CH_2CO (ketene) were targeted in pointed observations with the IRAM 30 m telescope towards two positions close to B5-Hotspot, i.e., the dense core East 189 (B5-East) and one position close to the edge of the B5 ridge (B5-Edge; see Fig. 1, paper B). At $T_{\rm mb}$ noise levels of 1.4 – 2.5 mK for B5-Edge and 2.9 – 6.2 mK for B5-East, spectral lines of all targeted COMs are observed towards both positions. In addition, several lines of CH_3OH were observed with the OSO 20 m telescope towards B5-Edge, B5-Hotspot, and B5-East. Column densities of all COMs except CH_3OH were calculated assuming LTE conditions.

Non-LTE models for CH_3OH were run with `ALI` to estimate $n(H_2)$, $T_{\rm k}$, and $N(CH_3OH)$ for all three positions, following the methods described in section 4.4. Using the recently published collisional rate coefficients from Dagdigian (2024) yields significant differences in best-fit $n(H_2)$ and $T_{\rm k}$, compared to models with the older rate coefficients from Rabli and Flower (2010), also produced in paper B with `ALI` as well as in Taquet et al. (2017) with RADEX. The best-fit value of $N(CH_3OH)$ is barely affected, because it is largely constrained by the observed line intensities. Utilizing the models with the Dagdigian (2024) rate coefficients as the reference models, no significant differences in $n(H_2)$, $T_{\rm k}$, and $N(CH_3OH)$ can be deduced from the modeling for the three target positions. B5-Edge is considered as an off-center position inside the B5-Hotspot model cloud, which is modeled with constant $n(H_2)$

and T_k. The models for B5-Hotspot and B5-East suggest a relatively high kinetic temperature of about 20 K, which might be consistent with a scenario in which ices in the area are released by grain-grain collisions.

The detection of emission from all targeted COMs towards B5-Edge and B5-East is showing that the efficient ice desorption, which releases ices at B5-Hotspot, is likely active at those positions as well. Similar relative abundances of the three large COMs CH_3CHO, CH_3OCHO, and CH_3OCH_3 are measured towards B5-Edge, B5-Hotspot, and B5-East, indicating a shared physical and chemical evolution. Furthermore, the CH_2CO/HCOOH ratio differs significantly among the three positions, which might be due to a different C/O ratio, as both CH_2CO and HCOOH have efficient surface formation routes starting from HCO^*, reacting with either C or O. The lowest CH_2CO/HCOOH ratio is observed at B5-Hotspot. This would indicate the lowest C/O, which is consistent with the high abundance of gas phase water at that position. Comparison of the measured COM column densities and abundances of the three large COMs to the data for a set of prestellar and starless cores in Perseus from Scibelli et al. (2024) indicates that the ices in the B5-Hotspot region are less evolved but released more efficiently.

Contributions to paper B

For paper B, I was responsible for the IRAM 30 m observations (including writing the proposal), the data reduction, data analysis, and for main-authoring all parts of the paper. The OSO 20 m data was taken by H. Olofsson, and the observing proposal was written by P. Bergman. The original script for the non-LTE modeling routine with `ALI` was written by P. Bergman. Part of the IRAM 30 m data was taken by the telescope staff.

5.4 Paper C: Sulfur Chemistry in Cold Water-Rich Gas in Barnard 5

The total gas phase sulfur abundance in dense molecular cloud regions can only account for about 0.1 % of the total cosmic sulfur abundance (S/H $\approx 10^{-5}$; Asplund et al., 2009; Jenkins, 2009). Paper C investigates the gas phase sulfur abundance at B5-Hotspot, where the efficient ice evaporation has the potential

to significantly increase the S/H value relative to other dark cloud sources, assuming that part of the "missing" sulfur is locked-up in ices. Furthermore, the high abundance of gas phase water at B5-Hotspot can have interesting implications for the sulfur chemistry.

The utilized data set consists of spectral line data obtained in pointed observations with the OSO 20 m, IRAM 30 m, and Yebes 40 m telescopes between 2015 and 2026. In the data, 33 lines of 16 sulfur-bearing species (including isotopologues) were clearly identified. Column densities were calculated by using LTE and non-LTE methods, depending on the molecule. The derived total sulfur abundance at B5-Hotspot is S/H $\approx 2\times10^{-8}$, and the sulfur budget is dominated by SO, H_2S, and CS (72 %), followed by H_2CS, OCS, and SO_2 (21 %). The remaining species are isotopologues of CS, SO, SO_2, and OCS, as well as HCS^+ and the carbon-chains C_2S and C_3S. The total sulfur budget at B5-Hotspot is significantly higher than towards other dark cloud sources, including some protostellar environments and a photodissociation region. This is another expression of the uniqueness of B5-Hotspot, characterized by very efficient ice desorption, especially considering the large contribution of H_2S to the total budget (29 %), compared to the other sources (14 % on average). H_2S is predominantly formed on grain surfaces, such that the high contribution of H_2S is related to the efficient ice evaporation. However, the total sulfur budget at B5-Hotspot is still about three orders of magnitude lower than the cosmic sulfur abundance.

The abundances of oxygen-bearing sulfur species at B5-Hotspot are significantly higher than the abundances of carbon-bearing species. This is likely due to the high abundance of gas phase water, which is producing an oxygen-rich environment that favors the formation of SO and SO_2 over C_2S and C_3S. This is in-line with the low CH_2CO/HCOOH ratio at B5-Hotspot, reported in paper B. Considering the sulfur data for the other dark cloud sources, a clear separation into sources dominated by either an oxygen- or carbon-chemistry is observed based on the $[SO+SO_2]/[C_2S+C_3S]$ ratio. Furthermore, based on the similarities between gas phase H_2S and H_2O chemistries, it is speculated whether H_2S could be used as a tracer of an oxygen-dominated chemistry induced by high amounts of H_2O. However, no correlation is found between H_2S abundance and $[SO + SO_2]/[C_2S + C_3S]$.

Contributions to paper C

For paper C, I was responsible for the IRAM 30 m observations (including writing the proposal), the data reduction, data analysis, and for main-authoring all parts of the paper. The OSO 20 m data was taken by E. Wirström and H. Olofsson, and the proposals were written by E. Wirström and P. Bergman. The Yebes 40m data was taken by M. Jiménez-Donaire and I was responsible for writing the proposal. The original script for the non-LTE modeling routine with `ALI` was written by P. Bergman. Assistance during some of the IRAM 30 m observations was provided by A. Punanova and some of the data was taken by the IRAM staff.

CHAPTER 6

Summary and Outlook

In the papers appended to this thesis, different aspect of the gas phase molecular content at B5-Hotspot have been investigated and possible gas phase reactions and grain surface reactions as well as non-energetic desorption mechanisms, that might have produced the observed molecular abundances, have been discussed. In paper A, no glycine could be detected in the gas phase at B5-Hotspot at a noise level of 4.2 – 6.2 mK, despite the very efficient desorption of ices at that position, including several COMs. In paper B, it has been shown that the efficient desorption is not only active at B5-Hotspot but also at surrounding positions, i.e., B5-Edge and B5-East, as indicated by the detection of gas phase COMs (HCOOH, CH_2CO, CH_3OH, CH_3CHO, CH_3OCHO, and CH_3OCH_3) at both positions. This puts new constraints on the desorption mechanism, whose nature is still largely unknown, but which could be related to grain-grain collisions. Non-LTE models for CH_3OH suggest a relatively high kinetic temperature for B5-Hotspot and B5-East (~ 20 K), which might be consistent with this scenario. Paper B also puts new constraints on the low-temperature formation of some COMs by showing evidence for a relation between CH_3OCHO and CH_3OCH_3 as well as for the formation of CH_3CHO from CH_2CO (especially when compared to literature data). In paper C, the

total sulfur abundance at B5-Hotspot has been derived from observations of 16 different sulfur-bearing species (including isotopologues). It is found to be about 2×10^{-8}, which is still about three orders of magnitude lower than the cosmic sulfur abundance ($\sim 10^{-5}$), despite the efficient ice desorption at B5-Hotspot. The gas phase sulfur chemistry at B5-Hotspot appears to be dominated by oxygen, induced by the high gas phase abundance of water at that position. Comparison to literature data shows that the sulfur abundance at B5-Hotspot is significantly higher than towards other dark cloud sources, and there appears to be a general separation into sources with an oxygen-/carbon-dominated sulfur chemistry.

The detection of gas phase COMs in the area around B5-Hotspot (and especially at B5-Edge) indicates that the formation of COMs clearly predates the formation of dense starless and prestellar cores, and that COMs (or their precursors) might be ubiquitous in the ices in dense filaments of molecular clouds. This could be further investigated by observations of COMs in other early-stage molecular cloud environments. The efficient desorption of ices at B5-Hotspot could be better characterized by ice observations towards that position, e.g., with JWST (James Webb Space Telescope). For instance, comparing the abundances of, e.g., CH_3OH in the gas and ice would provide a direct measurement of the amount of ice released into the gas. The search for glycine at B5-Hotspot is one of a few that focused on a low-temperature environment and on low-frequency glycine transitions, expected to be strongest at those conditions. In the future, using the capabilities of the planned 50 m telescope AtLAST (Atacama Large Aperture Submillimeter Telescope; Cicone et al., 2026) in Chile, which will have a broad frequency coverage of 30 – 950 GHz, low-frequency transitions of glycine (or other biotically interesting COMs) could be targeted with high sensitivity towards B5-Hotspot or other promising sources (Jiménez-Serra et al., 2025). In addition, the growing number and capabilities of machine learning tools related to astrochemical research have the potential to drastically simplify certain steps of the data analysis (like spectral line identification and characterization) in the near future.

References

Allen, M. and Robinson, G.W. (1975). "Formation of molecules on small interstellar grains." In: *The Astrophysical Journal* 195, pp. 81–90. DOI: 10.1086/153306.

Anders, E. et al. (1974). "Interstellar Molecules: Origin by Catalytic Reactions on Grain Surfaces?" In: *The Astrophysical Journal Letters* 192, p. L101. DOI: 10.1086/181601.

André, P.J. et al. (2010). "From filamentary clouds to prestellar cores to the stellar IMF: Initial highlights from the Herschel Gould Belt Survey". In: *Astronomy and Astrophysics* 518, p. L102. DOI: 10.1051/0004-6361/201014666.

– (2014). "From Filamentary Networks to Dense Cores in Molecular Clouds: Toward a New Paradigm for Star Formation". In: *Protostars and Planets VI*. Ed. by H. Beuther et al. University of Arizona Press, pp. 27–51. DOI: 10.2458/azu_uapress_9780816531240-ch002.

– (2022). "The typical width of Herschel filaments". In: *Astronomy and Astrophysics* 667, p. L1. DOI: 10.1051/0004-6361/202244541.

Arzoumanian, D. et al. (2011). "Characterizing interstellar filaments with Herschel in IC 5146". In: *Astronomy and Astrophysics* 529, p. L6. DOI: 10.1051/0004-6361/201116596.

– (2019). "Characterizing the properties of nearby molecular filaments observed with Herschel". In: *Astronomy and Astrophysics* 621, A42. DOI: 10.1051/0004-6361/201832725.

Asplund, M. et al. (2009). "The Chemical Composition of the Sun". In: *Annual Review of Astronomy Astrophysics* 47, pp. 481–522. DOI: 10.1146/annurev.astro.46.060407.145222.

Atkins, P. et al. (2018). *Physical Chemistry - Quantum Chemistry, Spectroscopy, and Statistical Thermodynamics*. Oxford University Press.

Ball, J.A. et al. (1970). "Detection of Methyl Alcohol in Sagittarius". In: *The Astrophysical Journal Letters* 162, p. L203. DOI: 10.1086/180654.

Bar-Nun, A. (1975). "Interstellar molecules: direct formation on graphite grains." In: *The Astrophysical Journal* 197, pp. 341–345. DOI: 10.1086/153518.

Barnard, E.E. (1907). "On a nebulous groundwork in the constellation Taurus." In: *The Astrophysical Journal* 25, pp. 218–225. DOI: 10.1086/141434.

Barnard, E.E. et al. (1927). *A Photographic Atlas of Selected Regions of the Milky Way*.

Beckwith, S. et al. (1986). "Small-Scale Structure of the Circumstellar Gas of HL Tauri and R Monocerotis". In: *The Astrophysical Journal* 309, p. 755. DOI: 10.1086/164645.

Bennett, J. et al. (2010). *Astronomie - Die kosmische Perspektive*. Pearson Studium.

Boogert, A.C.A. et al. (2008). "The c2d Spitzer Spectroscopic Survey of Ices around Low-Mass Young Stellar Objects. I. H_2O and the 5-8 μm Bands". In: *The Astrophysical Journal* 678, pp. 985–1004. DOI: 10.1086/533425.

– (2015). "Observations of the icy universe." In: *Annual Review of Astronomy and Astrophysics* 53, pp. 541–581. DOI: 10.1146/annurev-astro-082214-122348.

Brinch, C. and Hogerheijde, M.R. (2010). "LIME - a flexible, non-LTE line excitation and radiation transfer method for millimeter and far-infrared wavelengths". In: *Astronomy and Astrophysics* 523, A25. DOI: 10.1051/0004-6361/201015333.

Brown, R.D. et al. (1979). "A search for interstellar glycine." In: *Monthly Notices of the Royal Astronomical Society* 186, 5P–8P. DOI: 10.1093/mnras/186.1.5P.

Buhl, D. and Snyder, L.E. (1970). "The Detection of Interstellar HCN". In: *Bulletin of the American Astronomical Society*. Vol. 2, p. 299.

Burkhardt, A.M. et al. (2021). "Discovery of the Pure Polycyclic Aromatic Hydrocarbon Indene (c-C9H8) with GOTHAM Observations of TMC-1".

In: *The Astrophysical Journal Letters* 913, p. L18. DOI: 10.3847/2041-8213/abfd3a.

Callahan, M.P. et al. (2011). "Carbonaceous meteorites contain a wide range of extraterrestrial nucleobases". In: *Proceedings of the National Academy of Science* 108, pp. 13995–13998. DOI: 10.1073/pnas.1106493108.

Cami, J. et al. (2010). "Detection of C_{60} and C_{70} in a Young Planetary Nebula". In: *Science* 329, p. 1180. DOI: 10.1126/science.1192035.

Carl, T. et al. (2026a). "Sulfur chemistry in cold water-rich gas in Barnard 5". In.

– (2026b). "The distribution of complex organic molecules in Barnard 5". In: *Astronomy and Astrophysics* 710, A233. DOI: 10.1051/0004-6361/202558098.

Caselli, P. et al. (2012). "First Detection of Water Vapor in a Pre-stellar Core". In: *The Astrophysical Journal Letters* 759, p. L37. DOI: 10.1088/2041-8205/759/2/L37.

Ceccarelli, C. et al. (2000). "Search for glycine in the solar type protostar IRAS 16293-2422". In: *Astronomy and Astrophysics* 362, pp. 1122–1126.

– (2014). "Deuterium Fractionation: The Ariadne's Thread from the Precollapse Phase to Meteorites and Comets Today". In: *Protostars and Planets VI*. Ed. by H. Beuther et al. University of Arizona Press, pp. 859–882. DOI: 10.2458/azu_uapress_9780816531240.

Cernicharo, J. et al. (2021). "Pure hydrocarbon cycles in TMC-1: Discovery of ethynyl cyclopropenylidene, cyclopentadiene, and indene". In: *Astronomy and Astrophysics* 649, p. L15. DOI: 10.1051/0004-6361/202141156.

Chang, Q. and Herbst, E. (2012). "A Unified Microscopic-Macroscopic Monte Carlo Simulation of Gas-grain Chemistry in Cold Dense Interstellar Clouds". In: *The Astrophysical Journal* 759.2, p. 147. DOI: 10.1088/0004-637X/759/2/147.

Chapovsky, P.L. and Hermans, L.J.F. (1999). "Nuclear Spin Conversion in Polyatomic Molecules". In: *Annual Review of Physical Chemistry* 50, pp. 315–345. DOI: 10.1146/annurev.physchem.50.1.315.

Charnley, S.B. (1997). "On the nature of interstellar organic chemistry". In: *IAU Colloquium 161: Astronomical and Biochemical Origins and the Search for Life in the Universe*. Ed. by C. Batalli Cosmovici, S. Bowyer, and D. Werthimer, p. 89.

Charnley, S.B. (2001). "Interstellar Organic Chemistry". In: *The Bridge Between the Big Bang and Biology*. Ed. by F. Giovannelli, p. 139.

Chen, Y. et al. (2024). "JOYS+: The link between the ice and gas of complex organic molecules: Comparing JWST and ALMA data of two low-mass protostars". In: *Astronomy and Astrophysics* 690, A205. DOI: 10.1051/0004-6361/202450706.

Cherchneff, Isabelle et al. (1992). "Polycyclic Aromatic Hydrocarbon Formation in Carbon-rich Stellar Envelopes". In: *The Astrophysical Journal* 401, p. 269. DOI: 10.1086/172059.

Cheung, A.C. et al. (1968). "Detection of NH_3 Molecules in the Interstellar Medium by Their Microwave Emission". In: *Physical Review Letters* 21, pp. 1701–1705. DOI: 10.1103/PhysRevLett.21.1701.

– (1969). "Detection of Water in Interstellar Regions by its Microwave Radiation". In: *Nature* 221, pp. 626–628. DOI: 10.1038/221626a0.

Chuang, K.-J. et al. (2018). "Reactive Desorption of CO Hydrogenation Products under Cold Pre-stellar Core Conditions". In: *The Astrophysical Journal* 853, p. 102. DOI: 10.3847/1538-4357/aaa24e.

– (2022). "Formation of the Simplest Amide in Molecular Clouds: Formamide (NH_2CHO) and Its Derivatives in H_2O-rich and CO-rich Interstellar Ice Analogs upon VUV Irradiation". In: *The Astrophysical Journal* 933, p. 107. DOI: 10.3847/1538-4357/ac7320.

Cicone, C. et al. (2026). "The Atacama Large Aperture Submillimeter Telescope (AtLAST): enabling large-scale sub-mm science beyond 2030". In: *arXiv e-prints*. DOI: 10.48550/arXiv.2607.05022.

Combes, F. et al. (1996). "Search for interstellar glycine." In: *Astronomy and Astrophysics* 308, pp. 618–622.

Condon, J.J. and Ransom, S.M. (2016). *Essential Radio Astronomy*. Princeton University Press.

Cooper, G. et al. (2001). "Carbonaceous meteorites as a source of sugar-related organic compounds for the early Earth". In: *Nature* 414, pp. 879–883. DOI: 10.1038/414879A.

Cordiner, M.A. et al. (2025). "A D/H ratio consistent with Earth's water in Halley-type comet 12P from ALMA HDO mapping". In: *Nature Astronomy*. DOI: 10.1038/s41550-025-02614-7.

Cuppen, H.M. et al. (2009). "Microscopic simulation of methanol and formaldehyde ice formation in cold dense cores". In: *Astronomy and Astrophysics* 508, pp. 275–287. DOI: 10.1051/0004-6361/200913119.

– (2011). "CO ice mixed with CH_3OH: the answer to the non-detection of the 2152 cm^{-1} band?" In: *Monthly Notices of the Royal Astronomical Society* 417, pp. 2809–2816. DOI: 10.1111/j.1365-2966.2011.19443.x.

– (2017). "Grain Surface Models and Data for Astrochemistry". In: *Space Science Reviews* 212, pp. 1–58. DOI: 10.1007/s11214-016-0319-3.

– (2024). "Laboratory and Computational Studies of Interstellar Ices". In: *Annual Review of Astronomy and Astrophysics* 62, pp. 243–286. DOI: 10.1146/annurev-astro-071221-052732.

Dagdigian, P.J. (2019). "Excitation of Astrophysical Molecules". In: *Gas-Phase Chemistry in Space*. IOP Publishing, 7-1 to 7–29. DOI: 10.1088/2514-3433/aae1b5ch7.

– (2024). "Rotational excitation of methanol in collisions with molecular hydrogen". In: *Monthly Notices of the Royal Astronomical Society* 527, pp. 2209–2213. DOI: 10.1093/mnras/stad3303.

Dalgarno, A. and Black, J.H. (1976). "REVIEW: Molecule formation in the interstellar gas". In: *Reports on Progress in Physics* 39, pp. 573–612. DOI: 10.1088/0034-4885/39/6/002.

de Jong, T. et al. (1980). "Hydrostatic models of molecular clouds." In: *Astronomy and Astrophysics* 91, pp. 68–84.

Dobbs, C.L. et al. (2014). "Formation of Molecular Clouds and Global Conditions for Star Formation". In: *Protostars and Planets VI*. Ed. by H. Beuther et al. University of Arizona Press, pp. 3–26. DOI: 10.2458/azu_uapress_9780816531240.

Dorschner, J. (2003). "From Dust Astrophysics Towards Dust Mineralogy – A Historical Review". In: *Astromineralogy*. Ed. by T. Henning. Springer, pp. 1–54.

Douglas, A.E. and Herzberg, G. (1941). "Note on CH^+ in Interstellar Space and in the Laboratory." In: *The Astrophysical Journal* 94, p. 381. DOI: 10.1086/144342.

Draine, B.T. (2011). *Physics of the Interstellar and Intergalactic Medium*. Princeton University Press.

Drozdovskaya, M.N. et al. (2019). "Ingredients for solar-like systems: protostar IRAS 16293-2422 B versus comet 67P/Churyumov-Gerasimenko". In:

Monthly Notices of the Royal Astronomical Society 490, pp. 50–79. DOI: 10.1093/mnras/stz2430.

Dunham, T. (1937). "Interstellar Neutral Potassium and Neutral Calcium". In: *Publications of the Astronomical Society of the Pacific* 49, p. 26. DOI: 10.1086/124759.

Dutrey, A. et al. (2014). "Physical and Chemical Structure of Planet-Forming Disks Probed by Millimeter Observations and Modeling". In: *Protostars and Planets VI*. Ed. by H. Beuther et al. University of Arizona Press, pp. 317–338. DOI: 10.2458/azu_uapress_9780816531240.

Eddington, A.S. (1937). "Interstellar matter". In: *The Observatory* 60, pp. 99–103.

Ehrenfreund, P. et al. (2001). "Extraterrestrial amino acids in Orgueil and Ivuna: Tracing the parent body of CI type carbonaceous chondrites". In: *Proceedings of the National Academy of Sciences* 98, pp. 2138–2141. DOI: 10.1073/pnas.051502898.

Ehrenfreund, P. and Charnley, S.B. (2000). "Organic Molecules in the Interstellar Medium, Comets, and Meteorites: A Voyage from Dark Clouds to the Early Earth". In: *Annual Review of Astronomy and Astrophysics* 38, pp. 427–483. DOI: 10.1146/annurev.astro.38.1.427.

Ewen, H.I. and Purcell, E.M. (1951). "Observation of a Line in the Galactic Radio Spectrum: Radiation from Galactic Hydrogen at 1,420 Mc./sec." In: *Nature* 168, p. 356. DOI: 10.1038/168356a0.

Faure, A. (2019). "Molecular collisional excitation: theory, experiment and observations". In: *SF2A-2019: Proceedings of the Annual meeting of the French Society of Astronomy and Astrophysics*. Ed. by P. Di Matteo et al.

Fourikis, N. et al. (1974). "Microwave emission of the $2_{11} \rightarrow 2_{12}$ rotational transition in interstellar acetaldehyde". In: *Australian Journal of Physics* 27, p. 425. DOI: 10.1071/PH740425.

Fraunhofer, J. (1817). "Bestimmung des Brechungs- und des Farbenzerstreungsvermögens verschiedener Glasarten in Bezug auf die Vervollkommnung achromatischer Fernröhre". In: *Annalen der Physik* 56, pp. 264–313. DOI: 10.1002/andp.18170560706.

Frenklach, M. and Feigelson, E.D. (1989). "Formation of Polycyclic Aromatic Hydrocarbons in Circumstellar Envelopes". In: *The Astrophysical Journal* 341, p. 372. DOI: 10.1086/167501.

Friberg, P. and Hjalmarson, Å. (1990). "Molecular clouds in the Milky Way". In: *Molecular Astrophysics*. Ed. by T.W. Hartquist. Cambridge University Press, pp. 3–34.

Fuchs, G.W. et al. (2009). "Hydrogenation reactions in interstellar CO ice analogues. A combined experimental/theoretical approach". In: *Astronomy and Astrophysics* 505, pp. 629–639. DOI: 10.1051/0004-6361/200810784.

Furukawa, Y. et al. (2019). "Extraterrestrial ribose and other sugars in primitive meteorites". In: *Proceedings of the National Academy of Science* 116, pp. 24440–24445. DOI: 10.1073/pnas.1907169116.

García de la Concepción, J. et al. (2022). "The trans/cis ratio of formic (HCOOH) and thioformic (HC(O)SH) acids in the interstellar medium". In: *Astronomy and Astrophysics* 658, A150. DOI: 10.1051/0004-6361/202142287.

Garrod, R.T. (2013). "A Three-phase Chemical Model of Hot Cores: The Formation of Glycine". In: *The Astrophysical Journal* 765, p. 60. DOI: 10.1088/0004-637X/765/1/60.

Garrod, Robin et al. (2006). "Are gas-phase models of interstellar chemistry tenable? The case of methanol". In: *Faraday Discussions* 133, p. 51. DOI: 10.1039/b516202e.

Goldsmith, P.F. and Langer, W.D. (1999). "Population Diagram Analysis of Molecular Line Emission". In: *The Astrophysical Journal* 517, pp. 209–225. DOI: 10.1086/307195.

Gordy, W. and Cook, R.L. (1984). *Microwave Molecular Spectra*. Wiley.

Goto, M. et al. (2021). "Water and methanol ice in L1544". In: *Astronomy and Astrophysics* 651, A53. DOI: 10.1051/0004-6361/201936385.

Gottlieb, C.A. and Ball, J.A. (1973). "Interstellar Sulfur Monoxide". In: *The Astrophysical Journal Letters* 184, p. L59. DOI: 10.1086/181288.

Gould, R.J. et al. (1963). "The Interstellar Abundance of the Hydrogen Molecule. II. Galactic Abundance and Distribution." In: *The Astrophysical Journal* 138, p. 408. DOI: 10.1086/147655.

Gould, R.J. and Salpeter, E.E. (1963). "The Interstellar Abundance of the Hydrogen Molecule. I. Basic Processes." In: *The Astrophysical Journal* 138, p. 393. DOI: 10.1086/147654.

Goumans, T.P.M. et al. (2008). "Formation of CO_2 on a carbonaceous surface: a quantum chemical study". In: *Monthly Notices of the Royal Astronomical Society* 384, pp. 1158–1164. DOI: 10.1111/j.1365-2966.2007.12788.x.

Griffiths, D.J. (1995). *Introduction to Quantum Mechanics*. Prentice Hall.

Gußmann, E. A. (1979). "D. MIHALAS: Stellar Atmospheres. Second Edition. W. H.FREEMAN & Co., San Francisco 1978. XX + 632 p., Price US $ 27.50". In: *Astronomische Nachrichten* 300, pp. 221–222. DOI: https://doi.org/10.1002/asna.19793000416.

Hadraoui, K. et al. (2019). "Distributed glycine in comet 67P/Churyumov-Gerasimenko". In: *Astronomy and Astrophysics* 630, A32. DOI: 10.1051/0004-6361/201935018.

Haken, H. and Wolf, H.C. (2006). *Molekülphysik und Quantenchemie*. Springer.

Hartmann, J. (1904). "Investigations on the spectrum and orbit of delta Orionis." In: *The Astrophysical Journal* 19, pp. 268–286. DOI: 10.1086/141112.

Hartquist, T.W. (1990). *Molecular Astrophysics*. Cambridge University Press.

Heger, M.L. (1919). "Stationary Sodium Lines in Spectroscopic Binaries". In: *Publications of the Astronomical Society of the Pacific* 31, pp. 304–305. DOI: 10.1086/122890.

Herbst, E. and Klemperer, W. (1973). "The Formation and Depletion of Molecules in Dense Interstellar Clouds". In: *The Astrophysical Journal* 185, pp. 505–534. DOI: 10.1086/152436.

Hirota, E. (2011). *High-Resolution Spectroscopy of Transient Molecules*. Springer.

Hollas, J.M (1998). *High Resolution Spectroscopy*. Wiley.

– (2004). *Modern Spectroscopy*. Wiley.

Hollis, J.M. et al. (2000). "Interstellar Glycolaldehyde: The First Sugar". In: *The Astrophysical Journal Letters* 540, pp. L107–L110. DOI: 10.1086/312881.

Hoyle, F. and Wickramasinghe, N.C. (1977). "Prebiotic molecules and interstellar grain clumps". In: *Nature* 266, pp. 241–242. DOI: 10.1038/266241b0.

Hu, C.-H. et al. (1993). "Glycine Conformational Analysis". In: *Journal of the American Chemical Society* 115, pp. 2923–2929.

Hubble, E.P. (1925). "Cepheids in spiral nebulae". In: *The Observatory* 48, pp. 139–142.

– (1926). "Extragalactic nebulae." In: *The Astrophysical Journal* 64, pp. 321–369. DOI: 10.1086/143018.

Ioppolo, S. et al. (2021). "A non-energetic mechanism for glycine formation in the interstellar medium". In: *Nature Astronomy* 5, pp. 197–205. DOI: 10.1038/s41550-020-01249-0.

Jenkins, E.B. (2009). "A Unified Representation of Gas-Phase Element Depletions in the Interstellar Medium". In: *The Astrophysical Journal* 700, pp. 1299–1348. DOI: 10.1088/0004-637X/700/2/1299.

Jewell, P.R. (2002). "Millimeter Wave Calibration Techniques". In: *Single-Dish Radio Astronomy: Techniques and Applications*. Ed. by Snezana Stanimirovic et al. Vol. 278. Astronomical Society of the Pacific Conference Series, pp. 313–328.

Jiménez-Serra, I. et al. (2016). "The Spatial Distribution of Complex Organic Molecules in the L1544 Pre-stellar Core". In: *The Astrophysical Journal Letters* 830, p. L6. DOI: 10.3847/2041-8205/830/1/L6.

– (2020). "Toward the RNA-World in the Interstellar Medium—Detection of Urea and Search of 2-Amino-oxazole and Simple Sugars". In: *Astrobiology* 20. DOI: 10.1089/ast.2019.2125.

– (2025). "The Emergence of Prebiotic Chemistry in the ISM". In: *arXiv e-prints*. DOI: 10.48550/arXiv.2512.14772.

– (2026). "Detection of a four-carbon sugar in interstellar space". In: *Nature Astronomy*. DOI: 10.1038/s41550-026-02905-7.

Johansen, A. et al. (2021). "A pebble accretion model for the formation of the terrestrial planets in the Solar System". In: *Science Advances* 7, eabc0444. DOI: 10.1126/sciadv.abc0444.

Jones, A.P. et al. (2013). "The evolution of amorphous hydrocarbons in the ISM: dust modelling from a new vantage point". In: *Astronomy and Astrophysics* 558, A62. DOI: 10.1051/0004-6361/201321686.

Jones, P.A. et al. (2007). "A Search for biomolecules in Sagittarius B2 (LMH) with the Australia Telescope Compact Array". In: *Monthly Notices of the Royal Astronomical Society* 374, pp. 579–589. DOI: 10.1111/j.1365-2966.2006.11175.x.

Kahn, F.D. (1955). "The Heating and Cooling of Interstellar Gas Clouds". In: *Gas Dynamics of Cosmic Clouds*. Vol. 2. IAU Symposium, p. 60.

Kaifu, N. et al. (1974). "Detection of Interstellar Methylamine". In: *The Astrophysical Journal Letters* 191, pp. L135–L137. DOI: 10.1086/181569.

Kalvāns, J. and Silsbee, K. (2022). "Icy molecule desorption in interstellar grain collisions". In: *Monthly Notices of the Royal Astronomical Society* 515, pp. 785–794. DOI: 10.1093/mnras/stac1792.

Kapteyn, J.C. (1909). "On the Absorption of Light in Space". In: *The Astrophysical Journal* 29, p. 46. DOI: 10.1086/141618.

Kirchhoff, G.R. (1860). "Ueber das Verhältniss zwischen dem Emissionsvermögen und dem Absorptionsvermögen der Körper für Wärme und Licht". In: *Annalen der Physik* 109, pp. 275–301. DOI: 10.1002/andp.18601850205.

Kirchhoff, G.R. and Bunsen, R.W. (1860). "Chemische Analyse durch Spectralbeobachtungen". In: *Annalen der Physik* 186, pp. 161–189. DOI: 10.1002/andp.18601860602.

– (1861). "Chemische Analyse durch Spectralbeobachtungen". In: *Annalen der Physik* 189, pp. 337–381. DOI: 10.1002/andp.18611890702.

Koga, T. and Naraoka, H. (2017). "A new family of extraterrestrial amino acids in the Murchison meteorite". In: *Scientific Reports* 7, p. 636. DOI: 10.1038/s41598-017-00693-9.

Kvenvolden, K. et al. (1970). "Evidence for Extraterrestrial Amino-acids and Hydrocarbons in the Murchison Meteorite". In: *Nature* 228, pp. 923–926. DOI: 10.1038/228923a0.

Lampton, M. et al. (1976). "Parameter estimation in X-ray astronomy." In: *The Astrophysical Journal* 208, pp. 177–190. DOI: 10.1086/154592.

Lee, K.L.K. et al. (2021). "Machine Learning of Interstellar Chemical Inventories". In: *The Astrophysical Journal Letters* 917, p. L6. DOI: 10.3847/2041-8213/ac194b.

Leemker, M. et al. (2025). "Pristine ices in a planet-forming disk revealed by heavy water". In: *Nature Astronomy*. DOI: 10.1038/s41550-025-02663-y.

Li, A. and Draine, B.T. (2001). "Infrared Emission from Interstellar Dust. II. The Diffuse Interstellar Medium". In: *The Astrophysical Journal* 554, pp. 778–802. DOI: 10.1086/323147.

Lique, F. et al. (2020). "Hyperfine excitation of SH^+ by H". In: *Astronomy and Astrophysics* 638, A72. DOI: 10.1051/0004-6361/202038041.

Madhusudhan, Nikku et al. (2025). "New Constraints on DMS and DMDS in the Atmosphere of K2-18 b from JWST MIRI". In: *The Astrophysical Journal Letters* 983, p. L40. DOI: 10.3847/2041-8213/adc1c8.

Mangum, J.G. and Shirley, Y.L. (2015). "How to Calculate Molecular Column Density". In: *The Astronomical Society of the Pacific* 127, pp. 266–298. DOI: 10.1086/680323.

Mathis, J.S. et al. (1977). "The size distribution of interstellar grains." In: *The Astrophysical Journal* 217, pp. 425–433. DOI: 10.1086/155591.

Mathis, J.S. (1996). "Dust Models with Tight Abundance Constraints". In: *The Astrophysical Journal* 472, p. 643. DOI: 10.1086/178094.

McClure, M.K. et al. (2023). "An Ice Age JWST inventory of dense molecular cloud ices". In: *Nature Astronomy* 7, pp. 431–443. DOI: 10.1038/s41550-022-01875-w.

McCrea, W.H. and McNally, D. (1960). "The formation of Population I stars, II. The formation of molecular hydrogen in interstellar matter". In: *Monthly Notices of the Royal Astronomical Society* 121, p. 238. DOI: 10.1093/mnras/121.2.238.

McDowell, M.R.C. (1961). "On the formation of H2 in H I regions". In: *The Observatory* 81, pp. 240–243.

McGuire, B.A. et al. (2021). "Detection of two interstellar polycyclic aromatic hydrocarbons via spectral matched filtering". In: *Science* 371, pp. 1265–1269. DOI: 10.1126/science.abb7535.

McGuire, B.A. (2022). "2021 Census of Interstellar, Circumstellar, Extragalactic, Protoplanetary Disk, and Exoplanetary Molecules". In: *The Astrophysical Journal Supplement Series* 259, p. 30. DOI: 10.3847/1538-4365/ac2a48.

McKellar, A. (1940). "Evidence for the Molecular Origin of Some Hitherto Unidentified Interstellar Lines". In: *Publications of the Astronomical Society of the Pacific* 52, p. 187. DOI: 10.1086/125159.

Merrill, P.W. (1934). "Unidentified Interstellar Lines". In: *Publications of the Astronomical Society of the Pacific* 46, p. 206. DOI: 10.1086/124460.

– (1936). "Stationary Lines in the Spectrum of the Binary Star Boss 6142". In: *The Astrophysical Journal* 83, p. 126. DOI: 10.1086/143707.

Min, M. et al. (2007). "The shape and composition of interstellar silicate grains". In: *Astronomy and Astrophysics* 462, pp. 667–676. DOI: 10.1051/0004-6361:20065436.

Minissale, M. et al. (2016). "Dust as interstellar catalyst. I. Quantifying the chemical desorption process". In: *Astronomy and Astrophysics* 585, A24. DOI: 10.1051/0004-6361/201525981.

Molinari, S. et al. (2014). "The Milky Way as a Star Formation Engine". In: *Protostars and Planets VI*. Ed. by H. Beuther et al. University of Arizona Press, pp. 125–148. DOI: 10.2458/azu_uapress_9780816531240.

Molster, F.J. and Waters, B.F.M. (2003). "The Mineralogy of Interstellar and Circumstellar Dust". In: *Astromineralogy*. Ed. by T. Henning. Springer, pp. 121–170.

Müller, B. et al. (2021). "Spectroscopic measurements of CH_3OH in layered and mixed interstellar ice analogues". In: *Astronomy and Astrophysics* 652, A126. DOI: 10.1051/0004-6361/202039139.

Müller, H.S.P. et al. (2001). "The Cologne Database for Molecular Spectroscopy, CDMS". In: *Astronomy and Astrophysics* 370, pp. L49–L52. DOI: 10.1051/0004-6361:20010367.

– (2005). "The Cologne Database for Molecular Spectroscopy, CDMS: a useful tool for astronomers and spectroscopists". In: *Journal of Molecular Structure* 742, pp. 215–227. DOI: 10.1016/j.molstruc.2005.01.027.

Nuevo, M. et al. (2018). "Deoxyribose and deoxysugar derivatives from photoprocessed astrophysical ice analogues and comparison to meteorites". In: *Nature Communications* 9, p. 5276. DOI: 10.1038/s41467-018-07693-x.

Oba, Y. et al. (2019). "Nucleobase synthesis in interstellar ices". In: *Nature Communications* 10, p. 4413. DOI: 10.1038/s41467-019-12404-1.

Ohashi, N. et al. (1991). "Observations of 11 Protostellar Sources in Taurus With Nobeyama Millimeter Array: Growth of Circumstellar Disks". In: *Astronomical Journal* 102, p. 2054. DOI: 10.1086/116029.

Oort, J.H. and van de Hulst, H.C. (1946). "Gas and smoke in interstellar space". In: *Bulletin of the Astronomical Institutes of the Netherlands* 10, p. 187.

Panopoulou, G.V. et al. (2022). "The width of Herschel filaments varies with distance". In: *Astronomy and Astrophysics* 657, p. L13. DOI: 10.1051/0004-6361/202142281.

Payne-Gaposchkin, C.H. (1925). "Stellar atmospheres: A contribution to the observational study of high temperature in the reversing layers of stars". PhD thesis. Radcliffe College, United States.

Penteado, E.M. et al. (2015). "Spectroscopic constraints on CH_3OH formation: CO mixed with CH_3OH ices towards young stellar objects". In: *Monthly Notices of the Royal Astronomical Society* 454, pp. 531–540. DOI: 10.1093/mnras/stv1987.

Penzias, A.A. et al. (1971). "Interstellar Carbon Monosulfide". In: *The Astrophysical Journal Letters* 168, p. L53. DOI: 10.1086/180784.

Perotti, G. et al. (2023). "Water in the terrestrial planet-forming zone of the PDS 70 disk". In: *Nature* 620, pp. 516–520. DOI: 10.1038/s41586-023-06317-9.

Pickering, W.H. (1912). "The Motion of the Solar System relatively to the Interstellar Absorbing Medium". In: *Monthly Notices of the Royal Astronomical Society* 72, p. 740. DOI: 10.1093/mnras/72.9.740.

Pineda, J.E. et al. (2011). "Expanded Very Large Array Observations of the Barnard 5 Star-forming Core: Embedded Filaments Revealed". In: *The Astrophysical Journal Letters* 739, p. L2. DOI: 10.1088/2041-8205/739/1/L2.

– (2015). "The formation of a quadruple star system with wide separation". In: *Nature* 518, pp. 213–215. DOI: 10.1038/nature14166.

Pontoppidan, K.M. et al. (2014). "Volatiles in Protoplanetary Disks". In: *Protostars and Planets VI*. Ed. by H. Beuther et al. University of Arizona Press, pp. 363–386. DOI: 10.2458/azu_uapress_9780816531240.

Potapov, A. et al. (2025). "Is cosmic dust porous?" In: *The Astronomy and Astrophysics Review* 33, p. 6. DOI: 10.1007/s00159-025-00164-5.

Priestley, F.D. et al. (2025). "NEATH IV: an early onset of complex organic chemistry in molecular clouds". In: *Monthly Noticed of the Royal Astronomical Society* 537, pp. 2453–2461. DOI: 10.1093/mnras/staf191.

Rabli, D. and Flower, D. R. (2010). "The rotational excitation of methanol by molecular hydrogen". In: *Monthly Notices of the Royal Astronomical Society* 406, pp. 95–101. DOI: 10.1111/j.1365-2966.2010.16671.x.

Rickard, L.J. et al. (1975). "Detection of extragalactic carbon monoxide at millimeter wavelengths." In: *The Astrophysical Journal Letters* 199, pp. L75–L78. DOI: 10.1086/181852.

– (1977). "Observations of extragalactic molecules. II. HCN and CS." In: *The Astrophysical Journal* 214, pp. 390–393. DOI: 10.1086/155261.

Rivilla, V.M. et al. (2020). "Prebiotic Precursors of the Primordial RNA World in Space: Detection of NH_2OH". In: *The Astrophysical Journal Letters* 899. DOI: 10.3847/2041-8213/abac55.

Rivilla, Víctor M. et al. (2021). "Discovery in space of ethanolamine, the simplest phospholipid head group". In: *Proceedings of the National Academy of Science* 118. DOI: 10.1073/pnas.2101314118.

Rocha, W.R.M. et al. (2024). "JWST Observations of Young protoStars (JOYS+): Detecting icy complex organic molecules and ions. I. CH_4, SO_2, $HCOO^-$, OCN^-, H_2CO, HCOOH, CH_3CH_2OH, CH_3CHO, CH_3OCHO, and CH_3COOH". In: *Astronomy and Astrophysics* 683, A124. DOI: 10.1051/0004-6361/202348427.

Rubin, R.H. et al. (1971). "Microwave Detection of Interstellar Formamide". In: *The Astrophysical Journal Letters* 169, p. L39. DOI: 10.1086/180810.

Rybicki, G.B. and Hummer, D.G. (1991). "An accelerated lambda iteration method for multilevel radiative transfer." In: *Astronomy and Astrophysics* 245, pp. 171–181.

Sadavoy, S.I. (2013). "Star Formation in the Perseus Molecular Cloud: A Detailed Look at Star-Forming Clumps with Herschel". PhD thesis. University of Victoria, Canada.

Saha, M.N. (1937). "Molecules in Interstellar Space?" In: *Nature* 139, p. 840. DOI: 10.1038/139840a0.

Sakai, N. and Yamamoto, S. (2013). "Warm Carbon-Chain Chemistry". In: *Chemical Reviews* 113, pp. 8981–9015. DOI: 10.1021/cr4001308.

Sanz-Novo, M. et al. (2025). "On the Abiotic Origin of Dimethyl Sulfide: Discovery of Dimethyl Sulfide in the Interstellar Medium". In: *The Astrophysical Journal Letters* 980, p. L37. DOI: 10.3847/2041-8213/adafa7.

Schmiedeke, A. et al. (2021). "Dissecting the Supercritical Filaments Embedded in the 0.5 pc Subsonic Region of Barnard 5". In: *The Astrophysical Journal* 909, p. 60. DOI: 10.3847/1538-4357/abd6ef.

Schöier, F.L. et al. (2005). "An atomic and molecular database for analysis of submillimetre line observations". In: *Astronomy and Astrophysics* 432. DOI: 10.1051/0004-6361:20041729.

Scibelli, S. et al. (2024). "Survey of complex organic molecules in starless and pre-stellar cores in the Perseus molecular cloud". In: *Monthly Notices of the Royal Astronmical Society* 533, pp. 4104–4149. DOI: 10.1093/mnras/stae2017.

Scibelli, S. and Shirley, Y. (2020). "Prevalence of Complex Organic Molecules in Starless and Prestellar Cores within the Taurus Molecular Cloud". In: *The Astrophysical Journal* 891, p. 73. DOI: 10.3847/1538-4357/ab7375.

Scolati, H.N. et al. (2023). "Explaining the Chemical Inventory of Orion KL through Machine Learning". In: *The Astrophysical Journal* 959, p. 108. DOI: 10.3847/1538-4357/ad004c.

Siebenmorgen, R. et al. (2014). "Dust in the diffuse interstellar medium. Extinction, emission, linear and circular polarisation". In: *Astronomy and Astrophysics* 561, A82. DOI: 10.1051/0004-6361/201321716.

Snyder, L.E. et al. (1969). “Microwave Detection of Interstellar Formaldehyde”. In: *Physical Review Letters* 22, pp. 679–681. DOI: 10.1103/PhysRevLett.22.679.
– (1974). “Radio Detection of Interstellar Dimethyl Ether”. In: *The Astrophysical Journal Letters* 191, p. L79. DOI: 10.1086/181554.
– (1983). “An extensive galactic search for conformer II Glycine.” In: *The Astrophysical Journal* 268, pp. 123–128. DOI: 10.1086/160937.
Snyder, L.E. and Buhl, D. (1973). “Interstellar Methylacetylene and Isocyanic Acid”. In: *Nature Physical Science* 243, pp. 45–46. DOI: 10.1038/physci243045a0.
Solomon, P.M. et al. (1971). “Detection of Millimeter Emission Lines from Interstellar Methyl Cyanide”. In: *The Astrophysical Journal Letters* 168, p. L107. DOI: 10.1086/180794.
Spitzer, L. and Tukey, J.W. (1951). “A Theory of Interstellar Polarization.” In: *The Astrophysical Journal* 114, p. 187. DOI: 10.1086/145463.
Strömgren, B. (1948). “On the Density Distribution and Chemical Composition of the Interstellar Gas.” In: *The Astrophysical Journal* 108, p. 242. DOI: 10.1086/145068.
Struve, O. (1925). “On the calcium clouds”. In: *Popular Astronomy* 33, p. 639.
– (1926). “On the calcium clouds”. In: *Popular Astronomy* 34, p. 1.
– (1927). “Interstellar calcium”. In: *The Astrophysical Journal* 65, pp. 163–199. DOI: 10.1086/143041.
– (1928). “Further work on interstellar calcium”. In: *The Astrophysical Journal* 67, pp. 353–390. DOI: 10.1086/143121.
– (1933). “Matter in interstellar space”. In: *Popular Astronomy* 41, p. 423.
Swings, P. (1937). “A note on molecular absorption in interstellar space”. In: *Monthly Notices of the Royal Astronomical Society* 97, p. 212. DOI: 10.1093/mnras/97.3.212.
Swings, P. and Rosenfeld, L. (1937). “Considerations Regarding Interstellar Molecules”. In: *The Astrophysical Journal* 86, pp. 483–486. DOI: 10.1086/143880.
Takayanagi, K. and Nishimura, S. (1960). “Cooling of the Interstellar Clouds in Region of Neutral Hydrogen”. In: *Publications of the Astronomical Society of Japan* 12, p. 77.

Taquet, V. et al. (2017). "Chemical complexity induced by efficient ice evaporation in the Barnard 5 molecular cloud". In: *Astronomy and Astrophysics* 607, A20. DOI: 10.1051/0004-6361/201630023.

Tennyson, J. and Faure, A. (2019). "Electron Collision Processes". In: *Gas-Phase Chemistry in Space*. IOP Publishing, 5-1 to 5–26. DOI: 10.1088/2514-3433/aae1b5ch5.

Thorndike, S.L. (1930). "Interstellar Matter". In: *Publications of the Astronomical Society of the Pacific* 42, p. 99. DOI: 10.1086/124007.

Tielens, A.G.G.M. (2005). *The Physics and Chemistry of the Interstellar Medium*. Cambridge University Press.

Trumpler, R.J. (1930). "Preliminary results on the distances, dimensions and space distribution of open star clusters". In: *Lick Observatory Bulletin* 420, pp. 154–188. DOI: 10.5479/ADS/bib/1930LicOB.14.154T.

van de Hulst, H.C. (1946). "The solid particles in interstellar space". In: *Recherches Astronomiques de l'Observatoire d'Utrecht* 11, pp. 2.i–2.

van der Tak, F.F.S. et al. (2007). "A computer program for fast non-LTE analysis of interstellar line spectra. With diagnostic plots to interpret observed line intensity ratios". In: *Astronomy and Astrophysics* 468, pp. 627–635. DOI: 10.1051/0004-6361:20066820.

van Dishoeck, E.F. et al. (2013). "Interstellar Water Chemistry: From Laboratory to Observations". In: *Chemical Reviews* 113, pp. 9043–9085. DOI: 10.1021/cr4003177.

– (2014). "Water: From Clouds to Planets". In: *Protostars and Planets VI*. Ed. by H. Beuther et al. University of Arizona Press, pp. 835–858. DOI: 10.2458/azu_uapress_9780816531240.

Vasyunin, A.I. et al. (2017). "Formation of Complex Molecules in Prestellar Cores: A Multilayer Approach". In: *The Astrophysical Journal* 842, p. 33. DOI: 10.3847/1538-4357/aa72ec.

Watanabe, N. and Kouchi, A. (2002). "Efficient Formation of Formaldehyde and Methanol by the Addition of Hydrogen Atoms to CO in H_2O-CO Ice at 10 K". In: *The Astrophysical Journal Letters* 571, pp. L173–L176. DOI: 10.1086/341412.

Watson, W.D. (1976). "Interstellar molecule reactions". In: *Reviews of Modern Physics* 48, pp. 513–552. DOI: 10.1103/RevModPhys.48.513.

Weinreb, S. et al. (1963). "Radio Observations of OH in the Interstellar Medium". In: *Nature* 200, pp. 829–831. DOI: 10.1038/200829a0.

Wilson, R.W. et al. (1970). "Carbon Monoxide in the Orion Nebula". In: *The Astrophysical Journal Letters* 161, p. L43. DOI: 10.1086/180567.

Wilson, T.L. (2013). *Tools of Radioastronomy*. Springer.

Wirström, E.S. et al. (2014). "Cold Water Vapor in the Barnard 5 Molecular Cloud". In: *The Astrophysical Journal Letters* 788, p. L32. DOI: 10.1088/2041-8205/788/2/L32.

Yamamoto, S. (2017). *Introduction to Astrochemistry: Chemical Evolution from Interstellar Clouds to Star and Planet Formation*. Springer.

Zeng, S. et al. (2021). "Probing the Chemical Complexity of Amines in the ISM: Detection of Vinylamine ($C_2H_3NH_2$) and Tentative Detection of Ethylamine ($C_2H_5NH_2$)". In: *The Astrophysical Journal Letters* 920. DOI: 10.3847/2041-8213/ac2c7e.

Zinner, E. (2014). "Presolar Grains". In: *Treatise on Geochemistry (Second Edition)*. Ed. by H.D. Holland and K.K. Turekian. Vol. 1: Meteorites and Cosmochemical Processes. Elsevier Ltd., pp. 181–213.

Zucker, C. et al. (2018). "Mapping Distances across the Perseus Molecular Cloud Using CO Observations, Stellar Photometry, and Gaia DR2 Parallax Measurements". In: *The Astrophysical Journal* 869, p. 83. DOI: 10.3847/1538-4357/aae97c.

Zuckerman, B. et al. (1975). "Detection of interstellar trans-ethyl alcohol." In: *The Astrophysical Journal Letters* 196, pp. L99–L102. DOI: 10.1086/181753.